POLITECNICO DI MILANO
School of Industrial and Information Engineering
Master of Science in Mechanical Engineering

Wind Tunnel Test on Full Array Solar PV Trackers

Supervisor:
Prof. Marco BELLOLI

Co-supervisor:
Ing. Alessandro FONTANELLA

Author:
Alican YAĞCI
Matr. 872155

Academic Year 2018 – 2019

To Bensu, Huriye, Uğur and Caner,

Acknowledgments

Firstly, I would like to express my sincere gratitude to Prof. Marco Belloli for giving me an opportunity to work in one of the most comprehensive wind tunnels in the world. Taking a part in this study gave me a chance to work with very professional individuals and observe wind tunnel applications closely. It was a great experience for me without any doubt.

Additionally, I would like to thank Ing. Alessandro Fontanella for all the support and guidance he has provided for my master thesis. His guidance helped me in all the aspects of research and implementation of this study in Politecnico di Milano, I could not have imagined having a better co-advisor for my master study.

Finally, I would like to give special appreciations to my family and friends without their encouragement and motivation this success would not have been possible. I would also like to specially thank Gökhan Yağcı for being by my side during the all of my days in Milano. I am so lucky to have them.

Table of Contents

List of Figures

List of Tables

Abstract

The aim of this study is creating threshold aerodynamic loading data for single axis PV tracker systems (PVT). Even if the increasing usage of this type of solar systems in recent years due to increasing efficiency and reducing cost, there are still not many studies about the aerodynamic interaction of the tracker support mechanisms. However, investors need benchmark wind loading data to secure their investment from any kind of wind damage.

To test the aerodynamic behavior of 5 x 3 PVT array, 1/15 scale models were built and placed inside a wind tunnel turn table. Turbulence and boundary layer conditions simulated according to Eurocode I terrain profile and pressure coefficients were measured for different pitch and exposure angles for two different ground cover ratio (GCR) arrangements. Recorded pressure coefficients were used to calculate normal force and torque coefficients for three different loading zones.

All test results were presented in peak loading graphs and tables. Graphs were organized for different rows and loading zones to investigate the effect of panel location to loading coefficients. Also, peak coefficient graphs were used to point out most critical location in the array. After presenting each set of results, necessary comments made considering the theoretical background of the problem. In addition to that, effect of the test variables such as pitch angle, exposure angle and ground cover ratio were investigated separately.

Keywords: *Atmospheric Boundary Layer, Wind Tunnel, PV Tracker, Wind Loading, Load Coefficient, Aerodynamics*

Sommario

Il presente studio è volto a definire i dati di carico aerodinamico per la progettazione di un generico sistema di inseguimento fotovoltaico ad asse singolo (PVT). Anche se negli ultimi anni questo tipo di sistema solare è stato interessato da un crescente utilizzo, specialmente a causa della maggiore efficienza e dei costi ridotti, pochi sono gli studi relativi ai carichi generati dal vento sulla struttura del PVT e gli investitori richiedono dati di riferimento per garantire l'impianto rispetto qualsiasi tipo di danno generato dal vento.

Al fine di definire il comportamento aerodinamico di un generico schieramento 5x3 di PVT, sono stati costruiti dei modelli in scala 1/15 degli inseguitori fotovoltaici, poi piazzati all'interno della sezione a strato limite atmosferico della galleria del vento del Politecnico di Milano. Sono state simulate le approriate condizioni di vento definite secondo l'Eurocodice e sono stati misurati i coefficienti di pressone per diversi angoli di pitch, di esposizione al vento e due diversi rapporti di copertura del terreno (GCR). Lo schieramento di pannelli è stato diviso in zone in cui gli inseguitori sono soggetti a carichi aerodinamici simili e per ciascuna zona sono stati definiti i coefficienti di carico per la progettazione.

I risultati delle prove sono presentati come grafici e tabelle dei carichi di picco. I grafici sono organizzati per le diverse righe e zone di carico dello schieramento per studiare l'effetto della posizione del pannello sui coefficienti di carico. I coefficienti di carico massimi sono stati utilizzati per individuare le posizioni più critiche all'interno dello schieramento. Ogni set di risultati è stato commentato in base alle nozioni teoriche sul problema aerodinamico.

Parole chiavi: *Strato limite atmosferico, Galleria del vento, Inseguitore fotovoltaico, Carichi aerodinamici, Coefficienti aerodinamici, Aerodinamica*

Chapter 1. Introduction

1.1 Overview

World electricity consumption is getting higher each year with increasing human population. According to Global Energy Statistical Yearbook [1], world energy consumption in 1990, was around 10.000 Thw, but it reaches up to 22.000 Thw in 2017, which means more than twice increase in consumption in 27 years. As a consequence, the challenge of supplying enough electricity to meet the demand pushes engineers to discover new and more efficient ways for producing electricty. In addition to that, with the increasing number of researches about the environmental effects of fossil fuels, now, we have a better understanding about how fossil fuels can be harmful for the future of our planet. Therefore, increase in the usage of renewable energy systems in recent years is not a surprise. This increase is related to two aspects of the renewable energy sources which are being clean and free. By using renewable power production systems, we can directly (solar systems) or indirectly (wind turbines etc.) extract the power coming from the sun which is an available source of energy for almost every country in the world, which makes it free source of energy. Also, this power source is considered as clean because there is no exhaust of greenhouse gases, which are the main reason of global warming.

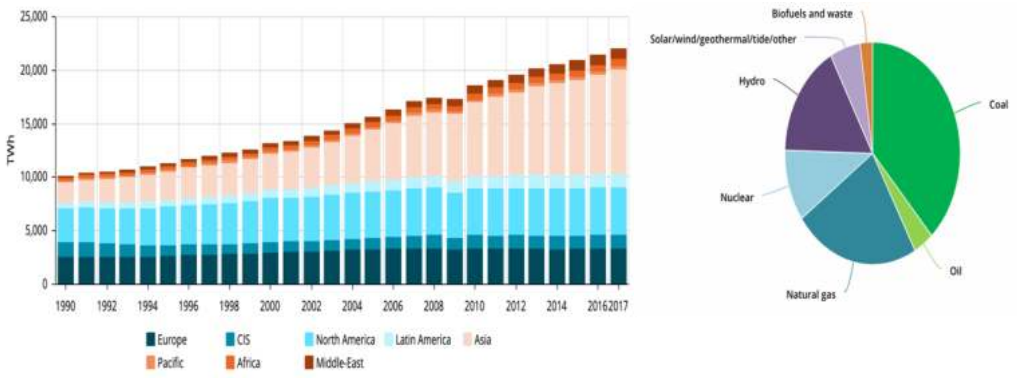

Figure 1.1 World electricity consumption between 1990 and 2017 [1] and gross energy production percentage by source in 2016 [2]

From statistical report of International Energy agency [2], in 2016, generation from combustible fuels accounted for 67.3% of total world gross electricity production. Electricity generation from fossil fuels fell for the fifth consecutive year in 2017, with generation from total combustible fuels accounted for 59.4% of total OECD gross electricity production (compared to 72.8% for non-OECD).

Electricity generation from renewable sources such as wind (+15.1%) and solar (+21.9%) registered robust growth. The most dramatic increase is in solar industry because there is a continues and fast increase in solar cell efficiencies and decrease in panel costs.

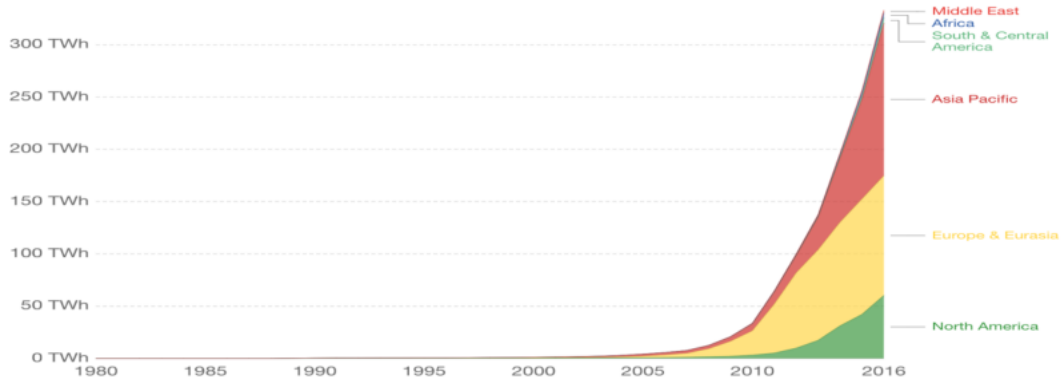

Figure 1.2 Solar PV energy consumption in years [2]

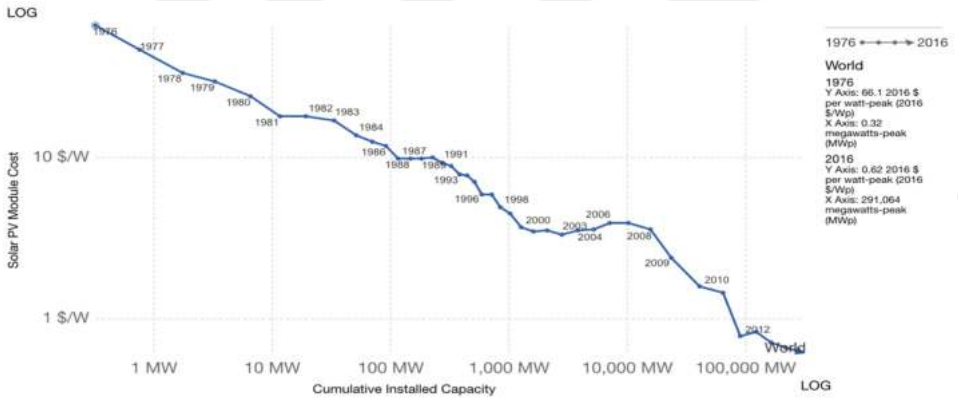

Figure 1.3 Solar PV module prices vs cumulative capacity between 1976 and 2016 [3]

Among all the power extraction methods from solar energy one of the widely commercialized solar energy technologies is the photovoltaic (PV) solar cells that convert the sunlight directly into electricity. The solar cells are made of semiconductor materials such as Silicon or Cadmium Telluride (CdTe). Sunlight contains energy particles called photons when light from the sun incidents on a solar cell, the photons are absorbed by the semiconductor material. The absorbed photons knock electrons (e-) out of their atoms in the semiconductor creating a hole (h+). The design of the semiconductor diode ensures that the released electrons move in a single direction and produces electricity. Sets of solar cells are combined to make a solar panel. They are installed by fastening them to a framework or support structure as standalone units or as an array of PV units. A

standalone solar PV structure may also comprise of several individual panels arrayed as a single structure. Furthermore, PV panels can be mounted on a tracker system to orient the panels toward the sun to increase energy production. Trackers are available as both single- and dual-axis, there are some key differences between the two: namely, while single-axis trackers tilt along the y-axis (enabling them to capture a bit more sun than the traditional fixed systems), dual-axis trackers move along both in the x- and y-axes. Thus, while fixed systems only collect maximum power for a few hours in the middle of the day, trackers can maintain this capacity throughout the entire day.

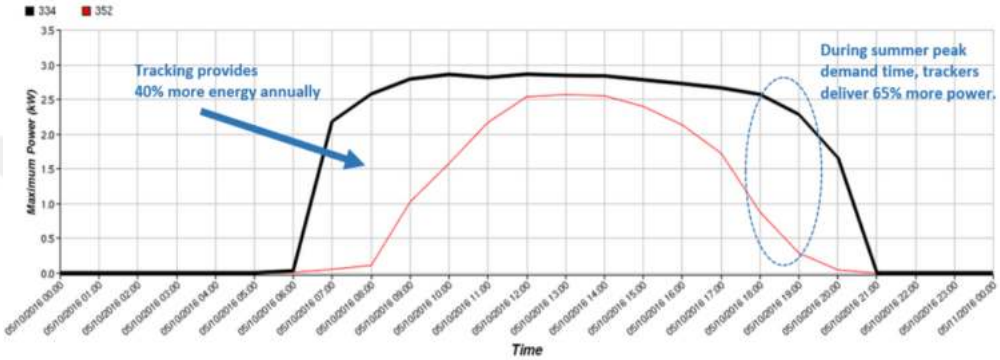

Figure 1.4 Comparison of fixed solar vs solar tracker

Figure 1.4 above [4] shows two 3kW PV arrays located on the same property in Vermont. The black line represents a dual-axis solar tracker; the red line represents a fixed roof-mount system, south-facing at 30° tilt. While the fixed system never reaches maximum power, the tracker maintains full power output throughout most of the day, from dawn to dusk. However dynamic behavior of PVT systems requires more complex design for the support structure of the panels. It is very important to know aerodynamic loadings on the system to minimize the risk of failure by designing reliable support mechanism. Therefore, this study investigates aerodynamic loading on a single axis 5 x 3 PVT array to provide threshold load coefficient data to the client.

Figure 1.5 Example of PV tracker array and photo of a wind damaged system

1.2 Motivation

Despite the increasing popularity of PV tracker systems, there are not enough studies about the aerodynamic loadings on trackers. Wind engineers made many efforts to define wind loadings on structures to create building codes and standards in order to ease the design process. However, these standards alone do not provide the necessary guidance for solar field construction because even the small assumptions made according to codes may lead great errors during actual operation of a solar field. Panel manufacturers can optimize their design of support mechanism and investors secure their solar farm from any damage related with the gusts of wind by accurately knowing the wind loadings on the array. Thus, wind engineering studies can provide safe, yet economical designs for PVT systems. With the reducing cost and increasing reliability more people can choose to produce energy by using solar PVT systems.

1.3 Objectives

The main objective of this study is, providing peak normal force and torque coefficients for various locations in the full PVT array according to changing exposure angles, pitch angles and row spacings. In order to see the effect of row spacing, models were tested with two different ground cover ratios. Tests were carried out in wind tunnel of Politecnico di Milano, detailed information about the test facility and setup is provided in latter chapters. According to pressure data obtained from pressure taps on panel models, force coefficients are calculated to find the most critical sections in the array for different arrangements. At the end, this study aims to provide threshold wind loading data that needs to be considered during the design stage of the PVT array.

1.4 Thesis Layout

The thesis contains five chapters:

- Chapter 1 provides introduction and description of the problem. Importance of solar systems and some of the trends related with them presented. PVT is described and the reasons why this kind of study is necessary are explained. Motivation and the objective of this study also presented in chapter 1.

- Chapter 2 provides related fluid mechanics theory to create better understanding for the discussions presented in proceeding chapters. Required theoretical background for the aerodynamic investigation of PVT's are described. In addition to that, general concepts and methods related with wind tunnel testing is presented at the end of this chapter.

- Chapter 3 introduces the test setup and the wind tunnel used in this study. General specification of Politecnico di Milano wind tunnel facility (GVPM) is presented. Afterwards, necessary test conditions inside the

tunnel are explained and simulated ABL and turbulence conditions are presented. Also test models and the instrumentation are explained in detail.

- Chapter 4 introduces all set of test results starting with isolated first row test and continues for the results of full array tests. Result presented in peak coefficient graphs and the highest peak coefficient tables. All presented graphs and tables categorized according to two different GCR arrangements on the wind tunnel test section. Comments about the trends shown in the graphs and discussions for the effect of the test variables are also presented in this chapter.

- Chapter 5 concludes the thesis by summarizing the test procedure and listing all major outcomes of this experiment. Some of the limitations of this study explained and finally, suggestions are made for possible future studies. At the end of chapter 5, references used in this thesis are listed. After references section some of the important drawings, photos and tables are presented in Appendix section.

Chapter 2. Theory

2.1 Atmospheric Boundary Layer

Atmospheric boundary layer (ABL) is the region of the lower troposphere where Earth's surface strongly influences temperature, moisture and wind through the turbulent transfer of air mass. We can also define ABL as a part of the atmosphere we are live in which experiences momentum and heat exchange with boundary layer's surface in short time scales (less than 1 hour) due to turbulent flow. As a result, ABL affects both the dynamics and thermodynamics of the atmosphere and generally extends up to 500-1000 m, air above this height inside the troposphere which extends up to 7-20 km considered as free atmosphere. According to Palmen and Newton [5], more than half of the atmosphere's kinetic energy loss happens inside the ABL. Friction forces caused by the terrain roughness makes the wind's flow turbulent that randomly varies in space and time.

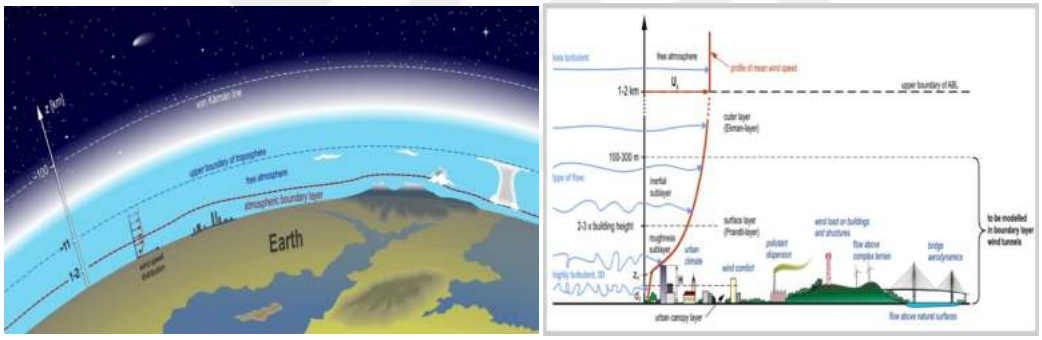

Figure 2.1 Schema representation of ABL

Close to earth's surface, the atmospheric flow becomes turbulent and breaks up in eddies that effectively transfer momentum and heat fluxes in vertical direction inside BL. Before describing turbulence, random swirls of motion called eddies need to be known because usually turbulence is superimposition of different size of eddies [7]. There are two main reasons for the flow to become turbulent close to ground; the first reason is vertical wind shear, which makes wind speed zero at ground and introduces hydrodynamic instability to flow. The second reason is negative buoyancy which is caused by the heating of earth's surface by solar radiation. Heat exchange between surface and the flow creates statically unstable

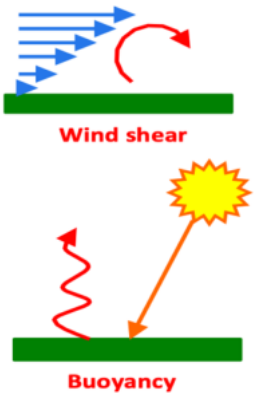

Figure 2.2

air due to change in air density causes mixing of flow. These two phenomena are represented in figure 2.2. The modified geostrophic balance due to surface shear changes the angle between mean wind vector and rotates isobars towards the low-pressure side. These changes in wind speed and direction are explained by Ekman Spiral [6] (fig 2.3). For strong winds, effects due to shear stress more significant than thermal effects, however for winds slower than 10 m/s, thermal effects cannot be neglected. Inside the following sub sections, concept that are related to ABL are explained briefly.

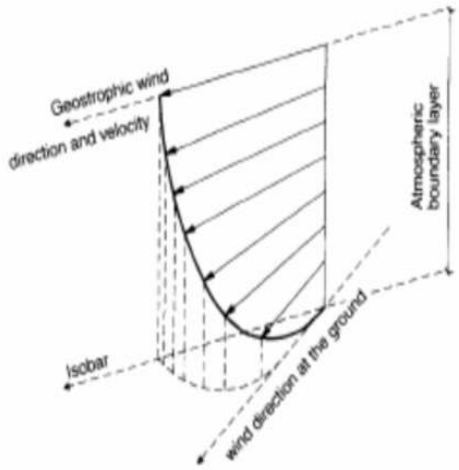

Figure 2.3 Ekman Spiral [6]

2.1.1 Mean Wind Velocity Profile

Mean wind velocity can be defined as average wind speed recorded over at least period of 10 minutes at a certain location. Inside the ABL, wind velocity profile mainly depends on the type of terrain because of the strong effects of surface roughness. Friction due to surface roughness induces a frictional drag force on the wind which causes the wind speed to become zero at the ground. On the other hand, pressure gradient inside the ABL, increases velocity of the wind with the increasing height from ground level. Effects of terrain type on the wind velocity profile can be seen in fig 2.4.

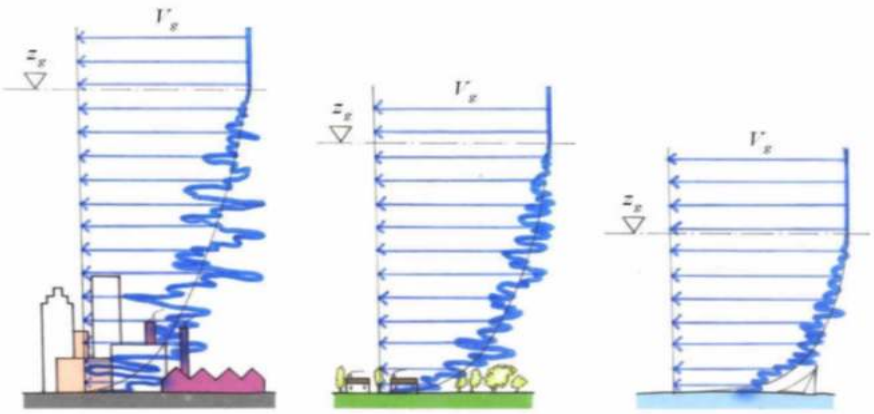

Figure 2.4 Wind velocity profile for urban, rural and off-shore areas

Wind velocity at a particular point in space and time can be defined by three orthogonal velocity components. Each component represents instantaneous wind

velocity in different directions, *u* is for mean wind direction, *v* horizontal direction normal to *u* and lastly, *w* vertical velocity component.

$$u = u_m + u'$$

$$v = v_m + v' = v'$$

$$w = w_m + w' = w'$$

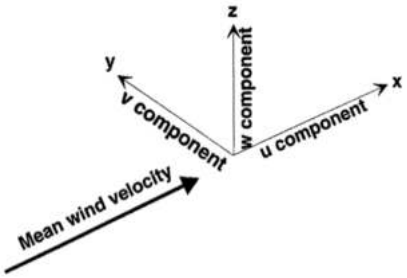

Figure 2.5 Representation in cartesian coordinate

The subscript 'm' shows the mean value and the sign over the velocity components shows the fluctuating component. Mean velocity is equal to zero for horizontal and vertical components. In addition to that fluctuating components of the wind can be considered stationary with a zero-mean value. With knowing these, now, we can define the mean wind velocity according to height from ground (z). To do so, we can use logarithmic law which gives the mean wind velocity for systems that are located close to ground where surface roughness effects dominate.

$$u_m(z) = \frac{u^*}{\kappa} ln \frac{z}{z_0} \qquad u^* = \sqrt{\frac{\tau_0}{\rho}}$$

u^* is friction velocity, Von Karman constant (typically 0.4), z_0 aerodynamic roughness length, ρ is air density and τ_0 is shear stress at ground level. It should not be forgotten that logarithmic law only valid for systems with height lower than atmospheric surface layer which is equal to 100 m for most of the strong wind applications. Over this limit, height of the boundary layer becomes more important than the effect of surface roughness. However, when we consider ground mounted PV trackers, we can say that applying logarithmic law is appropriate due to the small height and strong effects of surface roughness. To define surface roughness, aerodynamic roughness length (z_0) is being used. Aerodynamic roughness length is related with the geometry and spacing of the terrain that the system is located on [7]. Different roughness lengths for different

terrain types are tabulated in different codes and standards. Eurocode terrain profiles and z_0 values can be found in table 2.1.

	Terrain category	z_0 m	z_{min} m
0	Sea or coastal area exposed to the open sea	0,003	1
I	Lakes or flat and horizontal area with negligible vegetation and without obstacles	0,01	1
II	Area with low vegetation such as grass and isolated obstacles (trees, buildings) with separations of at least 20 obstacle heights	0,05	2
III	Area with regular cover of vegetation or buildings or with isolated obstacles with separations of maximum 20 obstacle heights (such as villages, suburban terrain, permanent forest)	0,3	5
IV	Area in which at least 15 % of the surface is covered with buildings and their average height exceeds 15 m	1,0	10

Table 2.1 Terrain categories and parameters

2.1.2 Turbulence

In many reference books and articles, turbulence is associated with chaotic changes in pressure and velocity. Unlike the case of laminar flow, stream lines are not collateral to each other and flow consists of random vortexes. Due to the randomness of the flow, it is really complex to describe turbulence with deterministic approach rather than stochastic approach. In low frequency levels which are related with the instabilities of mean flow, turbulence starts to be generated as large eddy bubbles. With increasing frequency, large eddies break up into smaller and smaller eddies by transferring their energy and forming an energy cascade. At some point where eddies become too small, viscosity becomes very significant property for the flow due to friction which causes energy dissipation as heat. These high frequency levels are associated to the turbulence inside the ABL. Special interest should be shown to turbulence for studies investigating the structural responses, because peak wind values are related to fluctuations inside the turbulent region. These fluctuations can be described as the superimposition of eddies with different sizes and frequencies. Estimation of the largest eddies is made with using integral length scales which are the cross correlation of wind velocity at two points in flow direction.

One of the most important parameters to characterize turbulence is turbulence intensity which is the ratio of the standard deviation of the wind component to mean wind velocity at the reference height z.

$$I_u(z) = \frac{\sigma_u(z)}{u_m(z)} \quad ; \quad I_v(z) = \frac{\sigma_v(z)}{u_v(z)} \quad ; \quad I_u(z) = \frac{\sigma_v(z)}{u_v(z)}$$

If we consider most of the cases in wind engineering applications, flow is typically in horizontal direction which creates much stronger turbulence in x-direction. Therefore, in most of the applications, only $I_u(z)$ is used to characterize the turbulence intensity over the system.

2.2 Flow Over Immersed Bodies

According to B. R. Munson [8], when a body moves through a fluid, an interaction between the body and the fluid arises, this interaction can be described by the forces at the fluid body interface. The forces acting on the body are related to wall shear stress due to viscosity and normal stress due to pressure. Because of the complexity of measuring shear stress and pressure distribution around the body, engineers often use resultant forces that are generated from the gradients over the body. If the fluid in motion is air, then this force is called aerodynamic force. There two components of aerodynamic force, the one, that is in the same direction with the flow is called drag force and the other one, that is perpendicular to the flow is called lift force. Good fluid dynamic background is needed to understand the loading around an immersed body because it depends on the air flow pattern around object in various shapes and sizes. There are 4 methods available for investigating aerodynamic forcing around a body;

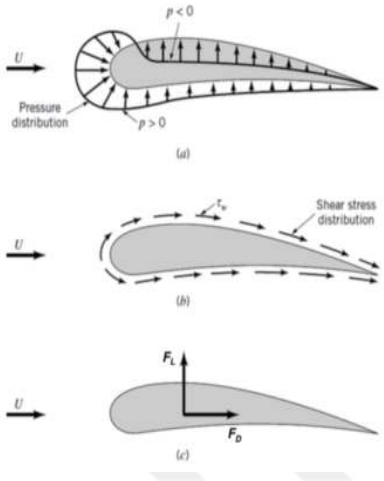

Figure 2.6 Forces on a 2-D immersed object a) pressure force b) shear stress c) resultant forces

1. *Full Scale Measurements:* Before the availability of powerful computational tools we are using today, full scale field test was one of the popular options to collect wind data. However, it is difficult to perform since the lack of control on the large-scale environment which leads to uncertainties in the collected data. In addition to that, they are not suitable method for using during the design process.
2. *Analytical Formulations:* There some available analytical formulations in literature based on simplifications such as potential flow, which is frictionless, irrotational flow. However, viscosity cannot be neglected in every situation and this leads huge errors between the ideal and real cases. So, analytical formulations are typically useful for very specific simplified cases.

3. *Computational Fluid Dynamics (CFD):* To describe the fluid motion inside the BL, Navier-Stokes equations that are set of nonlinear equations, can be treated via CFD approach. This method is becoming very popular with the increasing available level of computational power in research labs. Although it is a very practical approach for simple flow systems, CFD method still requires too much effort for complex flows due to increase in cost with increasing computational effort.
4. *Wind Tunnel Tests:* Major part of the aerodynamic knowledge used in wind engineering is coming from wind tunnel tests on small scale models. There are many standards developed to make the environment inside the tunnel closest with a real case. According to these tests, building code and standards created to ease the design of many civil engineering projects. Further detailed information about wind tunnel tests is at the end of this chapter.

2.2.1 Aerodynamic Forcing and Force Coefficients

As introduced earlier, when there is a relative velocity between air and a body, aerodynamic forces arise due to the perturbation induced by the body to the flow. To define these forces, pressure and shear distribution should be integrated over the whole body. The aerodynamic force on a body has two components, the one parallel to the wind flow direction is called drag force. Drag force also has two parts which are friction drag and pressure drag. Friction drag is directly generated from the shear stress on the body. Thus, magnitude of friction drag is proportional with the shear stress on the body and the orientation of the body with the flow. If the surface is parallel to the flow then, all shear stress contributes the drag force [9], otherwise contribution to the drag force is according to sinus of the relative angle between the surface and the flow. However, due to working with low viscosity fluids or flows with high Re numbers, the contribution of friction drag to actual drag force is quite low in structural wind engineering applications. On the other hand, neglecting friction drag for highly streamlined bodies or low Re number flows, leads errors in calculations because the main portion of the actual drag force comes from the shear part. The second part of the drag force is the pressure drag, which is the direct result of pressure distribution around the immersed body. Pressure drag is highly dependent on the shape of the body, that is why, it is also called ‘form drag’ in literature. Like the case of friction drag, pressure drag is also proportional with the magnitude of the pressure difference along the flow and the orientation of the body with the flow, but this time, contribution is a cosine function of the angle between the incoming wind and the surface.

Figure 2.7 In the first figure due to parallel position of the body, friction contribution is 100% while pressure contribution is 0%, vice versa for the last figure. For air foil, friction can be considered as 90% and for sphere it is 10%.

As mentioned before, the aerodynamic force component orthogonal to the flow is called lift force. If the immersed body is not symmetrical or does not produce a symmetrical flow, lift force normal to the stream arises. In order to provide better understanding of lift force generation, it is a common practice to apply Bernoulli equation to an airfoil; $\frac{p}{\rho} + \frac{V^2}{2} + gy = cost$ .The first term stands for static pressure, second term is kinetic energy and the last one represents the gravitational force per unit mass. These are the three components of total energy inside the flow. If we neglect the energy dissipation along the flow and consider the flow as inviscid, total energy entering from upstream should be equal to the total energy at the downstream. Therefore, if a fluid particle moves into high pressure field on the same elevation, according to Bernoulli equation, speed of the particle should decrease. In fig. 2.8, typical flow over an airfoil is shown. As can be seen from the deflection of black lines, flow over the airfoil is faster than the flow under the airfoil, and from Bernoulli equation we know that this means lower pressure on the upper side (suction side, SS), higher pressure on the bottom side (pressure side, PS) of the airfoil. This pressure difference between PS and SS is the main reason of lift force generation.

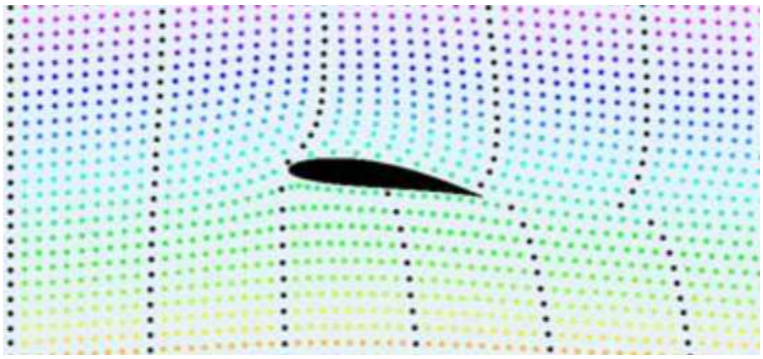

Figure 2.8 Flow over an airfoil

$$F_D = \int pcos(\theta) dA + \int \tau_w \sin(\theta)\, dA \quad [eqn.1]$$

$$F_L = \int -psin(\theta)dA + \int \tau_w \cos(\theta)\, dA \quad [eqn.2]$$

From above equations, it is possible to find values of lift and drag forces. It is easy to understand the dependence of these two equations with the shape of the body because of *dA* terms in each integral sign. In wind engineering applications, many of the projects have complex shapes and very detailed geometries, therefore many engineers are using non-dimensional numbers called force, momentum and pressure coefficients to determine aerodynamic characteristic of a body. Due to being direct representative of body shape, objects with the same geometrical shape should have same aerodynamic coefficients under different dimensional scales and flow conditions.

$$C_L = \frac{F_L}{\frac{1}{2}\rho U^2 A} \quad [eqn.3]\,; \qquad C_D = \frac{F_D}{\frac{1}{2}\rho U^2 A} \quad [eqn.4]$$

$$C_{M_i} = \frac{F_i}{\frac{1}{2}\rho U^2 AB} \quad [eqn.5]; \qquad C_P = \frac{p - p_0}{\frac{1}{2}\rho U^2} \quad [eqn.6]$$

Equations for lift, drag, momentum and pressure coefficients can be found above in the same order. *B* term inside the momentum coefficient equation is reference length and p_0 inside the pressure coefficient equation is reference pressure. It should be noted that, to be able to use aerodynamic coefficients, we must know the reference system and reference lengths because aerodynamic coefficients are highly depended on the shape of the structure. Other than geometrical dependence, there are 4 other parameters that have a relatively fewer but still significant influence on the aerodynamic coefficients. These factors are;

- Reynolds Number
- Mach Number
- Turbulence Intensity
- Surface Roughness Ratio

2.2.2 Boundary Layer Separation and Vortex Shedding

Let's assume inviscid flow over a body with non-zero thickness such as a cylinder. As a result of the assumption of inviscid flow (μ=0), Re number of the flow will be infinite ($Re = \frac{\rho UD}{\mu}$) , that will create symmetrical streamlines along the flow path as shown in fig 2.9 (a). Due to not negligible thickness of the body, fluid velocity along the cylinder varies between 0 - 2U. Velocity is zero at the so-called stagnation points which are located on the front and the back (points A-F). Moreover, flow reaches maximum velocity 2U at the top and bottom points of

the body (point C). This velocity distribution is shown in fig. 2.9 (b) where U and U_{fs} are upstream and free stream velocities. In fig 2.9 (c), pressure distribution with maximum $(p_0 + \rho U^2/2)$ and minimum $(p_0 - 3\rho U^2/2)$ points are presented. p_0 represents the upstream pressure. The most important observation can be made from fig 2.9 is the uniform pressure distribution around the cylinder. Pressures at the top equals to the pressure at the bottom and same condition also holds for the front and back sides. In the absence of viscous and pressure forces, drag force acting on the cylinder must be equal to zero.

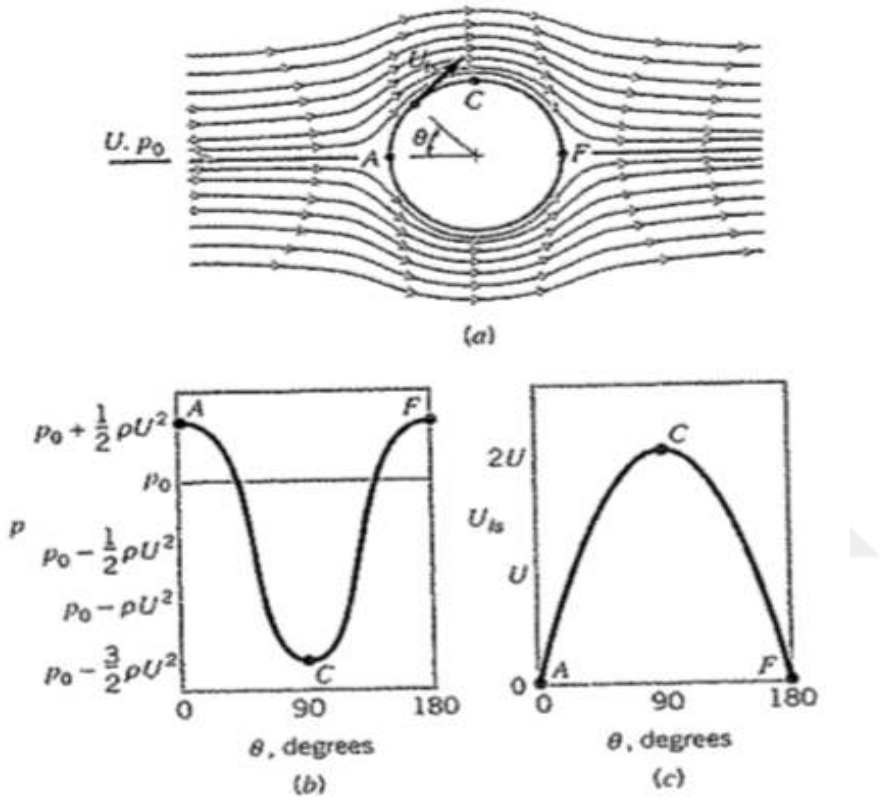

Figure 2.9 Inviscid flow around a cylinder [10]

On the other hand, inviscid flow assumption is just an ideal concept and does not exist in real applications. As we know from previous section, immersed body should experience a drag force. From above experiment, we can easily assume that this drag force is direct consequence of viscous forces inside the flow. However, if we make the same experiment with different fluids with decreasing viscosity, we will observe a drag force even inside the systems that are operating with fluids with negligibly small viscosity. This result leads us to concept that is called D'Alembert's Paradox which basically specifies that [10] the drag force on a body immersed in an inviscid flow equal to zero, but the drag force on a body inside a flow with a vanishingly small viscosity does not equal to zero.

When Prandtl introduced boundary layer concept in 1904, he enlightened D'Alambert's paradox by explaining pressure distribution inside boundary layer. Without viscous losses inside the flow, whole pressure energy can be recovered from kinetic energy, just like the case in fig 2.9. However, if we account the viscous effects inside BL, full energy recovery cannot be possible due to the friction force acting on the body. This case we need to consider a viscous flow over a cylinder which is shown in fig 2.10.

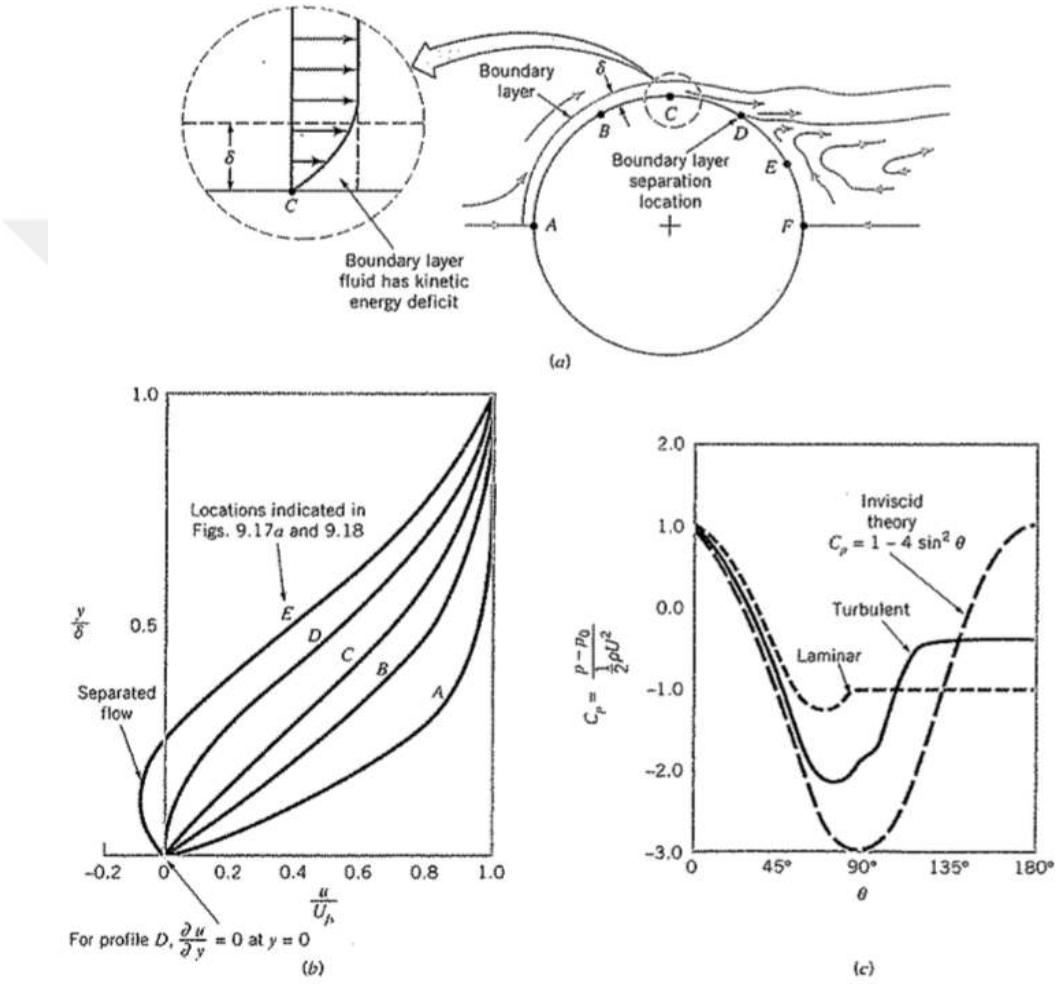

Figure 2.10 Boundary layer profile of a cylinder (a) BL separation (b) BL velocity profiles at different point on the cylinder (c) surface pressure distribution for inviscid and viscous flows[10]

Due to loss of energy along the fluid path inside the BL, fluid particles cannot recover all of the pressure energy. If the fluid is moving in an adverse pressure gradient ($\frac{dp}{dx}$>0), fluid flows until the point where it can withstand the centrifugal inertial forces. When the balance between pressure and inertial forces is distorted, BL starts to separate from the surface (point D) and flow cannot reach stagnation

pressure (point F). Due to pressure difference between front and rear sides, drag force forms. Even if we consider a flow with very small viscosity, there is a net drag acting on the body independent from viscosity term μ. BL separation can be observed on any curved surfaces and separation point depends on the curvature radius. When an object has small curvature radius, there will be high centrifugal forces that flow cannot withstand. Streamlined bodies like airfoils are specially designed to prevent BL separation which can cause stall condition (significant increase in drag force and sharp decrease in lift force) on the blade so, a flow over a bluff body inside an adverse pressure field will definitely be more prone to BL separation than a flow over an airfoil inside favorable pressure gradient ($\frac{dp}{dx} < 0$). The size of the wake region after the separation point is also depends on the characteristics of the flow other than curvature radius of the body. Due to high kinetic energy associated to swirling and random motions inside a turbulent BL, flow can move further along the curved surface and creates a narrow wake zone after separation. Drag that is generated from pressure difference due to BL separation will be lower inside turbulent BL even though it has higher friction than flow inside a laminar BL due to high shear related with turbulent flow.

On bodies with sharp edges like PV trackers, BL separates from corners which brings us to the topic of vortex shedding. Vortex shedding is basically alternating pressure change around the body due to boundary layer separation from opposite parts of the body. This phenomenon can typically be observed in flows with sharp edge separation and it causes fluctuating force that can damage the object. Fluctuation frequency is directly associated to Strouhal relation; $f_s = St\frac{U}{D}$, D is body dimension, U is mean flow velocity and St is Strouhal number which depends on the shape and Re number. If f_s becomes equal to natural frequency of the system for some wind velocity, the object starts to vibrate in resonance condition. This effect is called lock-in and amplitude of the vibration may reach very high values. Flow speed at lock-in is called Strouhal speed and can be calculated with using this formula; $U_{st} = \frac{f_n D}{St}$, where f_n is natural frequency of the system. We should also know that, U_{st} is not the only velocity that makes f_s equal to the system natural frequency, there is a velocity range that causes lock-in effect. Inside this velocity range immersed body vibrates with high amplitudes and eventually it may experience fatigue failure. To prevent this to happen, engineers are introducing disturbances on the structure to decrease the coherence of vortex shedding frequency along the body surface. Created unbalance prevents f_s to match with the frequency of any section along the body and reduces the vibration amplitude. The most typical example for this application is wrapping wire around immersed cylinders like chimneys or antennas. Another method to

reduce vortex shedding for rectangular bodies like PV panels, is using rounded edges rather than sharp ones. Using rounded edges reduces the size of the vortices and shortens the wake region in the downstream of the body. These two applications can be seen in figures 2.11 and 2.12, visual aspects of vortex shedding can also be seen in figures 2.13 and 2.14. Additionally, table 2.2 shows Strouhal numbers of some of the most typical geometries.

Figure 2.11 Helical wrapping to prevent vortex shedding

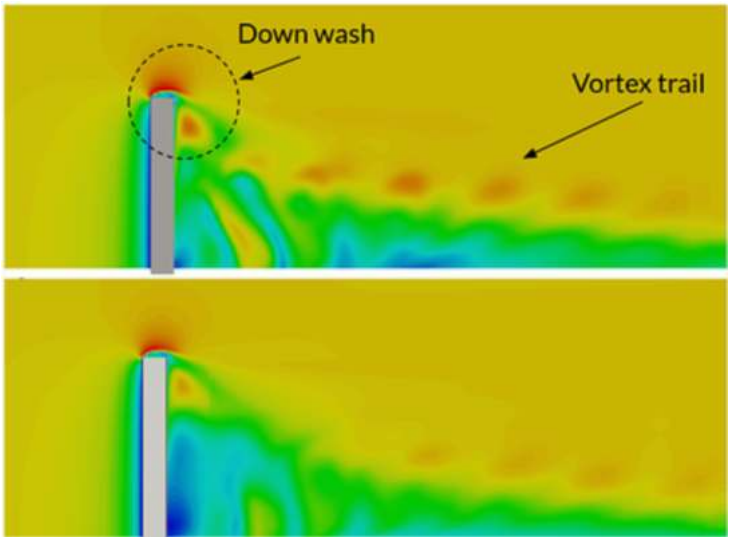

Figure 2.12 Corner vortex shedding on rectangular bodies. Slightly reduced effect in 2nd picture is the result of rounded edge.

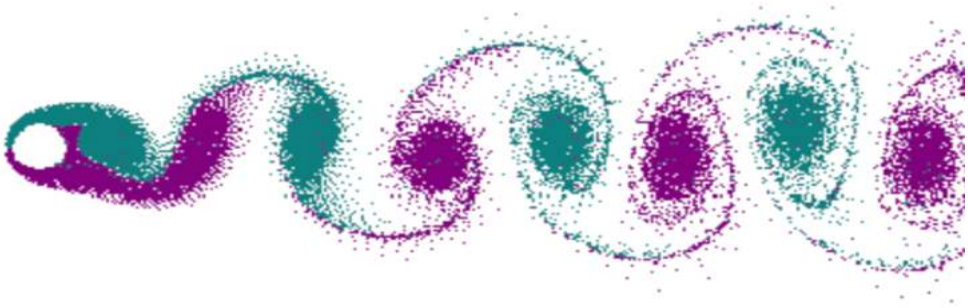

Figure 2.13 Vortex shedding behind a cylinder

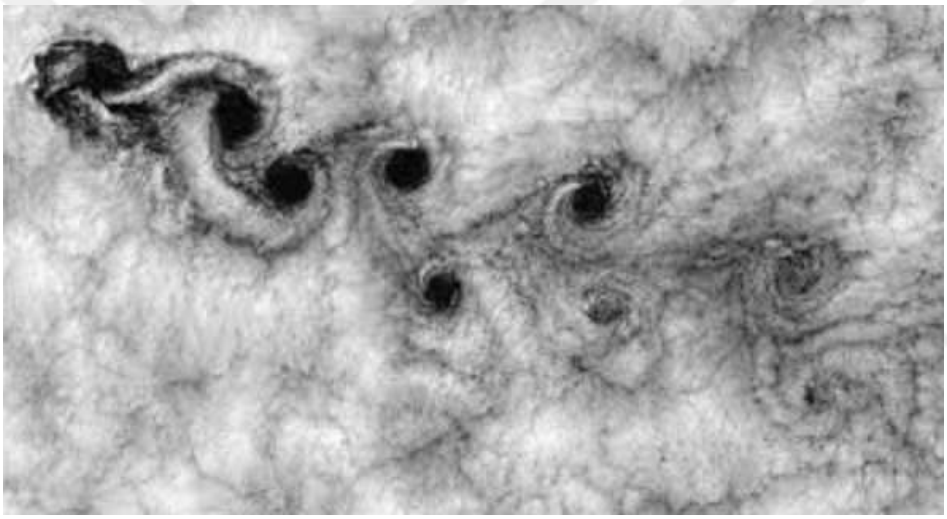

Figure 2.14 Meteorological observation of vortex shedding

Section Shape	→ ◁	→ ▷	→ ⌊	→ ⌐	→ ⊣	→ $\frac{a}{b}$=0.65	→ ◁	→ ▷	→ ◇
St_{∞}	0.19	0.15	0.14	0.14	0.15	0.13	0.19	0.12	0.13

Table 2.2 Strouhal number for different cross sections

2.3 Introduction to Wind Tunnel Testing

One of the most common methods to investigate wind effects on a structure is testing it in a proper wind tunnel facility by creating similar wind conditions. Although full scale testing is the most reliable way to understand aerodynamic behavior of a body, it is usually not feasible to perform because of the high costs related with the method or the size of structure to be tested such as buildings, bridges, stadiums etc. So, using reduced scale models inside a wind tunnel test section makes it more feasible to investigate civil engineering structures and unusual shaped bodies like solar panels which are not well covered by wind engineering codes.

The first enclosed wind tunnel invented by British aero engineer Frank Wenham (1824-1908) in 1871. It was quite simple design with 3.7 m length and maximum of 17 m/s wind speed. The popularity of wind tunnel studies increased in early 20th century in parallel to developments in aviation industry. Today, world's most comprehensive wind tunnels were built by NASA to test aerospace vehicles and aviation systems. Despite the different wind tunnel designs around the world, an operational wind tunnel has four fundamental parts;

- A contoured duct to control the passage of the working fluid through the tunnel.
- A drive system to move the working fluid
- A test section to mount a reduced or full-scale model
- Instrumentation to make necessary flow measurements

Among the all wind tunnel types, ABL wind tunnels are especially important for testing civil engineering structures because they can simulate natural wind flow conditions around a body with an advantage of full control on the wind. By using active or passive turbulence generating elements, similar boundary layer conditions with matching turbulence intensities can be created in ABL wind tunnels. However, reliability of wind tunnel tests depend on geometric, kinematic and dynamic similarity between the scaled model and the real structure [13]. To satisfy geometric similarity, the model has to be the reproduction of every shape on the real body that has aerodynamic relevance within a pre-determined scale. In addition to that, kinematic and dynamic similarity can only be satisfied by the equality of dimensionless parameters. These dimensionless parameters are obtained by grouping relevant dimensional variables according to physical laws related with the test. This method is called Buckingham pi theorem. It helps the engineer by reducing the number of dimensional variables to be dealt and ensures similarity when the equality of the dimensionless parameters that are coming

from the model and the real structure is obtained. Table 2.3 shows common variables and dimensionless groups in wind tunnel applications.

Group	Name	Interpretation	Application
Reynolds number, Re	$\frac{\rho U D}{\mu}$	$\frac{\text{inertia}}{\text{viscous}}$	Generally of importance in all types of fluid dynamics problems
Froude number, Fr	$\frac{U^2}{gD}$	$\frac{\text{inertia}}{\text{gravitational}}$	Problems where both elastic and gravity forces contribute to the stiffness
Strouhal number, St	$\frac{fD}{U}$	$\frac{\text{oscillation}}{\text{mean speed}}$	Oscillating flows (vortex shedding), see also reduced frequency and reduced velocity
Mach number, Ma	$\frac{U}{c}$	$\frac{\text{inertia}}{\text{compressibility}}$	Important only if compressibility of the flow is important ($Ma > 0.3$)
Mass ratio	$\frac{m_a}{\rho D^2}$	$\frac{\text{model mass}}{\text{flow mass}}$	Important in vibrations problems
Scruton number, Sc	$\frac{2\pi m\zeta}{\rho D^2}$	$\frac{\text{dissipative}}{\text{flow inertia}}$	Product of the mass ratio and critical damping ratio
Cauchy number, Ca	$\frac{E}{\rho U^2}$	$\frac{\text{structure internal force}}{\text{flow inertia}}$	Used for scaling structure stiffness
Force coefficient (drag), C_D	$\frac{F_D}{\frac{1}{2}\rho U^2 DL}$	$\frac{\text{drag force}}{\text{dynamic pressure}}$	All aerodynamics problems
Pressure coefficient, C_p	$\frac{p-p_s}{\frac{1}{2}\rho U^2}$	$\frac{\text{surface pressure}}{\text{dynamic pressure}}$	All aerodynamics problems

Table 2.3 Common dimensionless parameters

To understand which dimensionless groups we should use during the test, the structural behavior of the model must be understood. If we are working with aeroelastic models such as suspension bridges, dynamic properties of the structure are required to be scaled, so we must use the dimensionless parameters that are containing mechanical properties of the structure, mass (m), damping ratio (ζ) and earth's gravity (g) alongside flow properties such as density (ρ), wind speed (U), viscosity (μ), frequency (f). On the other hand, if rigid models are used, like the solar panel models that we used in the test, only requirement is matching the flow conditions between the real and simulated cases, therefore using dimensional flow variables is sufficient to get required dimensionless parameters which are Reynolds number, Strouhal number and force/pressure coefficients.

This is the end of chapter 2, all theoretical concepts that are related to the aerodynamic investigations of PV trackers are introduced and explained in this chapter. Following chapter will introduce the test facility, set up and PV tracker models used during this study.

Chapter 3. Wind Tunnel Test

3.1 GVPM, Politecnico di Milano WT

Required tests for understanding aerodynamic behavior of PV trackers were held in wind tunnel facility of Politecnico di Milano. Before explaining the test setup and the procedure, brief information about this facility is introduced in this part of the thesis. GVPM is a closed-circuit wind tunnel facility which is located in Bovisa campus of Politecnico di Milano. Vertically arranged layout of the facility provides two test sections, one for boundary layer tests and one for low turbulence and open jet tests. 1.8m diameter, 100kW 14 fans in 2x7 matrix arrangement produce 1.4MW total power inside the tunnel and each fan can be controlled independently. Flow loop inside the tunnel is represented in figure 3.1.

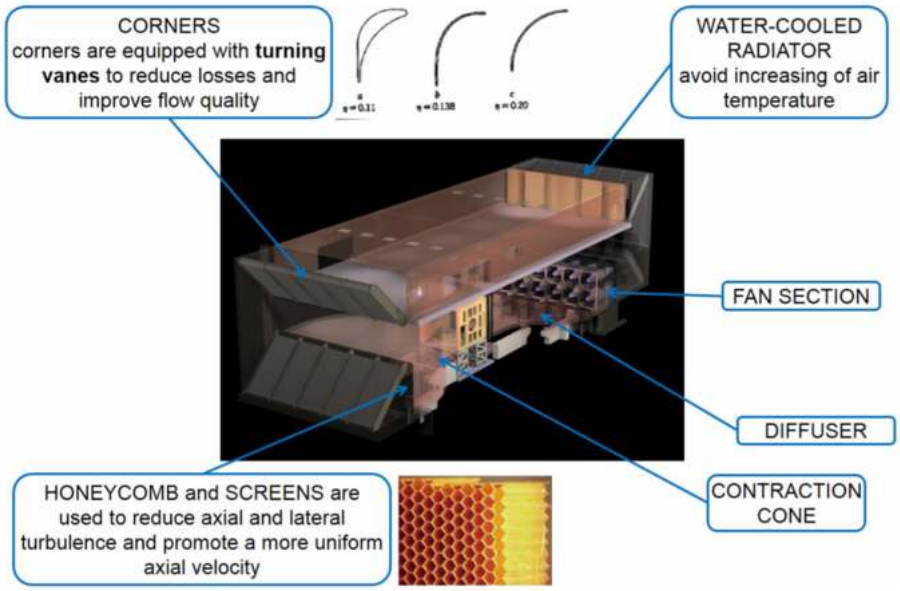

Figure 3.1 GVPM close circuit flow loop

Vertical arrangement with two test sections can be understood more easily with looking at the above figure. The lower part of the loop has the smaller test section with more uniform flow. This section is used for low turbulence tests, honeycomb screen and porosity wire nets create the required uniform flow for this section. The upper bigger test section is used for boundary layer tests. As we know, this is the section where PV trackers are tested. General specifications of boundary layer test section are;

- Dimensions: 35 m long, 13.84 m wide, 3,83 m height

- 16m/s max. wind speed
- %5 mean velocity variation
- Turbulence intensity: 2% (smooth flow condition), up to 35% (BL simulation)
- 13m diameter turntable

Turbulence generation inside the tunnel is provided by spires and roughness elements. 35 m length of tunnel makes possible to simulate different terrain types with different arrangements of these passive turbulence generating elements. Interested readers can learn more about GVPM and previous tests from [14] in reference section.

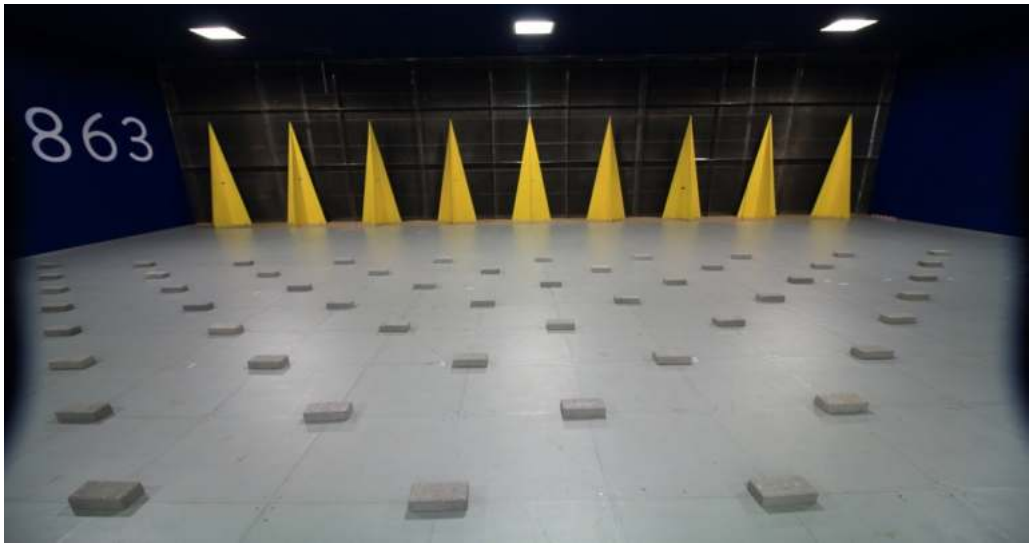

Figure 3.2 Roughness elements and spires in GVPM

3.2 Test Method and Procedure

In this section of the report, information about the test models, flow condition and measurement methods that are used to get aerodynamic load coefficients of PV tracker panels are explained. To calculate aerodynamic coefficients, pressure distributions on panels' lower and upper faces are measured by pressure taps. Full array layout of PV panels consists of 5 rows and 3 columns arrangement with 1/15 rigid models of full-scale PV tracker structures which have dimensions of 3.9x45 m. Pressure readings are made for different ground cover ratios (GCR), wind exposure angles and panel pitch angles. All tested variables are listed in table 3.2. Other than full array test, isolated first row with 3 columns of tracker was also tested to understand pressure tap sensitivity which gives us to minimum acceptable number of taps that we can use on panel measurement sections. Two different tests were organized for this study, the first test was held in October 2017 and the second in April 2018. During the second test, pressure distributions

for panel pitch angles ± 15° for GCR 2.65 and ± 15°, +30°, +60° for GCR 4 were added to the first test results. Recorded raw test data was processed in a Matlab interface named Elaboriamo created by Ing. Stefano Giappin. All discussion about the test results according to changing variables are presented in Chapter 4, this section of the thesis describes only the test organization for measuring the load coefficients on PV trackers.

Quantity	Unit	Full Scale Value	Description
λ_L	-	1/15	Geometric scale of the model
B	m	3.9	Panel chord
H	m	2.11	Reference height of torque tube
ρ	Kg/m^3	-	Air density
α	degree	-	Wind exposure angle
β	degree	-	Panel pitch angle
GCR	-	2.65	Ground Cover Ratio

Table 3.1 List of symbols

TEST	GCR	β	α
Isolated first row	0	-60	0 15 30 45 60 75 90 105 120 135 150 165 180

Isolated first row	0	-45	0 30 45 135 150 180
		-30	0 30 45 135 150 180
		-15	0 30 45 135 150 180
		0	0 30 45
Isolated central tracker	0	+5 -5 -10 -15 -20 -25 -30 -35 -45 -60	0
Full Array	2.65	0	0 15 30 45 135 150 180
		± 15	0 15 30 45 135 150 180

Full Array	2.65	± 30	0 15 30 45 135 150 180
		± 60	0 15 30 45 135 150 180
Full Array	4.00	0	0 15 30 45 135 150 180
		± 15	0 15 30 45 135 150 180
		± 30	0 15 30 45 135 150 180
		± 60	0 15 30 45 135 150 180

Table 3.2 All tested configurations with changing exposure and pitch angles

3.2.1 Flow Conditions Inside GVPM

Wind tunnel test of PV tracker array was performed in ABL test section of GVPM. To ensure the relevance of collected data, characteristics of the natural wind was scaled carefully. This is an essential requirement for the test in order to get correct reproduction of wind effects on PV tracker models. For a correct reproduction of natural wind, variation of mean wind velocity with the height from the ground and wind turbulence characteristics should match with the natural condition. As a general requirement for wind tunnel studies, wind turbulence spectrum of three turbulent velocity components should be represented properly, especially for the low frequency end of the spectrum which contains eddies with high level of energy. Therefore, simulated flow must contain these high energy eddies at low frequencies for a suitable reproduction of natural wind. However, ABL wind tunnels are normally used to test civil engineering structures with model scales between 1/200 and 1/400, but PV panel model scales typically much larger than that. In order to have proper placement of the instrumentation (pressure taps and pvc tubing) and correct reproduction of geometrical details, PV model scales are typically in between 1/20 to 1/50. According to study made by Banks in 2011 [18], when model scale is much larger than the typical flow scales, tunnel cannot simulate the low frequency turbulence correctly. To show the mismatch, Banks presented velocity spectrum graph of 1/40 scale model inside ABL wind tunnel with a flow simulated for 1/300 scale. Area under the curves represents the square of turbulence intensity, and it is evident that it is much lower than the needed value.

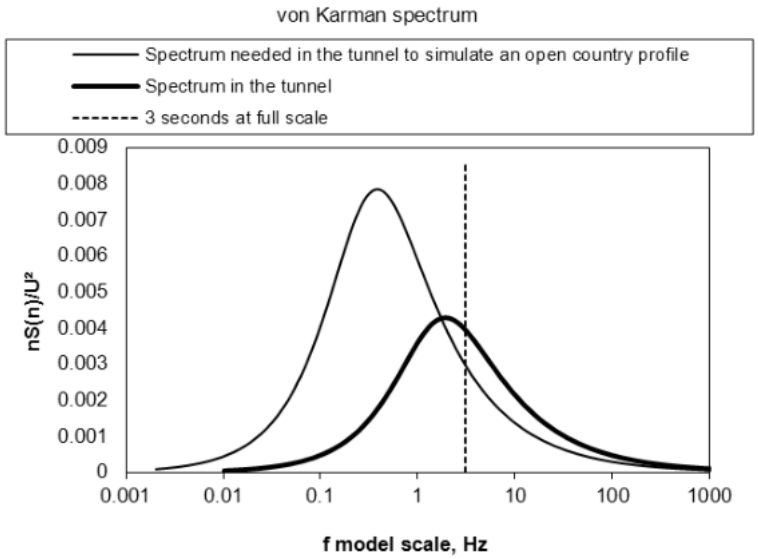

Figure 3.3 Velocity spectrum for 1/40 scale model [18]

To solve this problem, Banks proposes the method of high frequency spectrum matching which is aims to match the curves above 3 second line without worrying about missing energy at low frequencies for two reasons [18];

1. In many jurisdictions, design wind speeds are provided as 3 second gusts. So, we only need to measure what might happen during those 3 seconds. Anything of longer duration than 3 seconds has already been accounted for in the meteorological analysis.
2. If we do need them, these length scales are greater than 10 times the size of the model, and so can be accounted for using quasi-steady theory.

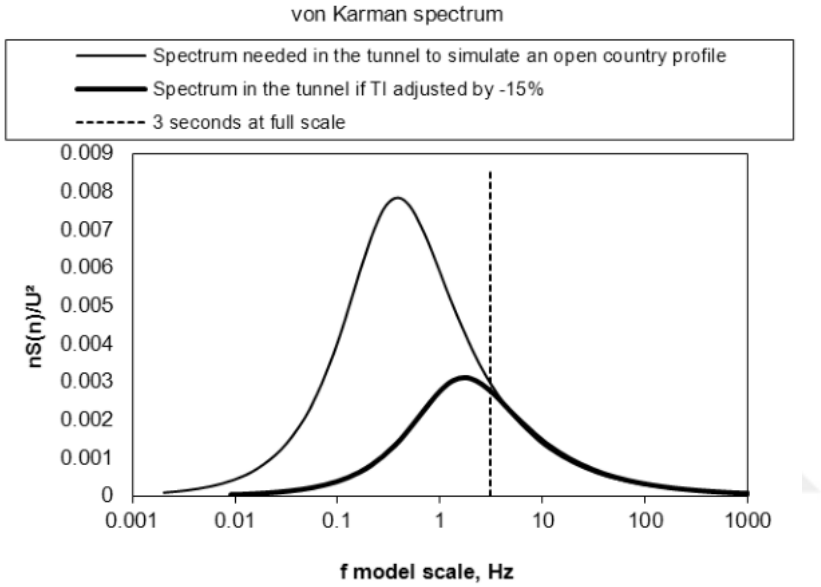

Figure 3.4 [18] High frequency spectrum matching, 1/40 scale model [18]

By reducing turbulence intensity, correct amount of energy can be provided at length scales which matter the most because large scale models are located in higher levels of the boundary layer where turbulence is lower and length scale is higher. This behavior is well described by Dyrbye and Hansen (1997). A very good match between full scale and tunnel can be seen in figure 3.4 for 3 second and smaller wind gust. If we look at the figure 3.6 and 3.7, spectrum comparison of Eurocode and wind tunnel condition created for this test can be seen. Both graphs are also showing adequate match to make the experiment relevant if we consider the above discussion.

Required wind speed measurements inside the tunnel are carried out with using three component multi-hole pressure probe anemometers that is positioned by an automatic traversing system. Selected terrain profile to match with natural condition is Eurocode Category I ($z_0 = 0.01m$). The simulation of natural wind

condition with desired BL behavior and turbulence characteristics is achieved by spires and roughness elements. Spires are located at the starting point of the flow and roughness elements are placed on the wind tunnel floor to create desired velocity profile and turbulence. Comparison between selected Eurocode wind velocity profile and the velocity profile inside the tunnel can be seen in figure 3.5. Vertical profile of wind turbulence intensity is also shown in figure 3.5. Normalization of the wind velocity data is made according to reference torque tube height,2.11m. Furthermore, in figures 3.6 and 3.7, normalized wind turbulence spectrum data at two different heights (2.11 m and 10 m) can be found.

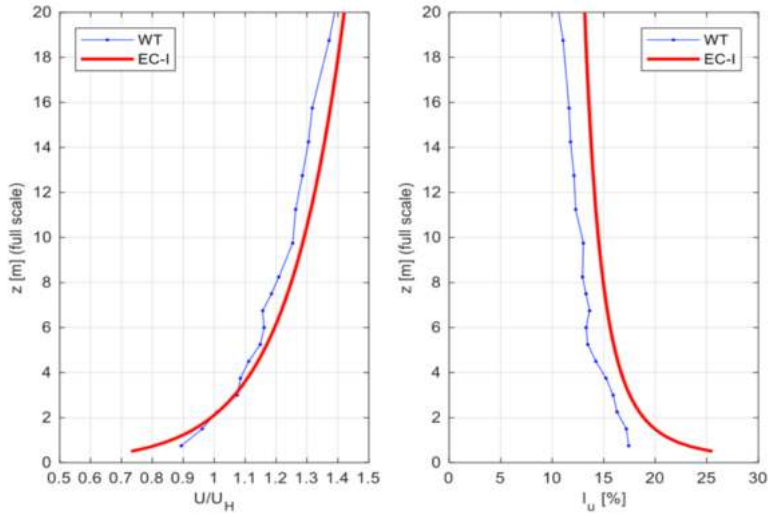

Figure 3.5 (left to right) Mean wind vertical velocity profile and along-wind vertical turbulence intensity profile

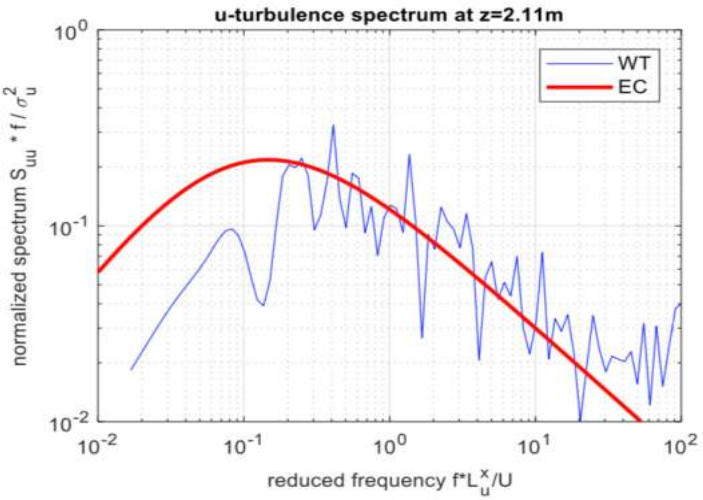

Figure 3.6 Along wind turbulence spectrum at reference height 2.11m

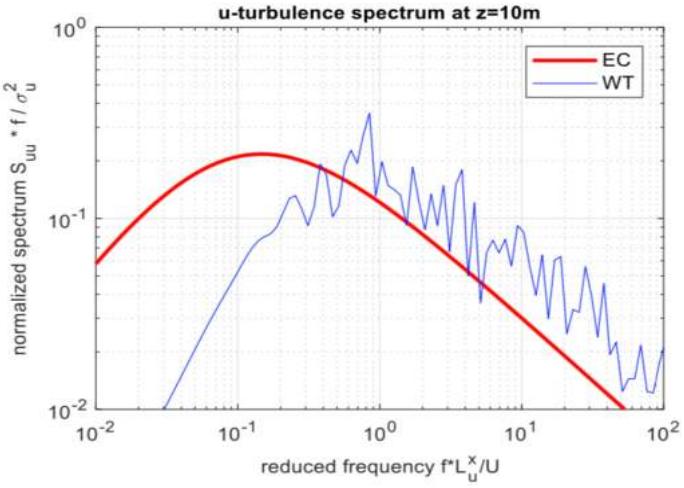

Figure 3.7 Along wind turbulence intensity profile at 10m

3.2.2 PV Tracker Models

Figure 3.8 PV tracker models and the test setup in GVPM

In order to collect pressure data, 1/15 scale PV tracker models are built in GVPM workshop by using plywood. To select a proper length scale, tradeoff between geometric detail and blockage percentage inside the tunnel should be made. This means models should be large enough to reproduce geometrical details that are relevant with the aerodynamic behavior of the structure and they should also be large enough for the required instrumentation while keeping the blockage at reasonable values. Blockage can be found by dividing frontal area of the model to cross-sectional area of the wind tunnel test section and it should not be much higher than 5% [15]. Set blockage limit for this experiment is 8%, if this value is exceeded, distortions on the flow become significant and validity of the test results disappears. So, without exceeding blockage limit, 1/15 scale models

provided enough space for measurement instrumentation and the reproduction of most of the design details provided by the client. It should be noted that, these models are not the exact reproductions of full-scale trackers. There are some minor design simplifications made on the model of the support system and PV panel geometry. The gap between single panels was not reproduced to make it possible to place necessary tubing for pressure taps. Total of 522 pressure taps were used for pressure measurements from inner and outer surfaces of each panel. To calculate pressure difference between bottom and top face of the models, pressure taps are located in the same position in opposite sides. There is one outer and one inner pressure data for each measurement point. By looking at the models, pressure tap locations can be understood from small holes which are indicating the pressure measurement points on each panel. These points can be seen on technical drawings in appendix section. These small holes are connected to the pressure scanners via PVC tubes. Air flow inside each tube was carefully controlled before the test to prevent loss of any pressure data. 4 vertical measurement points are located on one chord of the model and there are total of 8 chords on each panel. Location of these chords were decided upon expected pressure gradients, thus border of the models, where effects of boundary layer separation and vortex shedding create high pressure gradients, were instrumented with higher number of pressure taps to collect more pressure readings from these critical locations. All the measurements were performed using Pressure Systems DTC Initium and Chell Quad-Daq high speed scanning pressure equipment and miniaturized ESP pressure scanner. As stated in GVPM Wind Tunnel Procedures, Rev. 3[15], these scanners contain an array of 32 silicon piezoresistive pressure sensors for each measurement point and analog output of these sensors are multiplexed and amplified within the scanners. The calibration of ESP scanner is maintained through periodic online calibration. During the test, pressure readings are corrected according to frequency response of PVC tubes. This pneumatic link between the taps and scanners is evaluated by an analytical estimation verified by previous experimental investigations developed in GVPM.

Figure 3.9 Photos of pressure taps and connection tubes

To ease the identification of each pressure tap 5 digit code 'SRCrc' is created and the method of this coding is;

- **'S'** indicates the surface where the pressure is measured, **'S'** equals to 1 for outer and 2 for inner surface of the models.
- **'R'** indicates the row of the panel array.
- **'C'** indicates the column of the panel array
- **'r'** indicates the row of the pressure tap on a model.
- **'c'** indicates the column of the pressure tap on a model.

For example, 12311 defines outer face of the first row of the first chord on the model that is located in second row, third column of the tracker array. After instrumentation, the models were placed on the turntable in 5 x 3 matrix arrangement. Only the first three upwind rows at 0° wind exposure angle were instrumented with pressure taps. Other than these 9 instrumented models, 6 dummy models in 2 rows were used to simulated correct boundary conditions during the test.

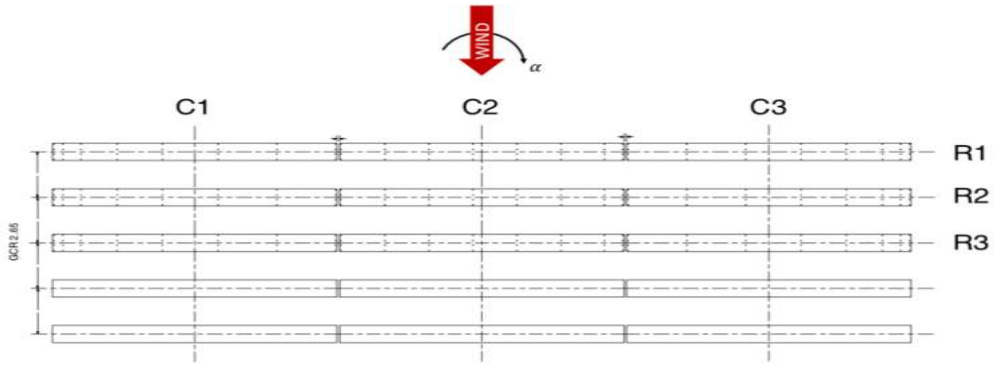

Figure 3.10 Top view of the test arrangement for GCR 2.65

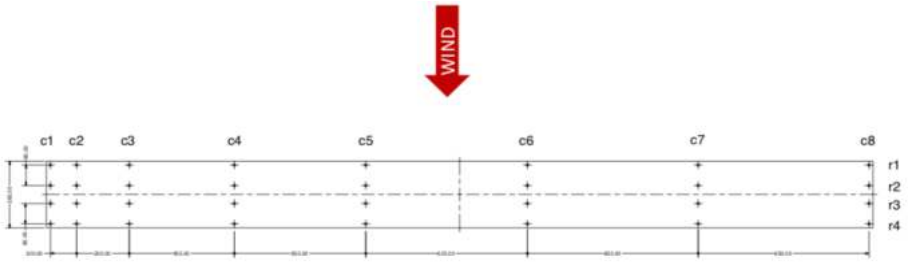

Figure 3.11 Pressure tap locations and chord arrangement for the first column tracker models

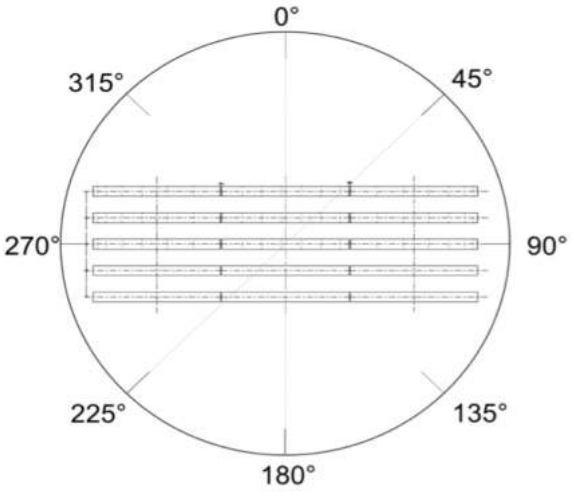

Figure 3.12 Full array arrangement on tunnel's turntable

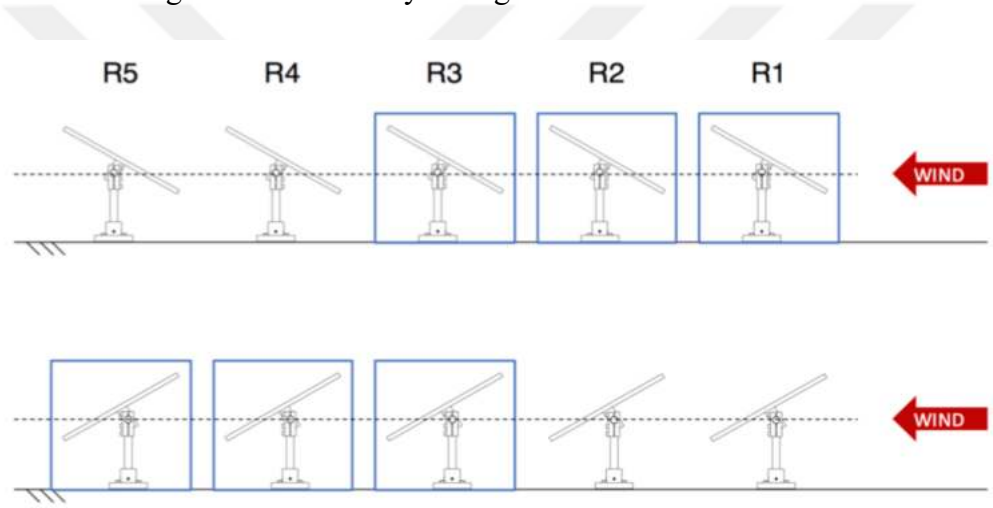

Figure 3.13 Model orientations at 0° and 180° wind exposure angle. Blue boxes are showing the instrumented models for the pressure readings

3.2.3 Equations and Measurements

3.2.3.1 Pressure Coefficients

Each envelope of pressure tap measurements were processed in Matlab and collected as non-dimensional surface pressure coefficients. Pressure coefficients are calculated according to following formulation;

$$C_{p,i}^{1,2} = \frac{p_i - p_0}{\frac{1}{2}\rho U_H^2}$$

p_i is the absolute pressure at the i-th pressure tap, p_0 is the static pressure inside the tunnel, U_H is the mean wind speed at reference height H and ρ is air density. The term in denominator, $\frac{1}{2}\rho U_H^2$, gives mean velocity pressure at refence height H. Numbers 1 and 2 represents the surface where the pressure is measured, again 1 is outer and 2 is inner surface measurements. Calculated pressure coefficients were named with 5-digit code of the pressure tap which the pressure reading was obtained from. With knowing pressure coefficients of each pressure tap, we can calculate the net pressure coefficients for each measurement point on the tracker models;

$$C_{p,i}^{net} = C_{p,i}^{1} - C_{p,i}^{2}$$

The net pressure coefficients were obtained by subtracting the inner pressure coefficient from the outer at each measurement point. The number that is indicating the outer or inner surface of the panel in 5-digit code (1,2) was changed to 3 for naming net pressure coefficient values. For example, net pressure coefficient value that is coming from the subtraction of pressure coefficients 12235 and 22235 is assigned with 32235 5-digit code. Last 4 digit in the code is still representing the measurement location inside the tracker array.

3.2.3.2 Sectional Loads and Zoning

Normal force ($C_{n,j}$) and torque ($C_{m,j}$) coefficients were computed for each chord section. These 8 chords with 8 pressure taps (4 outer, 4 inner) on each are identified with 4 digits that are showing the location of the chord. For example, sections on the model in third row, first column are coded from 3101 to 3108 showing 8 different chords on the model. Third digit, that shows the row number of a pressure tap, is always zero in this method of coding. Normal force coefficient on the model's j-th section can be calculated from;

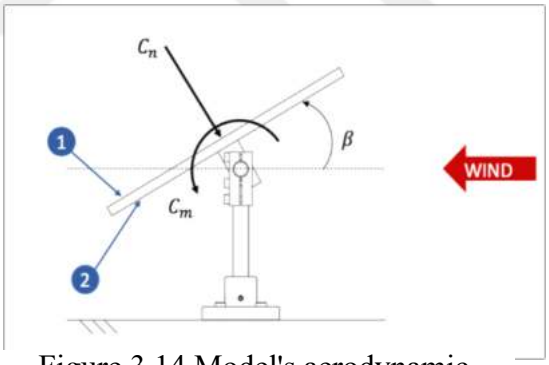

Figure 3.14 Model's aerodynamic loading

$$C_{n,j} = \frac{f_{n,j}}{\frac{1}{2}\rho U_H^2 B} = \frac{\sum_{i=1}^{8} p_i b_i}{\frac{1}{2}\rho U_H^2 B} = \sum_i C_{p,i}\left(\frac{b_i}{B}\right)$$

So, normal force coefficient can be found from the sum of the multiplication of i-th pressures coefficient in j-th chord with the ratio of chord portion assigned to that tap 'b_i' to chord length 'B'. To calculate torque coefficient;

$$C_{m,j} = \frac{f_{m,j}}{\frac{1}{2}\rho U_H^2 B^2}$$

'$f_{m,j}$' is the moment of j-th section on a model. With considering the similarity of loading coefficients, zoning for the model array was performed. In order to not miss any aerodynamic behavior of the models, the first zones selected according to the model's row location inside the full array. As shown in figure 3.15, R1 represents the first upwind and downwind rows, R2 the second upwind and downwind, R3 central row. Further separation was made according to similarity of load coefficients inside the same row. Outside of each instrumented model is named A1 and extends through 8m until A2 zone starts and continues for rest of (37m) the outside column models. Also, all normal force and torque coefficients of central column trackers were assigned to zone A3.

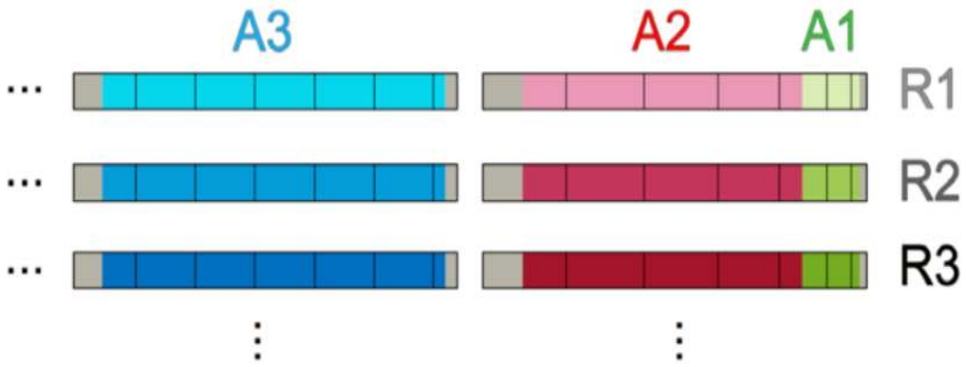

Figure 3.15 Load zone classification for the tracker array

This is the end of chapter 3, all necessary information about the test conditions and PVT model specifications were explained in this chapter. In chapter 4, test data is provided according to peak and min values of normal force and torque coefficients measured for above mentioned zones. Tests for exposure angles between 0°- 90°, represents the pressure readings made during the upwind orientation of the instrumented rows and the data in between exposure angles 90°-180° covers the downwind orientation in the tunnel test section. With using positive and negative pitch angles, models were tested for every location inside the array. Fig 3.12 and Fig 3.13 can be helpful to understand this movement of the tracker array with the rotation of the turntable.

Chapter 4. Results & Discussions

4.1 Isolated First Row Test

During the wind tunnel test in October 2017, single row arrangement was tested to analyze the sensitivity of pressure taps and compare the isolated first row data with standards. This test arrangement is useful for revealing minimum number of pressure taps that are necessary to measure correct sectional coefficients by integration of each tap reading. Less number of pressure taps may lead to loss of significant wind effects, on the other hand, too many pressure taps increase complexity and computational effort related with the test. Sensitivity was analyzed by comparing force coefficients for pressure tap arrangements of 4 and 9 on each side of section 1204 (1st row, 2nd column, 4th chord). Isolated row test is named as GCR0 and only the fourth chord of central tracker have instrumented with additional 5 taps on each side. Measured $C_{n,1204}, C_{m,1204}$ values can be compared for 4 taps and 9 taps in figure 4.1.

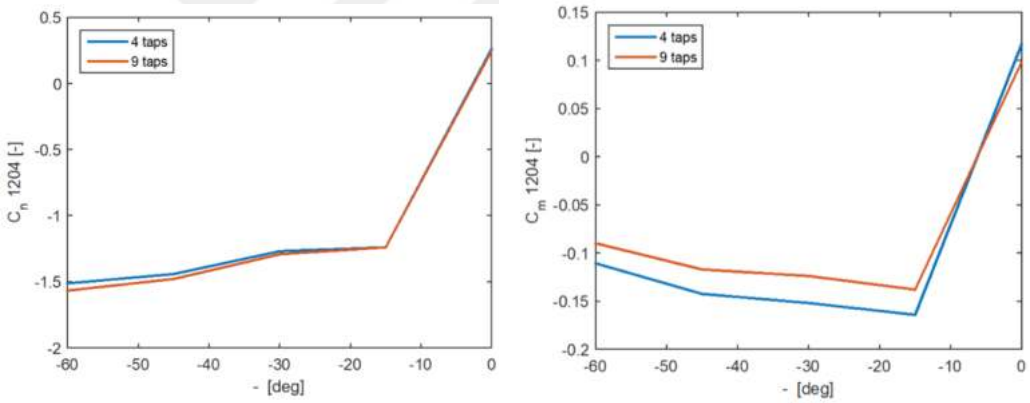

Figure 4.1 Normal force and torque coefficients for section 1204 with 4 and 9 pressure taps

As can be seen from above figures, although there is a small difference at higher absolute values of the pitch angle, 5 additional pressure taps do not change the computed coefficients significantly. Therefore, 4 pressure taps arrangement on inner and outer surfaces was found acceptable for this study.

After sensitivity analyze, zone loads of the isolated first row were compared to proposed standards. To do so, all pressure fluctuations on the models that are induced by fluctuation of incoming wind pressure (turbulence) and flow-body interactions (self-induced turbulence) were normalized according to gust wind kinetic pressure at torque tube height 2.11m. The scaling factor ($sf = \bar{q}_H/\hat{q}_H$)

has been calculated by using the simulated wind profile and it is equal to 0.47. Before presenting load zones, all values were normalized according to wind kinetic pressure with the calculation procedure shown below.

$$C_{p,i}^{1,2} = \frac{p_i - p_0}{\frac{1}{2}\rho U_H^2} = \frac{p_i - p_0}{\bar{q}_H} \Rightarrow C_{n,j} = \sum_i C_{p,i}\left(\frac{b_i}{B}\right) \Rightarrow sf = \frac{\bar{q}_H}{\hat{q}_H} \Rightarrow C_{n,j,s} = C_{n,j} * sf$$

The normalized results for zones A1 and A3 of isolated first row are compared to the results from ASCE 7-10, chapter 27.4.3 and UNI-EN 1991-1-4 section 7.3. ASCE 7-10 chapter 27.4.3 is specially dedicated for wind loads on open buildings with mono slope, pitched, or troughed free roofs and UNI-EN 1991-1-4 sec 7.3 is for measuring wind loads for canopy roofs which is defined by Eurocode as the roof of a structure that does not have any walls. Normally, coefficients in Eurocode standards are normalized according to the height of the roof top, however in this study reference height is considered as torque tube height. Necessary calculations, procedures and tables proposed by ASCE and Eurocode are presented in appendix section. Peak values of normal force and torque coefficients for the isolated row are presented in figures 4.3 and 4.4. In addition to these, comparison of sectional coefficients for A1 and A3 with the standard values can be found in figures 4.5 to 4.8. If we investigate figure 4.3, we can see the increasing trend of C_n with the increasing pitch angle. This is an expected result due to the increase in effective pressure area. Minus and plus signs are only representing the panels facing with wind direction. It can be better understood from figure 4.2. By looking at the wind and force directions, it is not hard to understand why peak absolute values of force coefficient are presented in force coefficient envelopes at max 90°- 180° and min 0°- 90°. In between the 0° starting point and 90° mid-point, wind first touches the inner face (2) of the model and creates negative force coefficient that has a horizontal component in the same direction with the flow. When horizontal component of the force coefficient is in the same direction with the wind, maximum absolute values in each of the envelopes (0°-90°/ 90°-180°) can be reached. A smaller force also appears opposite to the flow direction due to wind flow inside the tunnel, coefficient envelopes of max 0°-90° and min 90°- 180° cover these forces which are in the opposite direction with the flow.

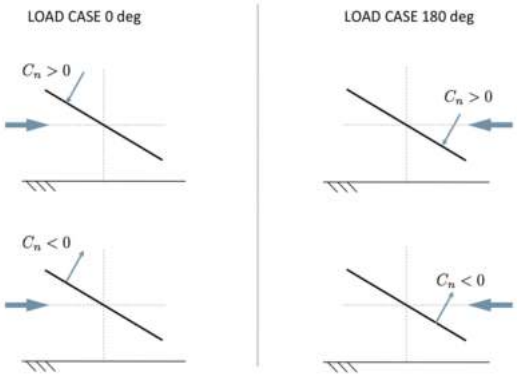

Figure 4.2 Panels facing and direction of negative/positive values of normal force coefficient

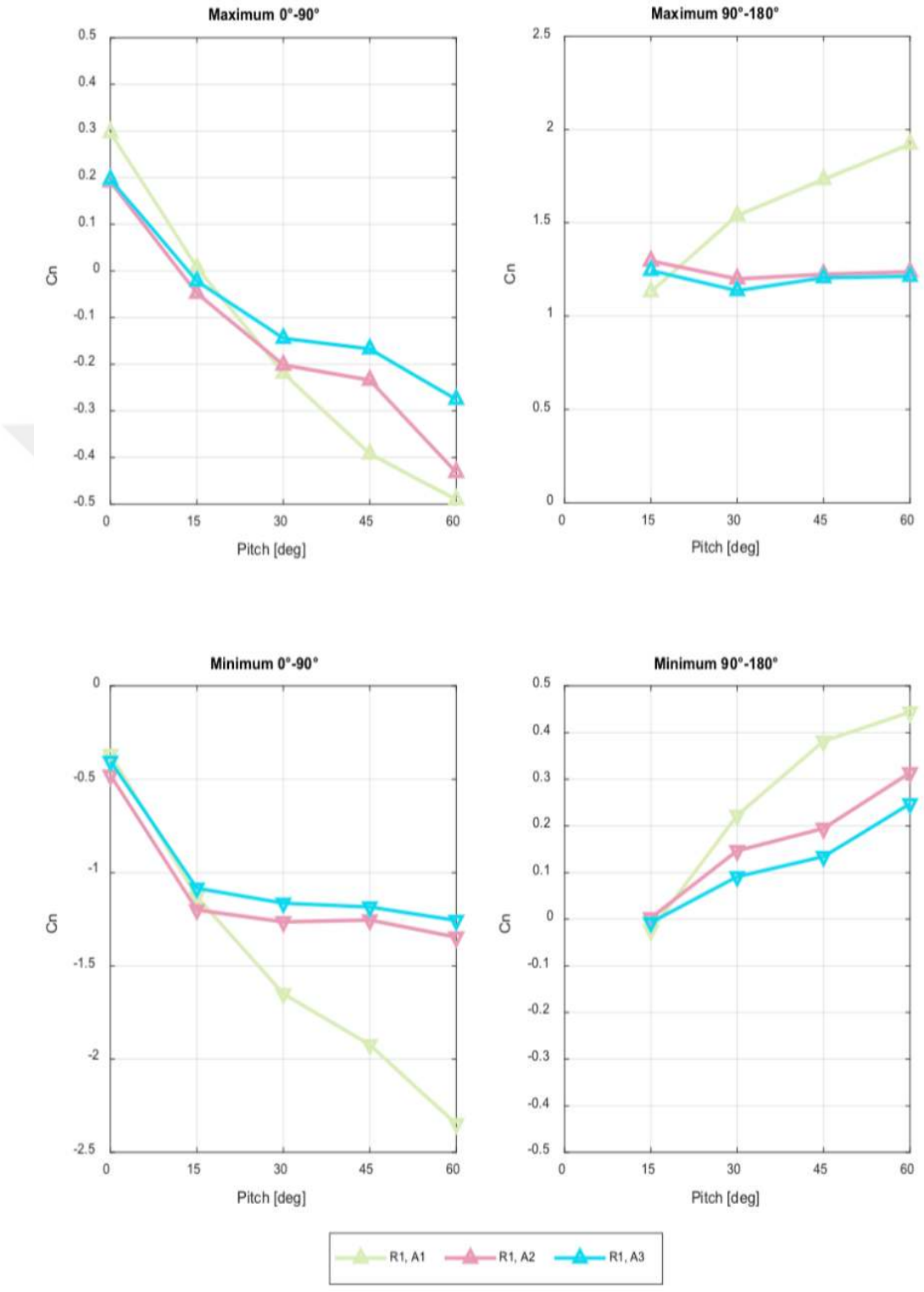

Figure 4.3 Peak normal force coefficients for each load zone on the isolated row

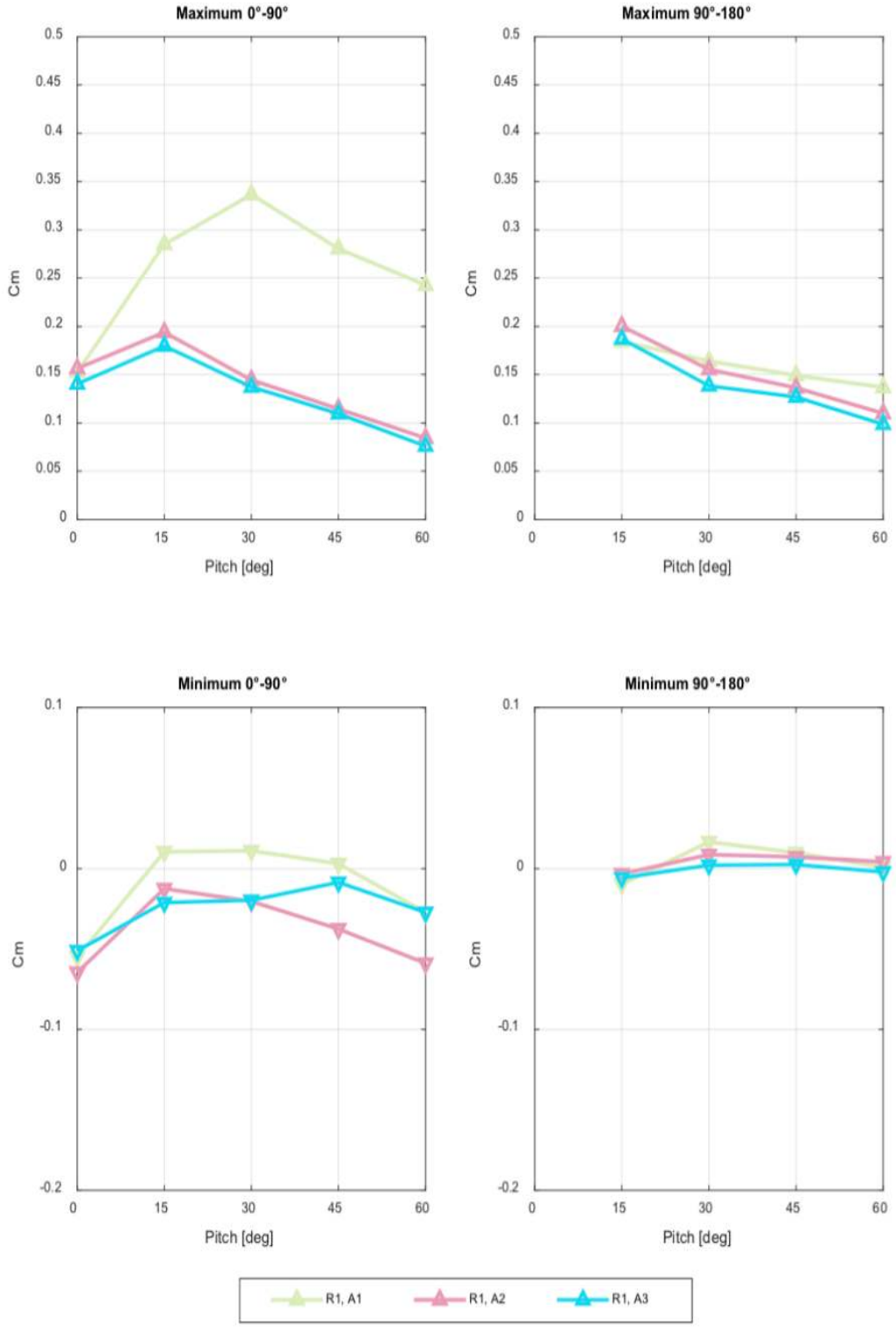

Figure 4.4Peak torque coefficients for each load zone on the isolated row

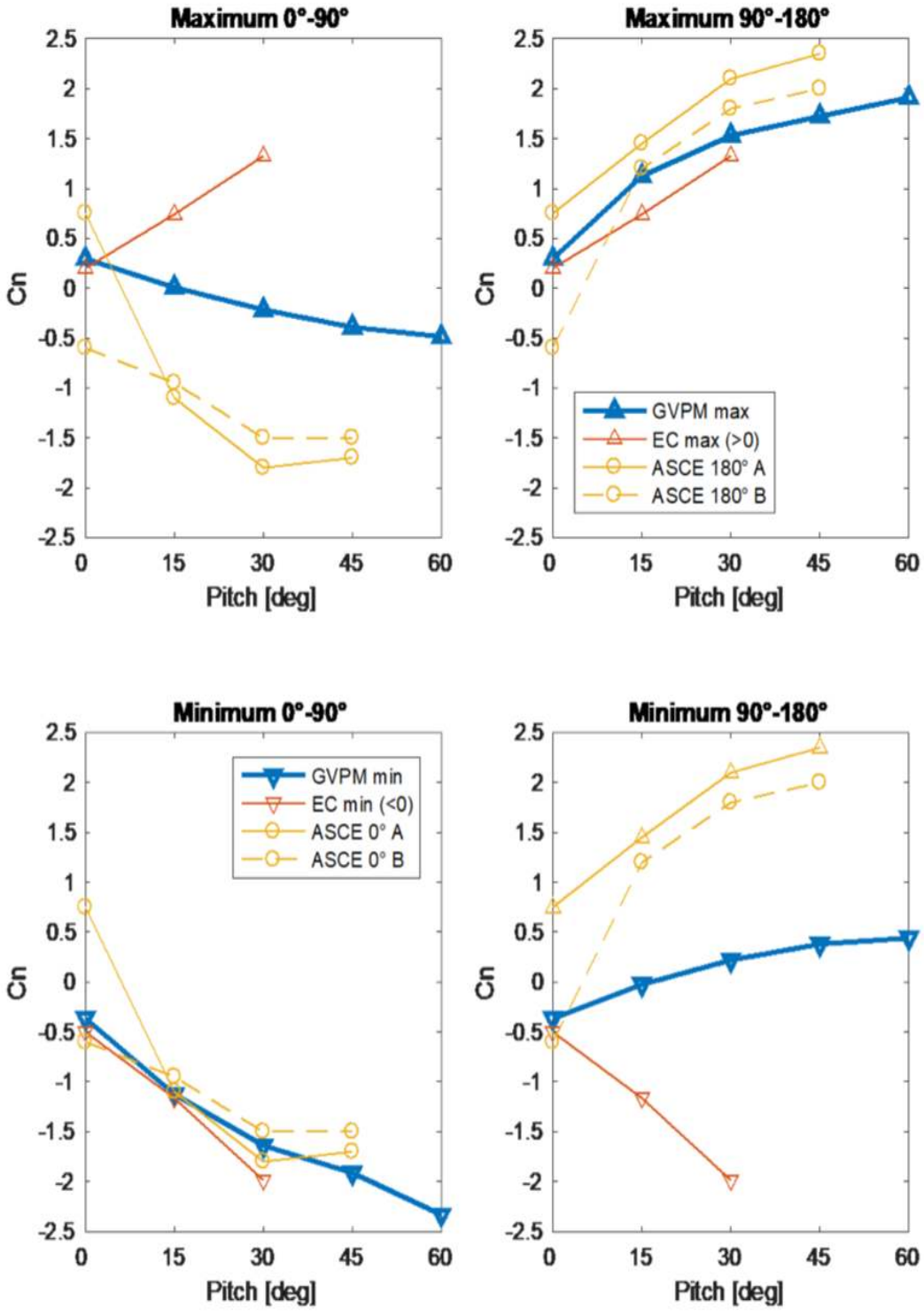

Figure 4.5 Comparison of peak normal force coefficients for A1 of the isolated row with values proposed by standards

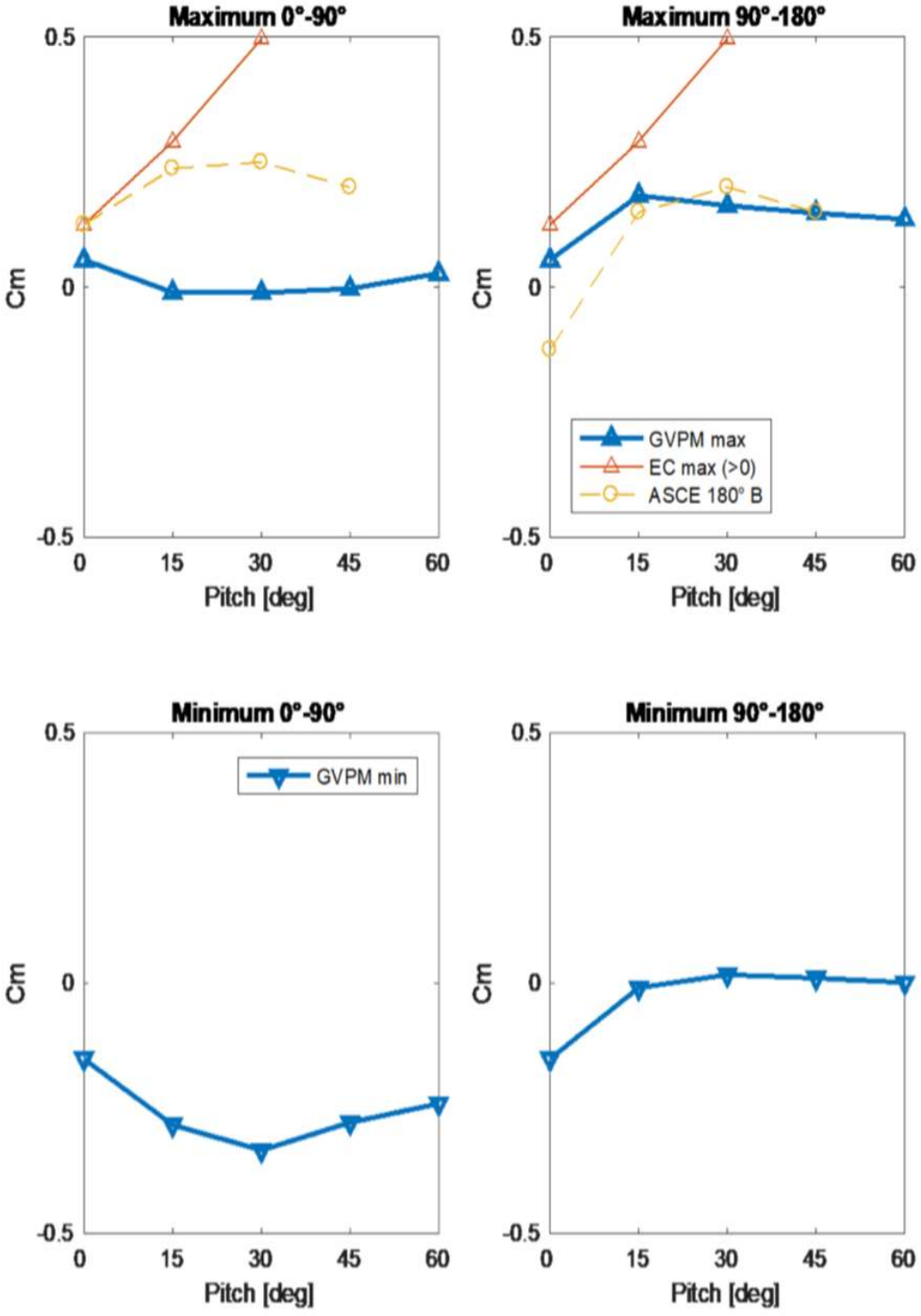

Figure 4.6 Comparison of peak torque coefficients for A1 of the isolated row with values proposed by standards

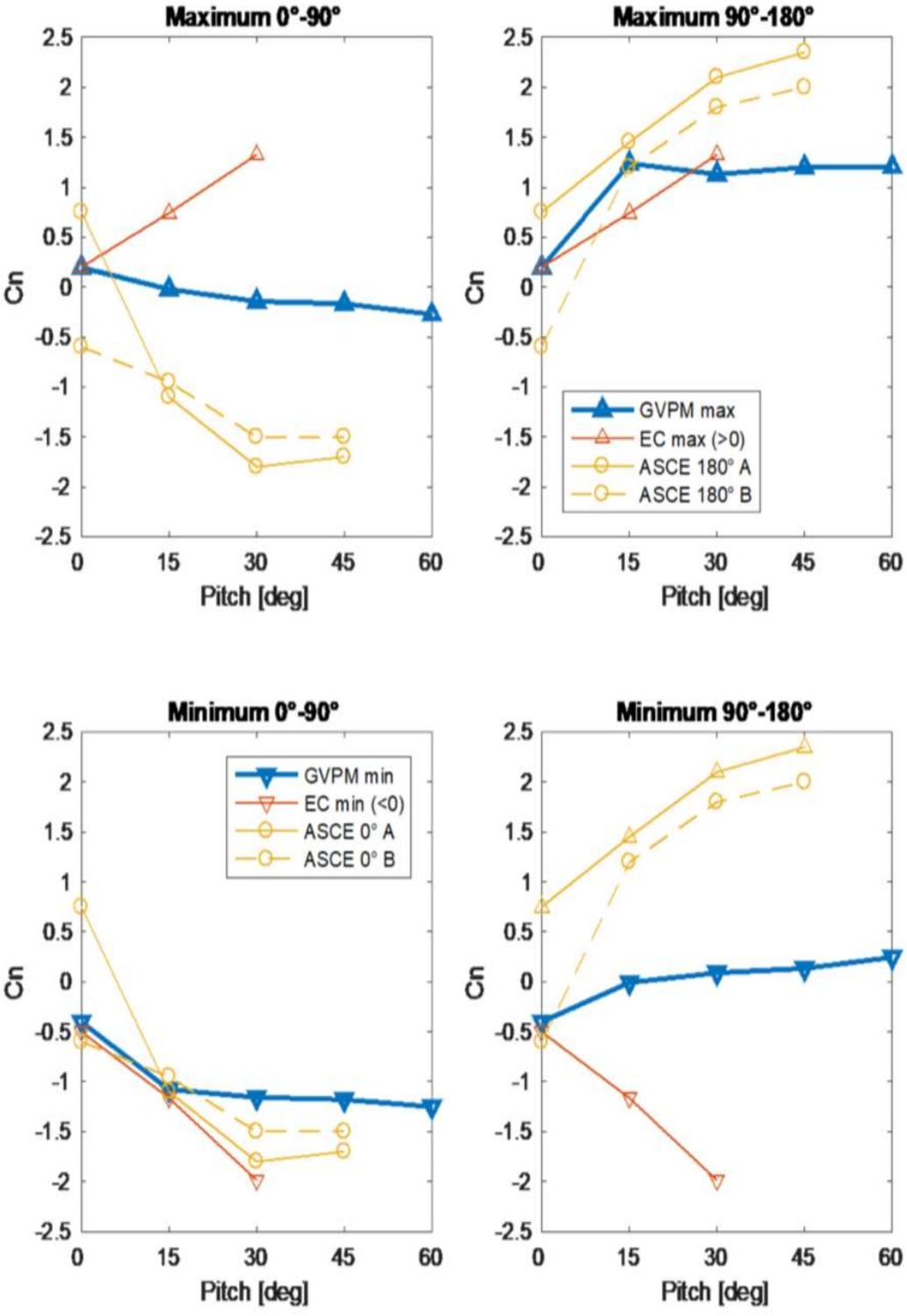

Figure 4.7 Comparison of peak normal force coefficients for A3 of the isolated row with values proposed by standards

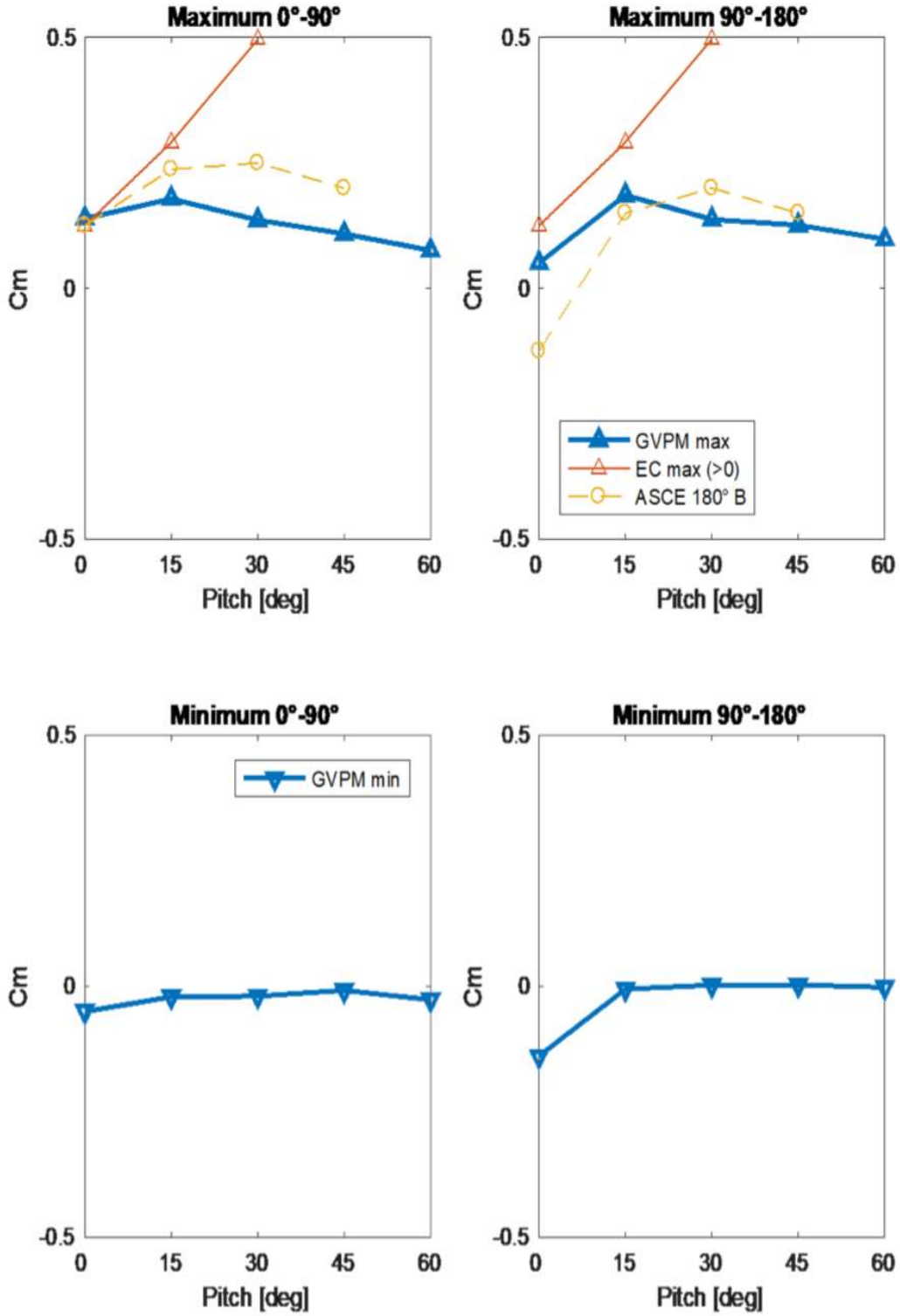

Figure 4.8 Comparison of peak torque coefficients for A3 of the isolated row with values proposed by standards

The highest value of C_n is in zone A1 due to vortex shedding on outer sections of each row. Although A2 and A3 shares almost similar lines in graphs, zone A2 has slightly higher values of C_n than A3.

Even if C_n values increase with pitch angle, the highest values of C_m is experienced at mid values of the pitch angle. This is because increasing pitch angle decreases the torque arm length, and results with decrease in peak torque coefficient for higher values of pitch. If we continue with figures 4.5 and 4.7, it is clear to see the good agreement between ASCE cases A, B, Eurocode standards and the peak coefficient envelopes which have a force coefficient in the same direction with the wind (max 90°-180°/min 0°-90°). Although coefficient values do not overlap, peak values measured in the tunnel for envelopes min 90°-180° and max 0°-90° also follow the same trend with ASCE cases while having a significant difference with Eurocode standards. Almost similar agreements can be seen in figures 4.6 and 4.8, one difference can be noted that reference peak torque coefficients for ASCE is computed by only using case B. In every peak torque coefficient graph, Eurocode standard value takes the highest value compared to tunnel data and ASCE case B.

4.2 Zone Loads

After completing isolated first row tests, full array of 5 x 3 matrix arrangement was set up on the turntable. The first full array test was done in October 2017, afterwards another test was organized in April 2018 to test pitch angles of ± 15° for GCR 2.65 and ±15°, +30°, +60° for GCR 4. At the end of both test, measured data presented in reports prepared by Ing. Alessandro Fontanella, Phd candidate who works with Prof. Marco Belloli. Zone loading graphs presented in this section are full set of results organized by Alessandro for the second test report in July 2018. Graphs are organized under subtitles according to see behavior of the same load zone in different rows and different load zones in the same row. Also, Eurocode type peak coefficient table is prepared to provide better understanding for the critical location inside the array. Although some of the discussion about the graphs is made in this section, effect of each test variable is investigated in Discussion section in this chapter, under dedicated subtitle for each variable.

4.2.1 Same Load Zone in Different Rows

By investigating the same load zone located in 1st, 2nd and 3rd upwind or downwind rows, we see that how aerodynamic loading is changing with row location for different sections inside the array. These data are also useful for comparing load coefficients for upwind and downwind orientation of the array,

so facing of the panels according to incoming wind during 0°-90° and 90°-180° exposures should be considered carefully. It should be remembered that R1 represents the first upwind, last downwind rows, R2 second upwind and downwind, and R3 is for the central row in the tracker array. In order to remember zoning of the full array, readers may visit back to related section (3.2.3.2) in chapter three. Graphs presented in following pages are separated in two subtitles according to two different GCR values that were used during the test. In each subtitle, two graphs ($C_n \; vs \; \beta$, $C_m \; vs \; \beta$) for each load zone, total of 6 peak load coefficient graphs are provided. Peak load coefficients for the same zone in different rows are compared in each graph.

Let's start with figures 4.9, 4.11 and 4.13, peak normal coefficient graphs for GCR 2.65 model arrangement in tunnel test section. The first thing can be noticed immediately is high values of peak C_n recorded at 15° pitch inside the envelopes of max 0°-90° and min 90°-180°. If we consier the almost linear increase in C_n with the pitch angle during the isolated row tests, it will not be hard to relate this sharp increase at low pitch angles with the row interactions inside the array. In addition to this irregularity in max 0°-90° and min 90°-180° graphs, very small C_n values at 15° pitch in min 0°-90° and max 90°-180° graphs implies a pressure increase on the downwind surface of models. It is the surface facing the interior rows of the array. However, for higher degrees of pitch angle, this fluctuation in pressure disappears, peak loading direction and wind direction matches again. For exposure between 0° and 90° at high pitch angles, positive C_n values are very small and close to each other in every row, however, negative C_n values R1 takes the highest absolute value in every load zone when we compare it with the inner rows. It is an expected result because R1 represents the most outer rows in the array. Although C_n increases with pitch angle for R1 in every load zone, it is not the case for R2 and R3. This opposite trend can be seen better in graphs of A2 and A3, there is a slight decrease in C_n at high pitch angles due to increase in blockage of the first row. Because of being located on the most outer sections of each row, A1 is under exposure of cornering winds which increase load on the surfaces with creating corner vortices. So, it is also an expected result for A1 to reach the highest value of peak C_n in graphs. We can see the same trends for 90°-180° exposures in opposite direction. One important difference that can be compared is loading values at 15° pitch angle. Even if the highest measured absolute values are in min 90°-180° graphs for R1 at 15°, peak C_n decreases significantly in subsequent rows for zone A2 and A3. This trend is not that clear in max 0°-90° graphs despite the fact that the flow interaction which is creating the high loading at 15° has the same effect in opposite direction during 0°-90°

exposure. Therefore, differences between two faces of the model, such as torque tube and support system, may be the cause of this dissimilarity.

Peak C_n values for GCR 4 can be found in figures 4.15, 4.17 and 4.19. Many of the above discussions also hold for the graphs of GCR 4. An important difference can be seen in max 0°-90° and min 90°-180° graphs is the significant increase in peak C_n. Decreasing trend between 15° and 30° seems to be loss for GCR 4 in A1. For zone A1, absolute value of C_n increases with pitch angle in each row for both exposure ranges. Even if this increase settles in graphs of A2 and A3 for interior rows, load on R1 keeps increasing with pitch angle and creates high loads in both directions during 0°-90° exposure. By looking at min 90°-180° graphs, we can say that the same condition is not experienced in A2 and A3 during 90°-180° exposure because trends in these graphs are almost similar with the ones presented in GCR 2.65. One last thing that can be pointed from GCR 4 C_n graphs, is the significant decrease in the values measured from R3 in max 90°-180° and min 0°-90° graphs. Sharp increase between 15° and 30° seems like swapped with steady increase between 15° and 60°. Even if this steady increase is enough for having almost similar peak C_n with GCR 2.65 at 60° in zones A2 and A3, peak C_n values at 30° are significantly smaller in all zones when compared to values measured for GCR 2.65.

To investigate peak torque coefficients, we need to look to figures 4.10, 4.12 and 4.14. Trend of peak C_m is almost similar for different rows in the same load zone. Measurements made during isolated first row test matches with the values obtained from the load zones located on the first row. In C_n graphs, the highest value is measured from R1 in every condition, however the highest peak C_m is on R2 for zones A2 and A3 at 30° pitch during 0°-90° wind exposure. This difference can be seen clearer in GCR 4 because in GCR 2.65, values measured from different rows are too close to each other for comparison.

4.2.1.1 GCR 2.65

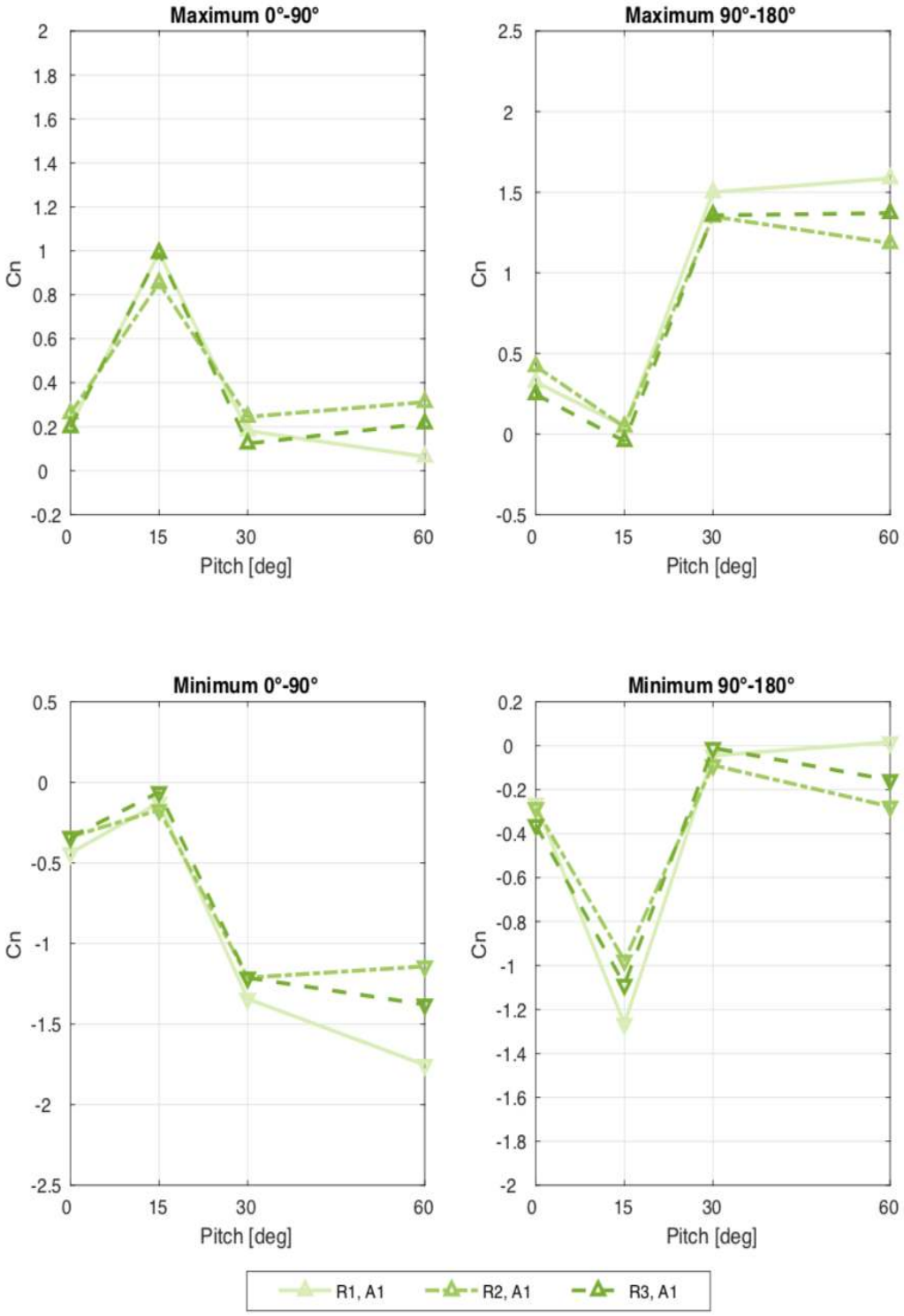

Figure 4.9 GCR 2.65 Zone A1 peak normal force coefficients for three instrumented rows

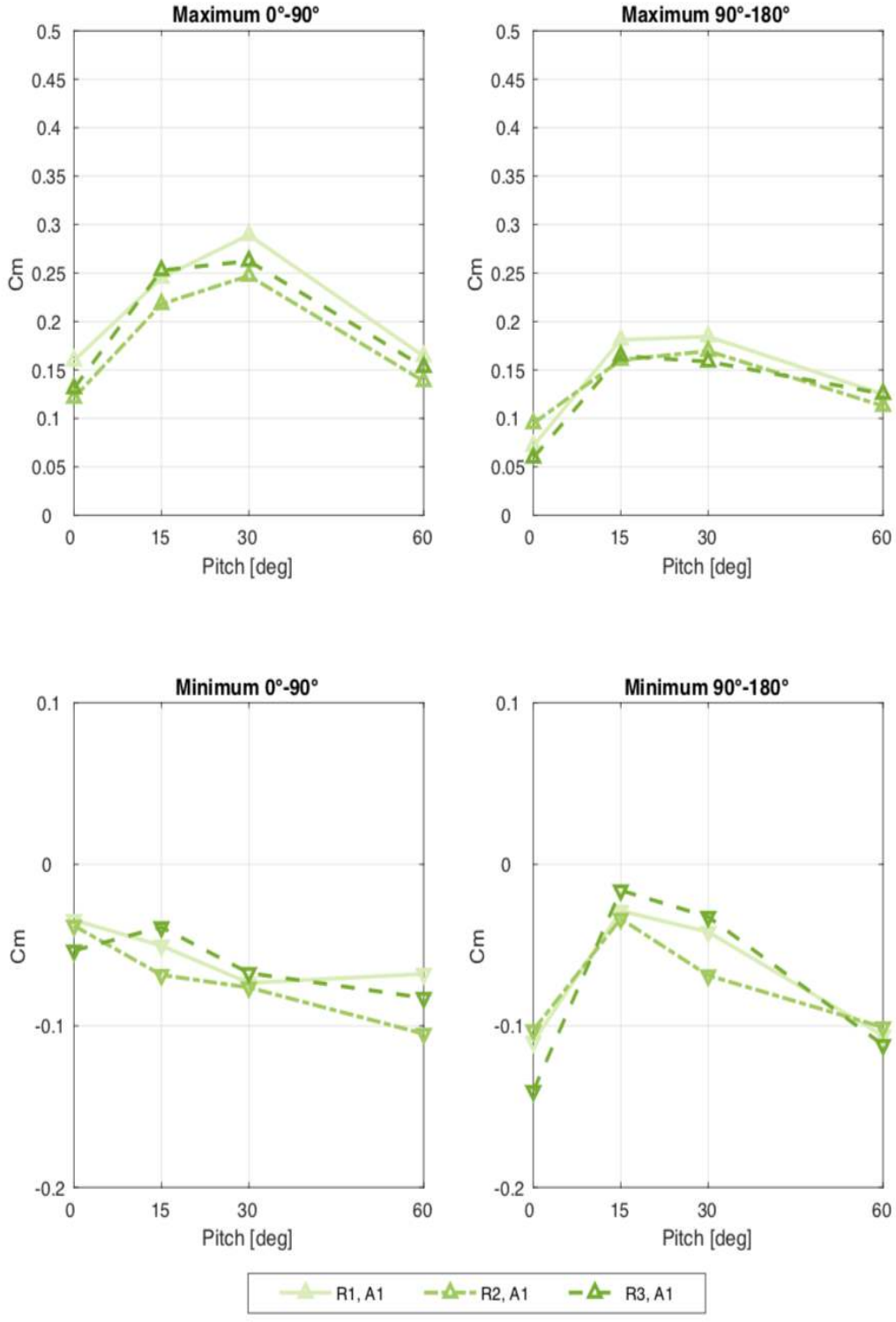

Figure 4.10 GCR 2.65 Zone A1 peak torque coefficients for three instrumented rows

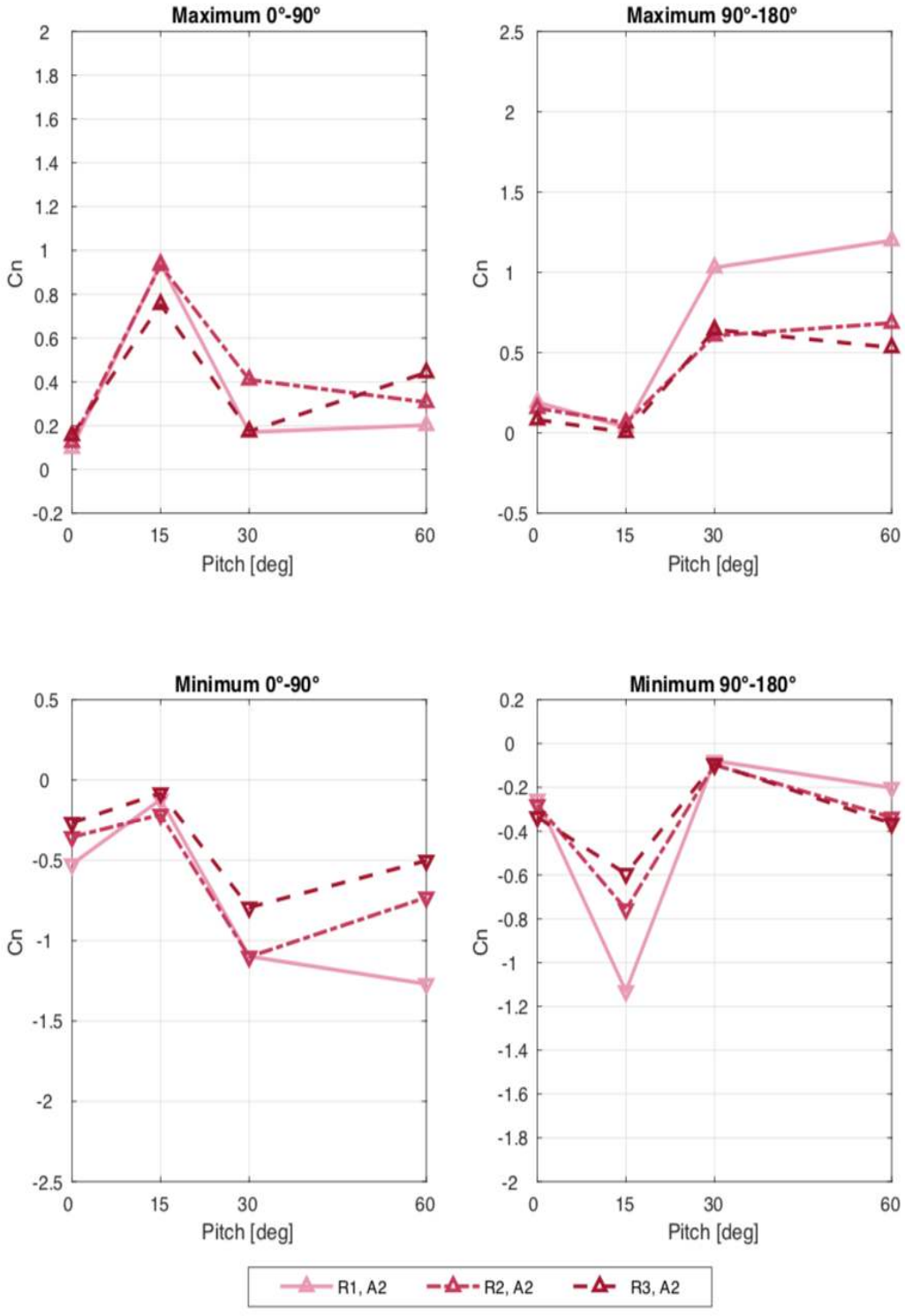

Figure 4.11 GCR 2.65 Zone A2 peak normal force coefficients for three instrumented rows

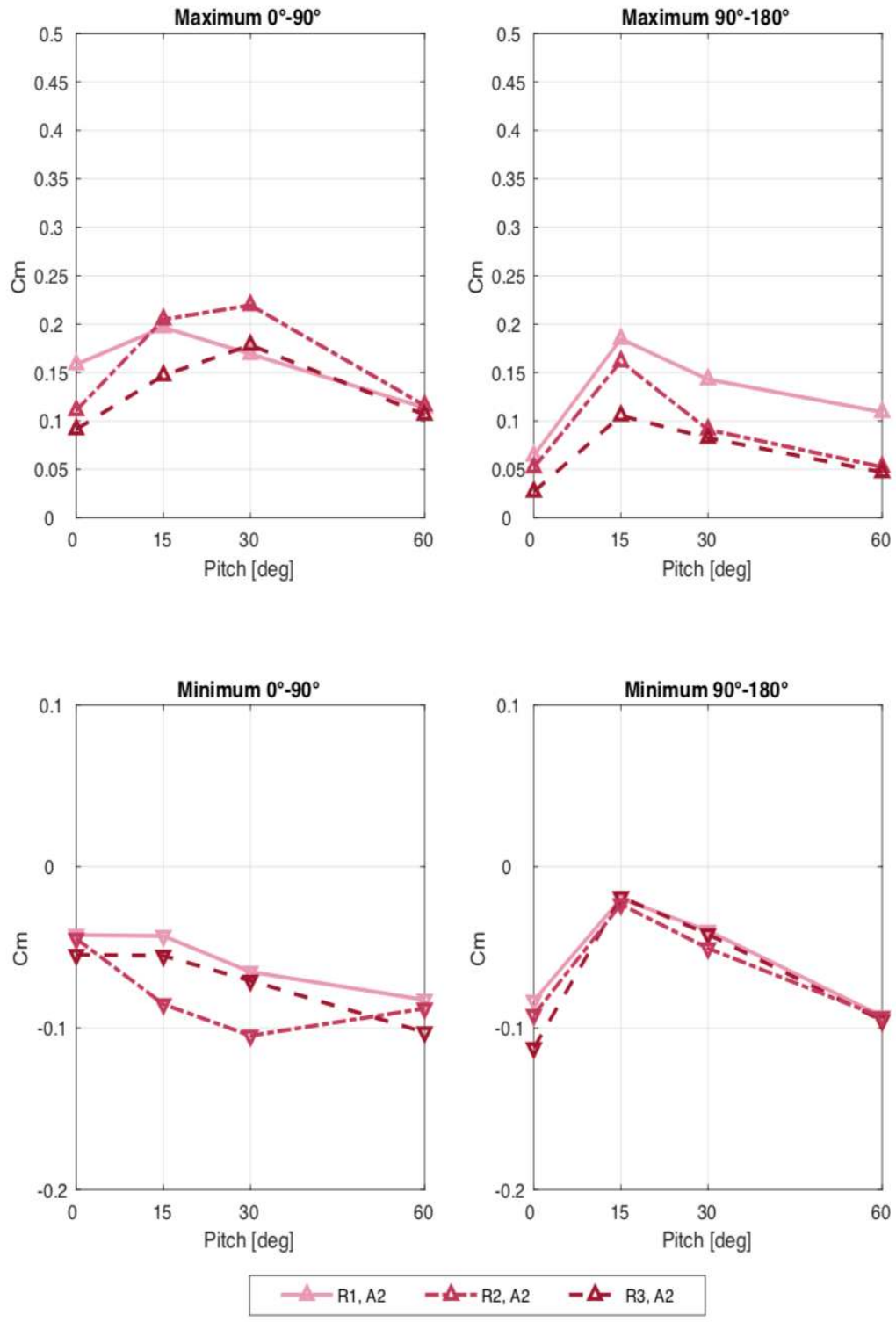

Figure 4.12 GCR 2.65 Zone A2 peak torque coefficients for three instrumented rows

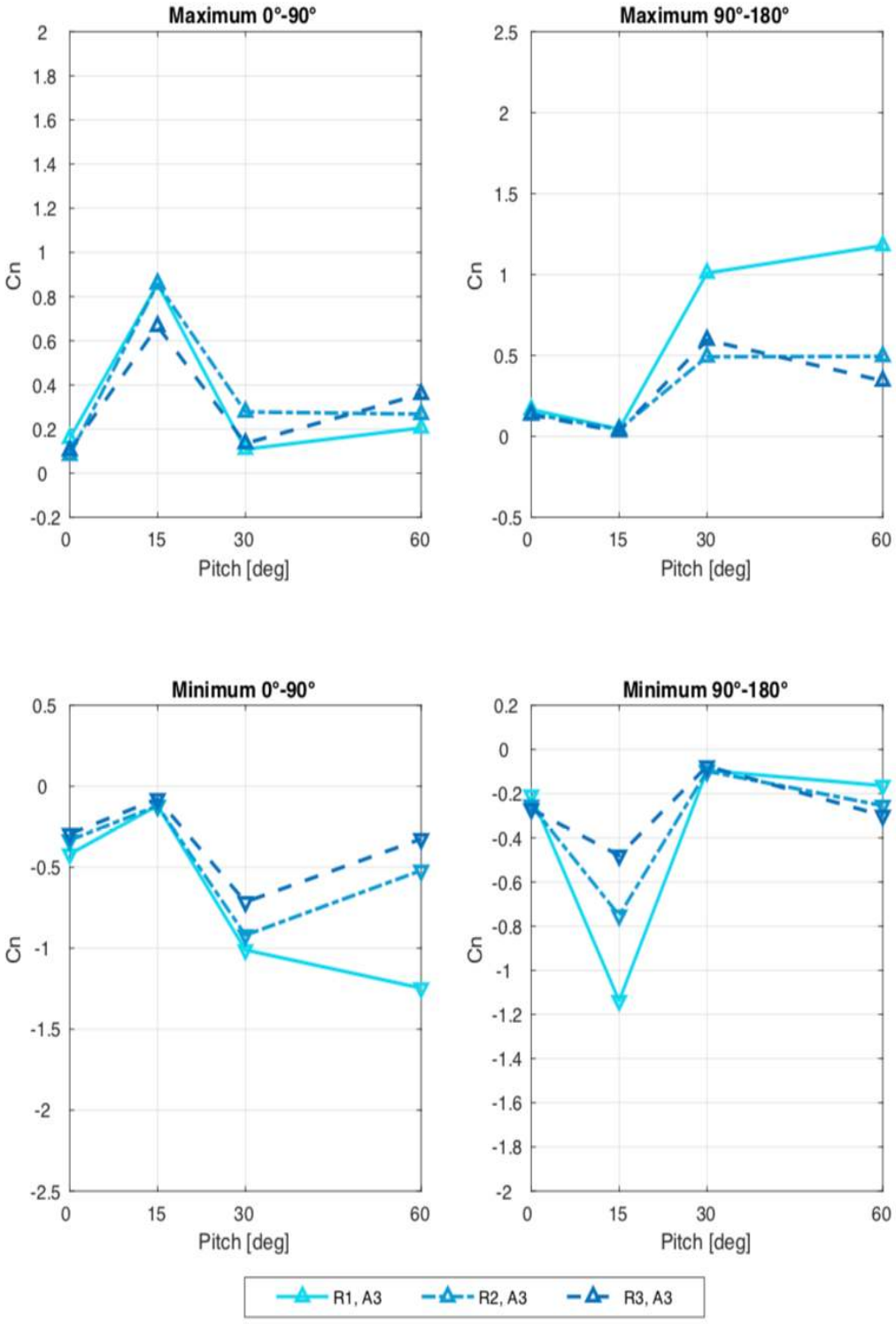

Figure 4.13 GCR 2.65 Zone A3 peak normal force coefficients for three instrumented rows

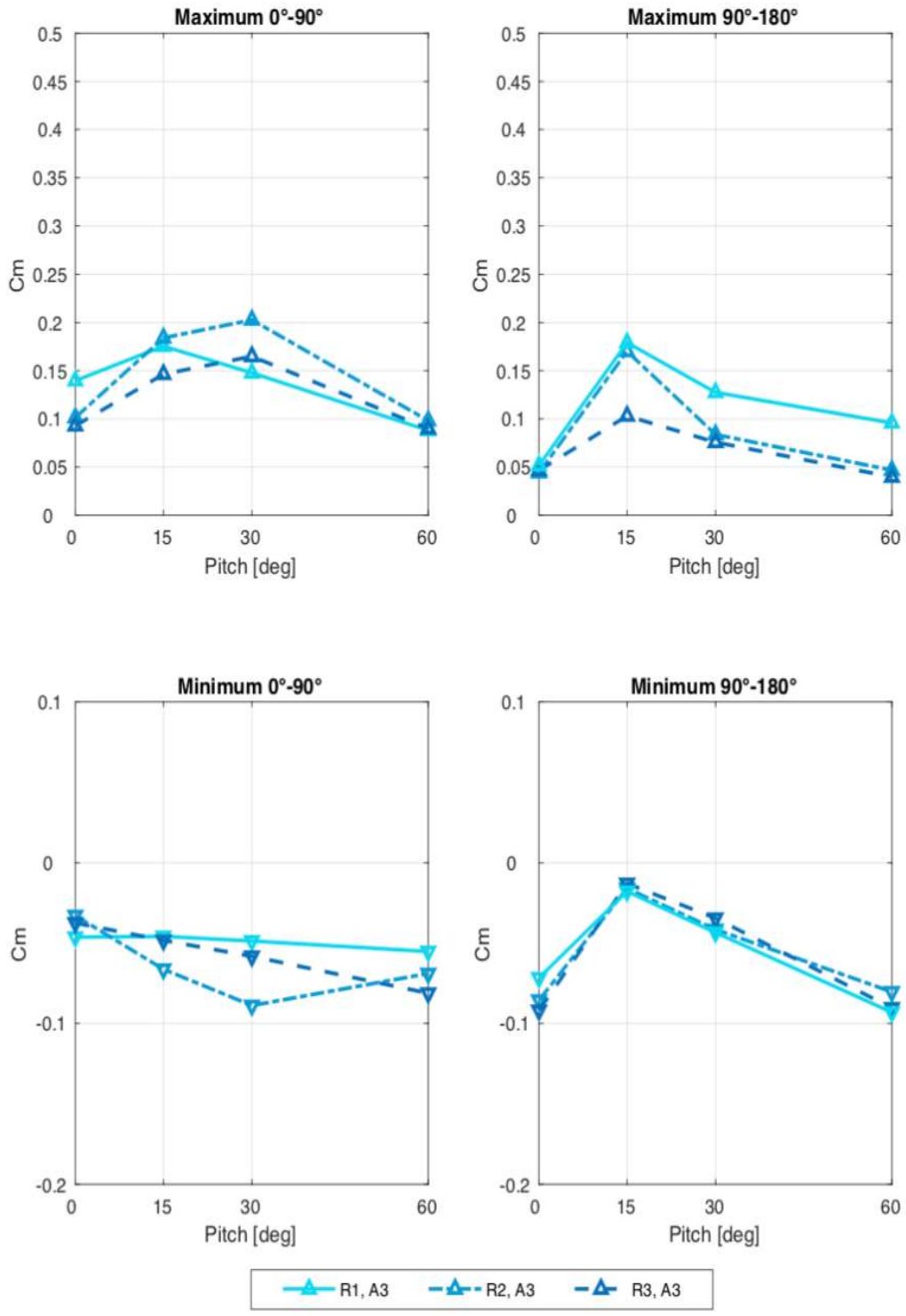

Figure 4.14 GCR 2.65 Zone A3 peak torque coefficients for three instrumented rows

4.2.1.2 GCR 4

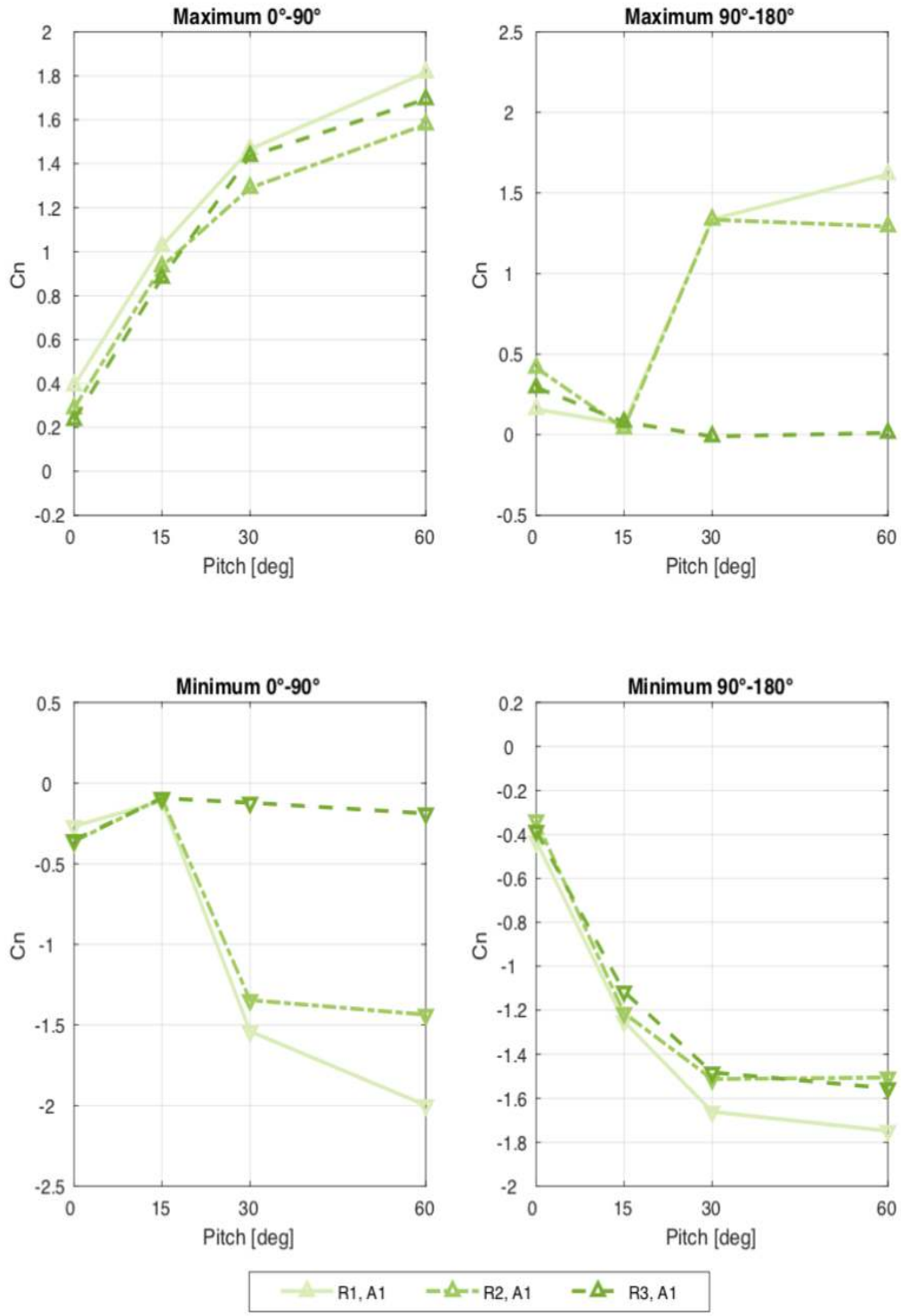

Figure 4.15 GCR 4 Zone A1 peak normal force coefficients for three instrumented rows

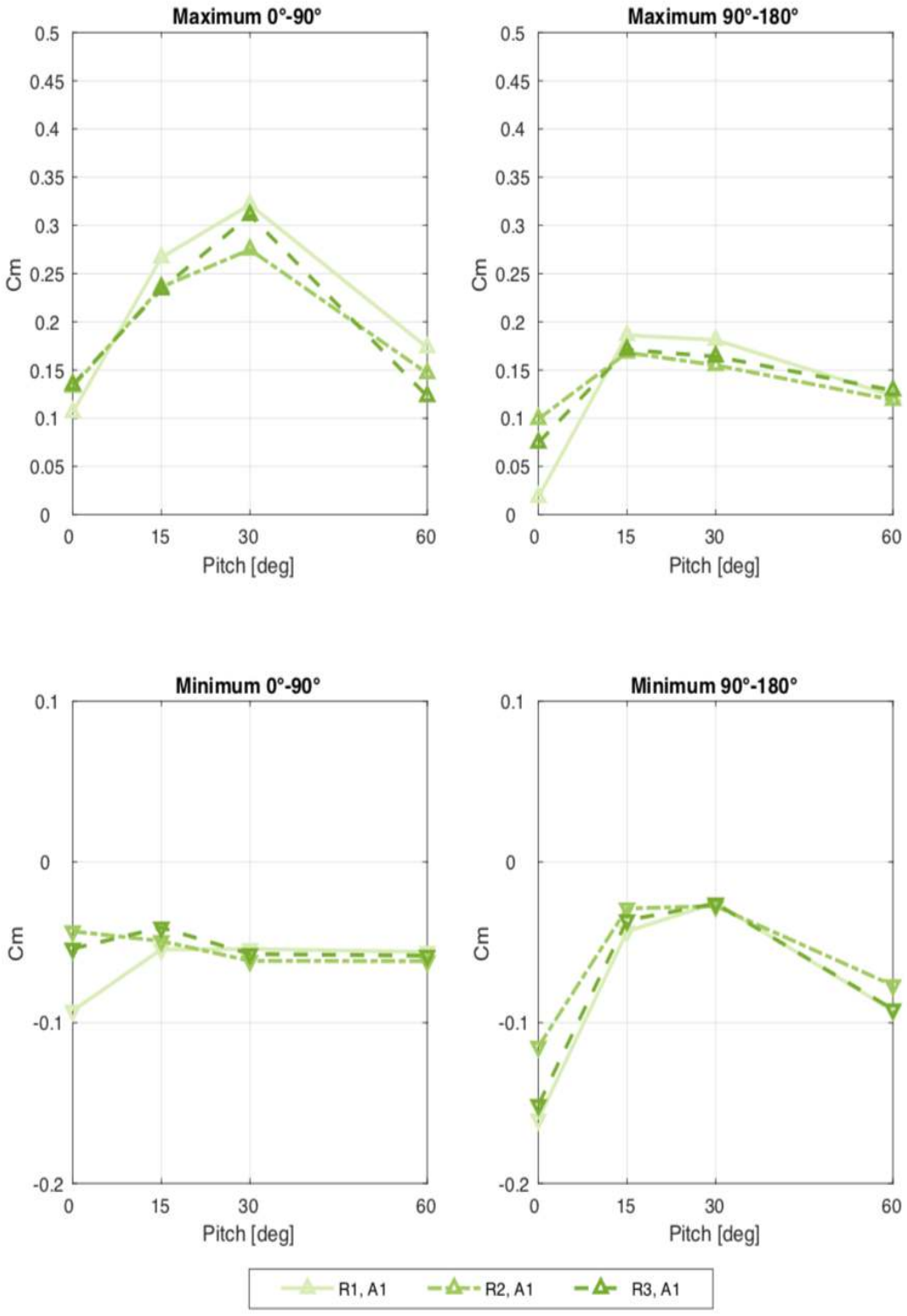

Figure 4.16 GCR 4 Zone A1 peak torque coefficients for three instrumented rows

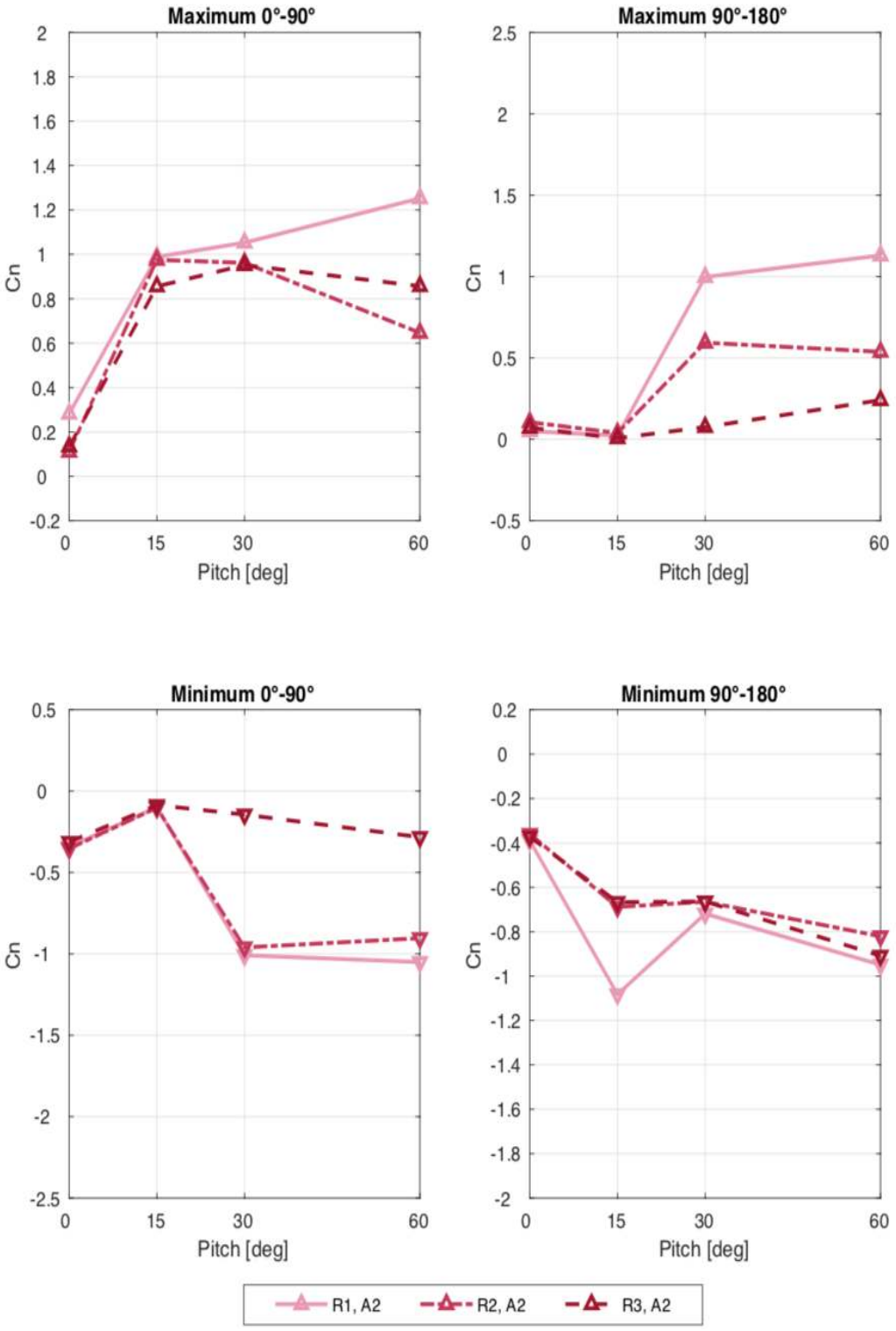

Figure 4.17 GCR 4 Zone A2 peak normal coefficients for three instrumented rows

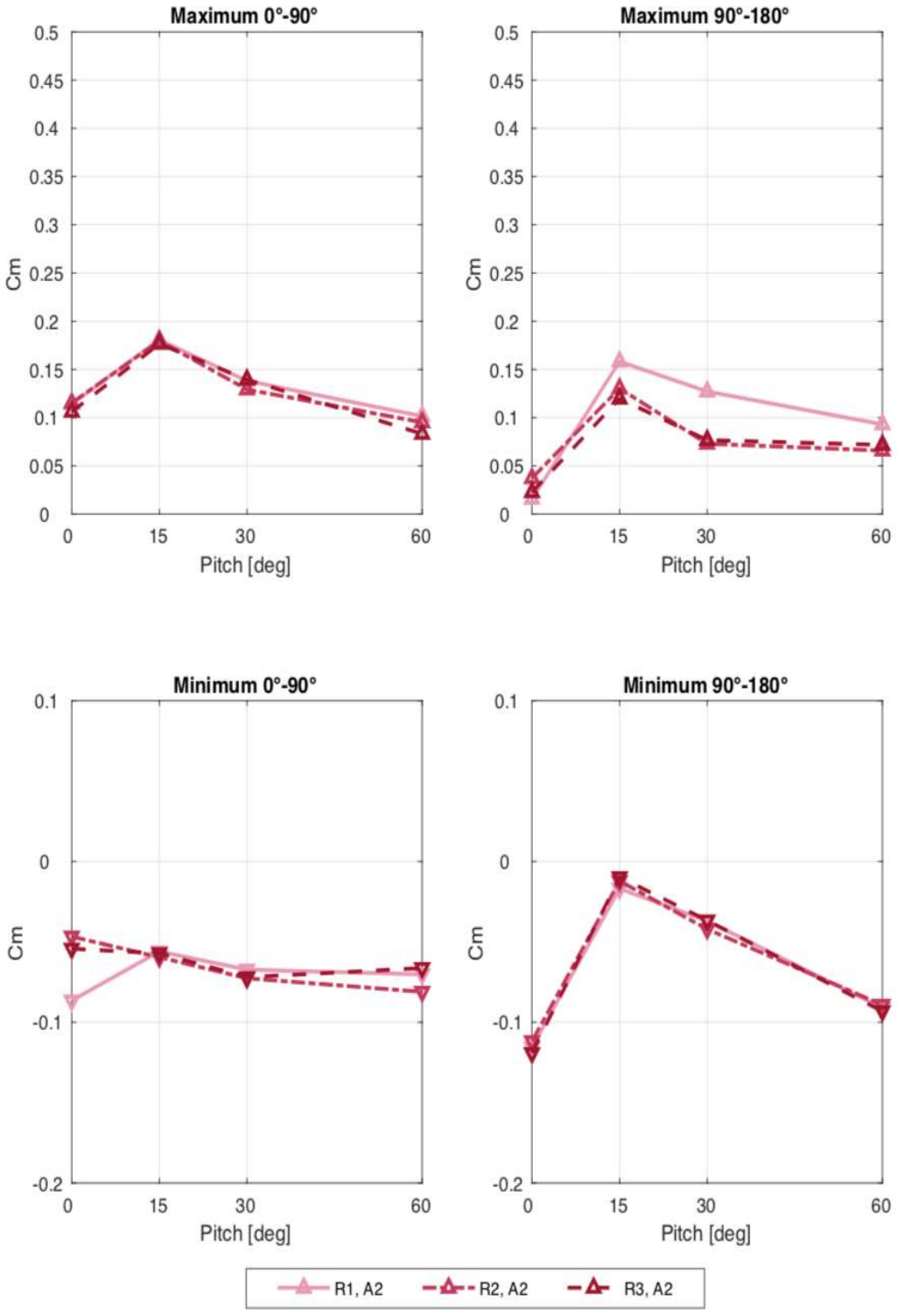

Figure 4.18 GCR 4 Zone A2 peak torque coefficients for three instrumented rows

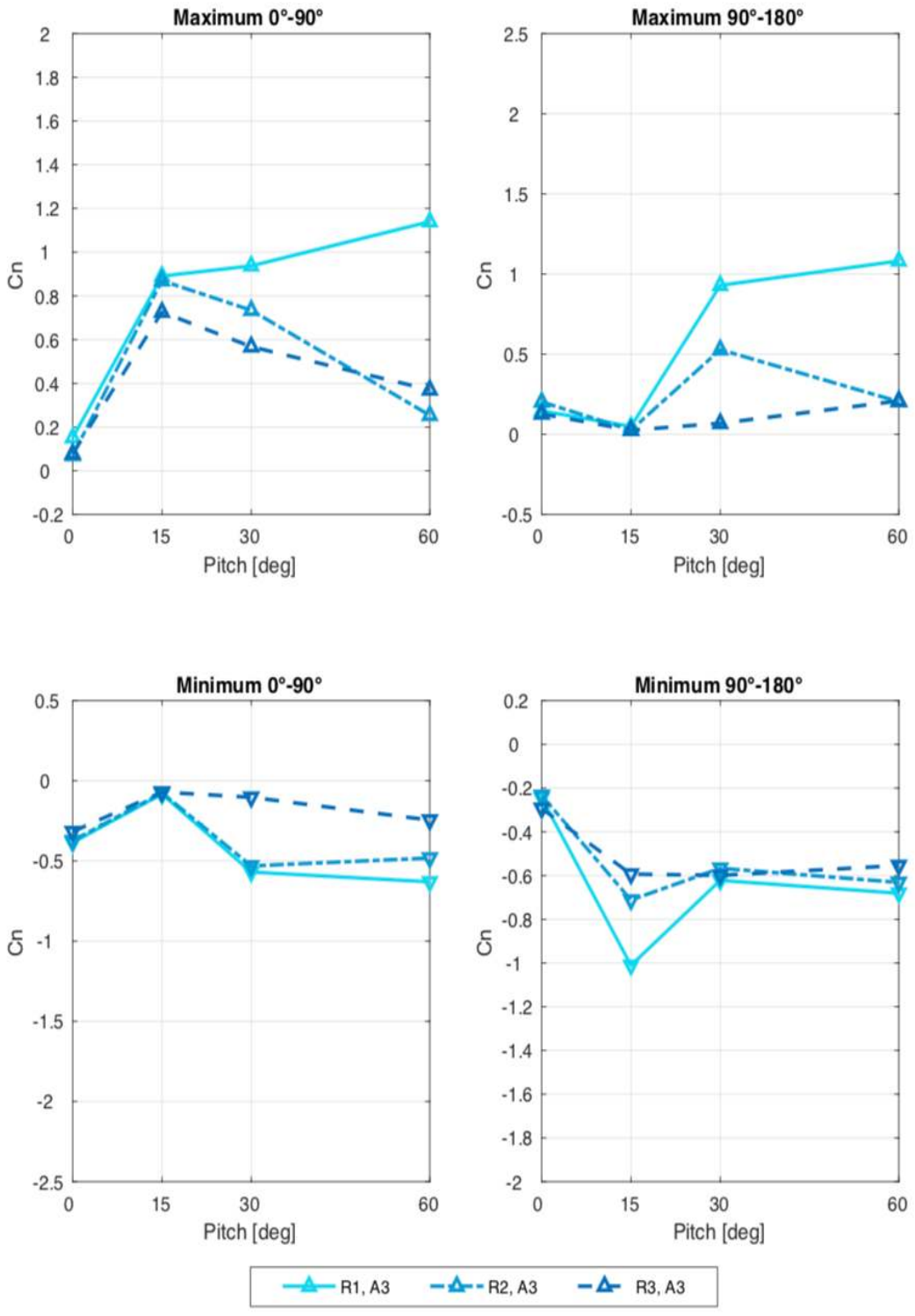

Figure 4.19 GCR 4 Zone A3 peak normal force coefficients for three instrumented rows

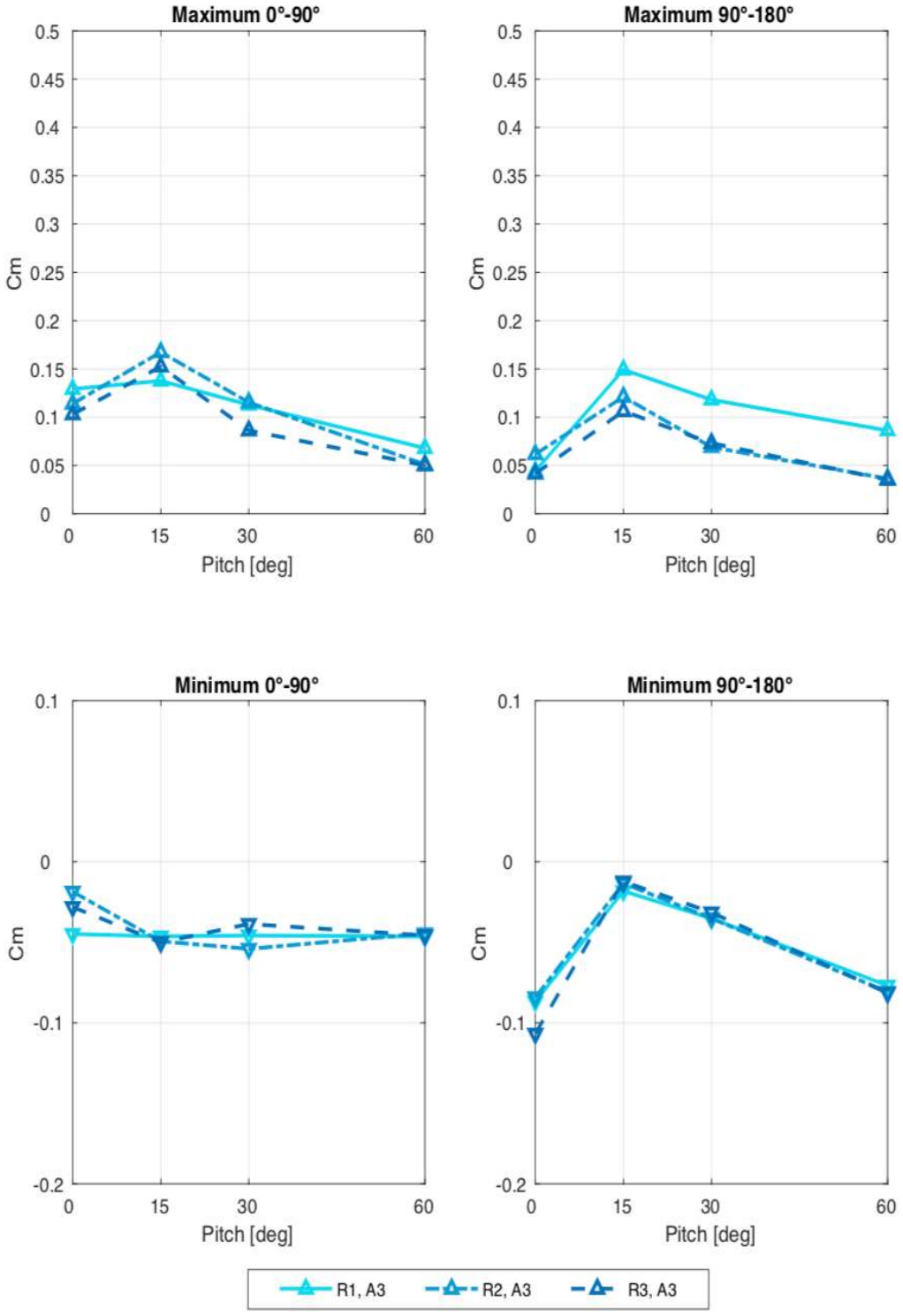

Figure 4.20 GCR 4 Zone A3 peak torque coefficients for three instrumented rows

4.2.2 Different Load Zones in Same Row

After row to row comparison graphs in previous section, zone comparisons for each row is presented to provide better understanding of peak loading variation with sectional position in each row. Graphs in following pages, present and compare the peak values of C_n and C_m measured from three different load zones that are located in the same row. Graphs are divided according to the same GCR categorization made in previous section.

By looking at direct zone to zone comparisons of peak C_n values, it is easier to spot A1, the most outer section, has the highest peak loading values. Although they have generally close values, we can say that A2, inner region of the outer column, reaches higher peak values than A3, the central column. The difference is clearer in GCR 4 graphs, especially for max 0°-90° and min 90°-180°. In min 0°-90° and max 90°-180° graphs, despite the different values, lines are showing the almost same trend according to pitch angle. Pitch angles of the extreme points are the same in every load zone if we compare the graphs with same orientation. Graphs presented in this section are especially important for comparing the first row of full array and the isolated first row arrangements due to having the same zone to zone arrangement in result graphs. As previously mentioned, there is a distinct difference between max 0°-90°, min 90°-180° graphs of R1 and the same ones from isolated first row test at 15° pitch. However, in peak C_m graphs this difference is not as distinct as the one for C_n, full array graphs seem slightly shifted downwards, if we compare them with the ones in single row test. The same magnitude ranking of load zones also holds in graphs of peak C_m. Graphs reach their peak points at 15° and 30° pitch, as experienced in the isolated first row test. During 0°-90° exposure, the highest peak C_m value recorded is at 30° pitch and during 90°-180° exposure, it is at 15° pitch for zone A1 in both of the GCR arrangements. Although during 90°-180° exposure, zones A2 and A3 have the highest loading values at the same pitch with zone A1, graphs of GCR 4 and the graph of R1 in GCR 2.65 reach their extremities at 15° pitch for zone A2 and A3 during 0°-90° exposure. These extreme points on graphs can be seen and compared more easily from the Eurocode type peak coefficient tables in next section.

With the below figures, all peak load coefficient graphs related to the test will be presented. In these last two sections, trends in these graphs are explained and critical locations are pointed out. Further discussion about peak load coefficients is carried out in the following section called peak load coefficient tables.

4.2.2.1 GCR 2.65

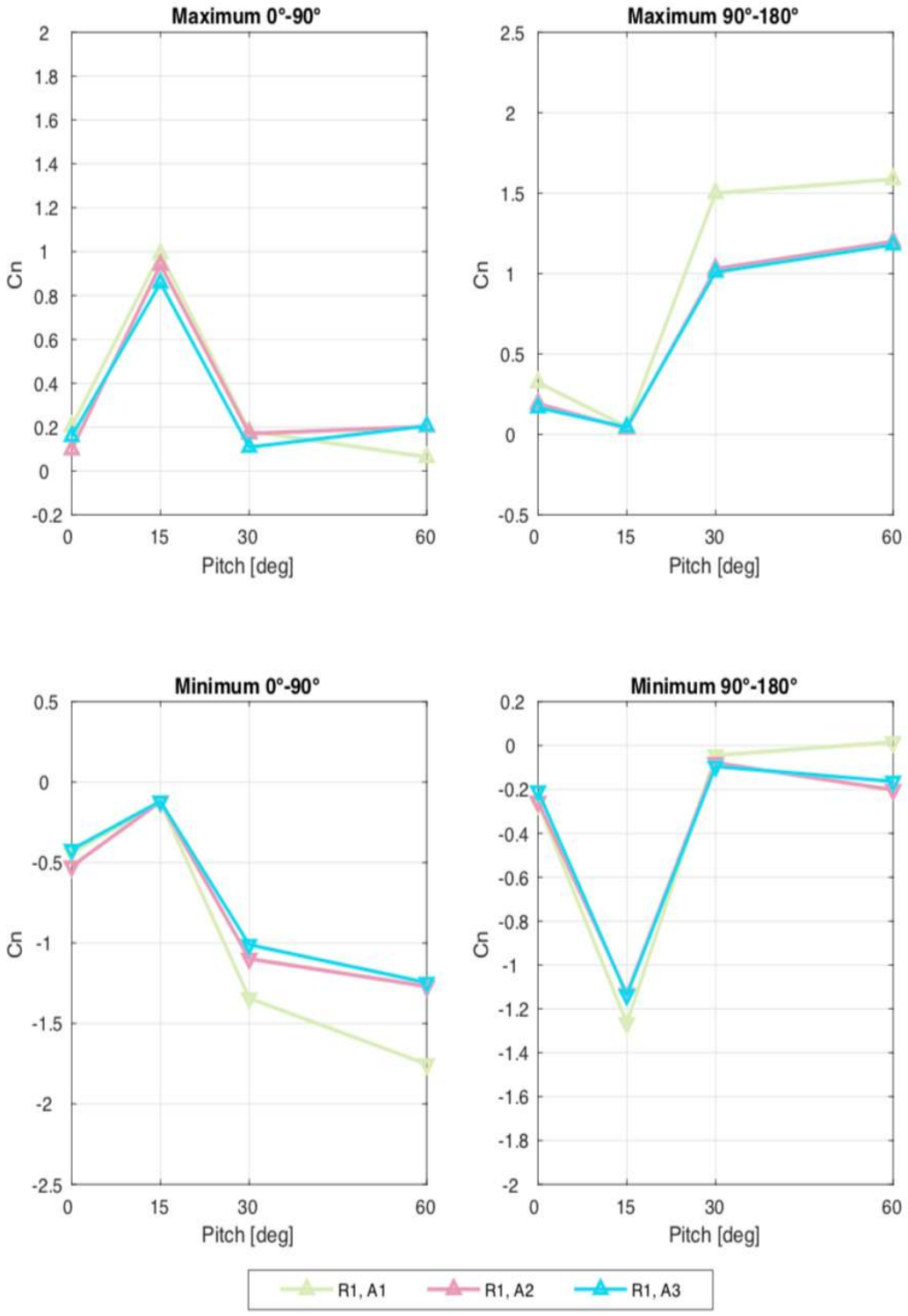

Figure 4.21 GCR 2.65 R1 peak normal force coefficients for three load zones

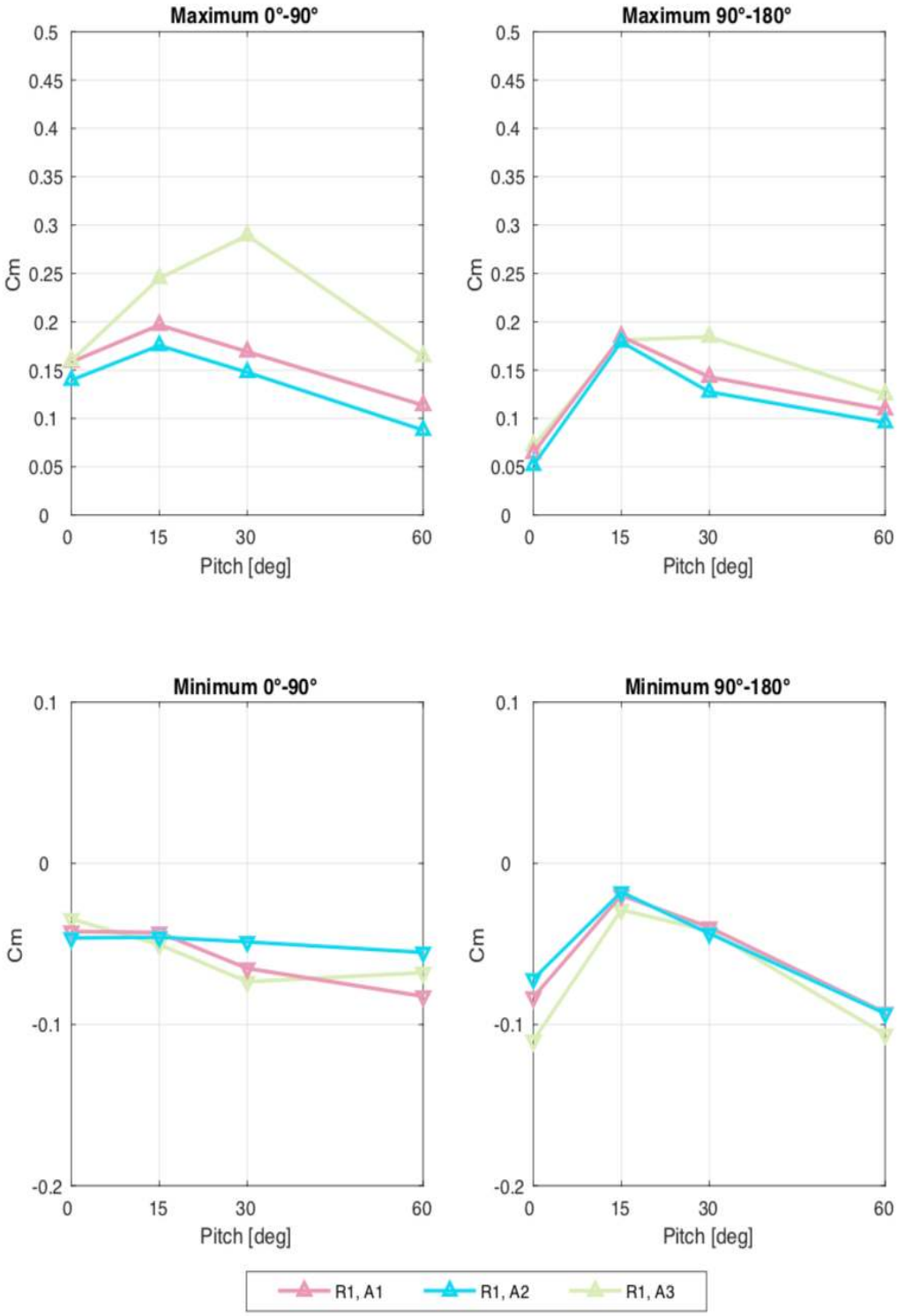

Figure 4.22 GCR 2.65 R1 peak torque coefficients for three load zones

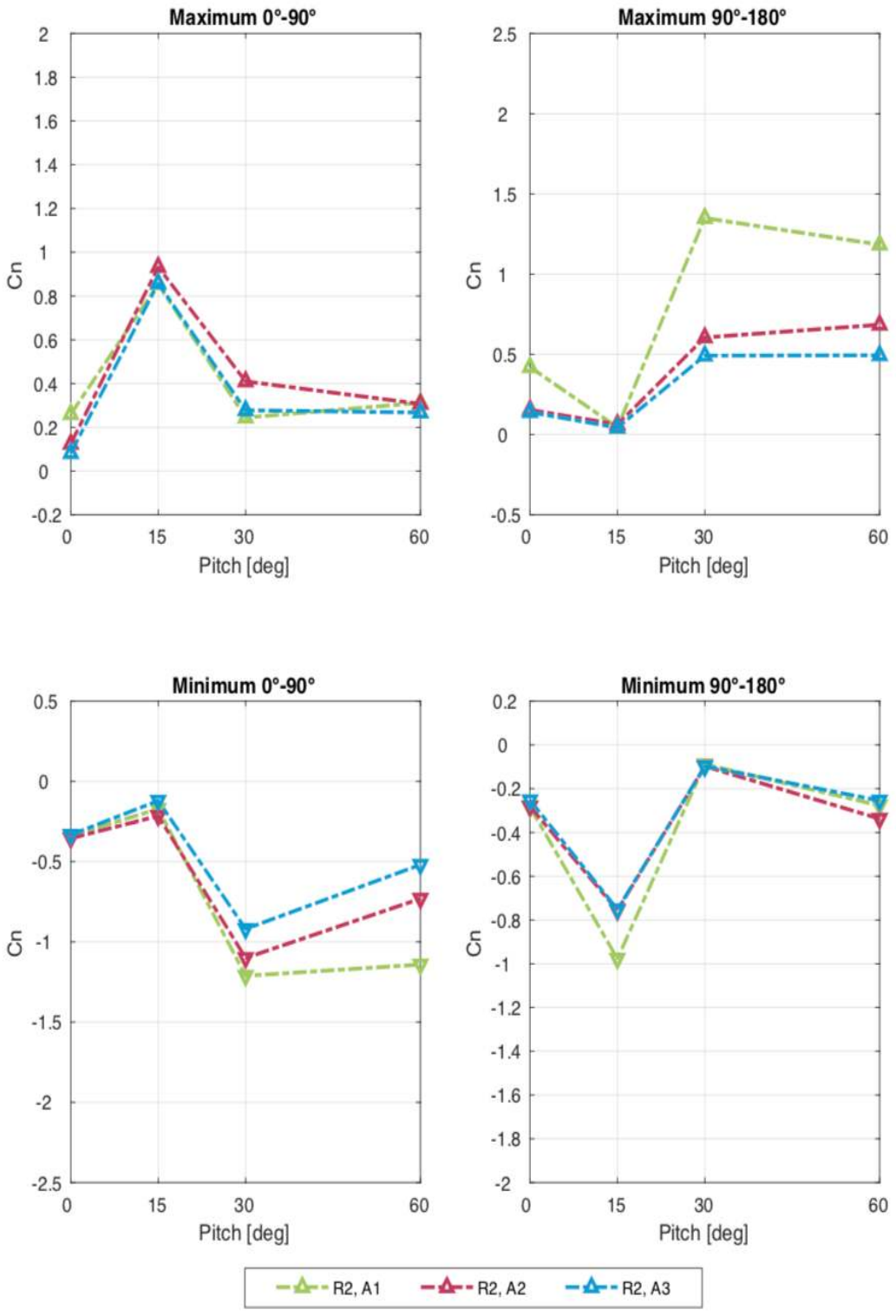

Figure 4.23 GCR 2.65 R2 peak normal force coefficients for three load zones

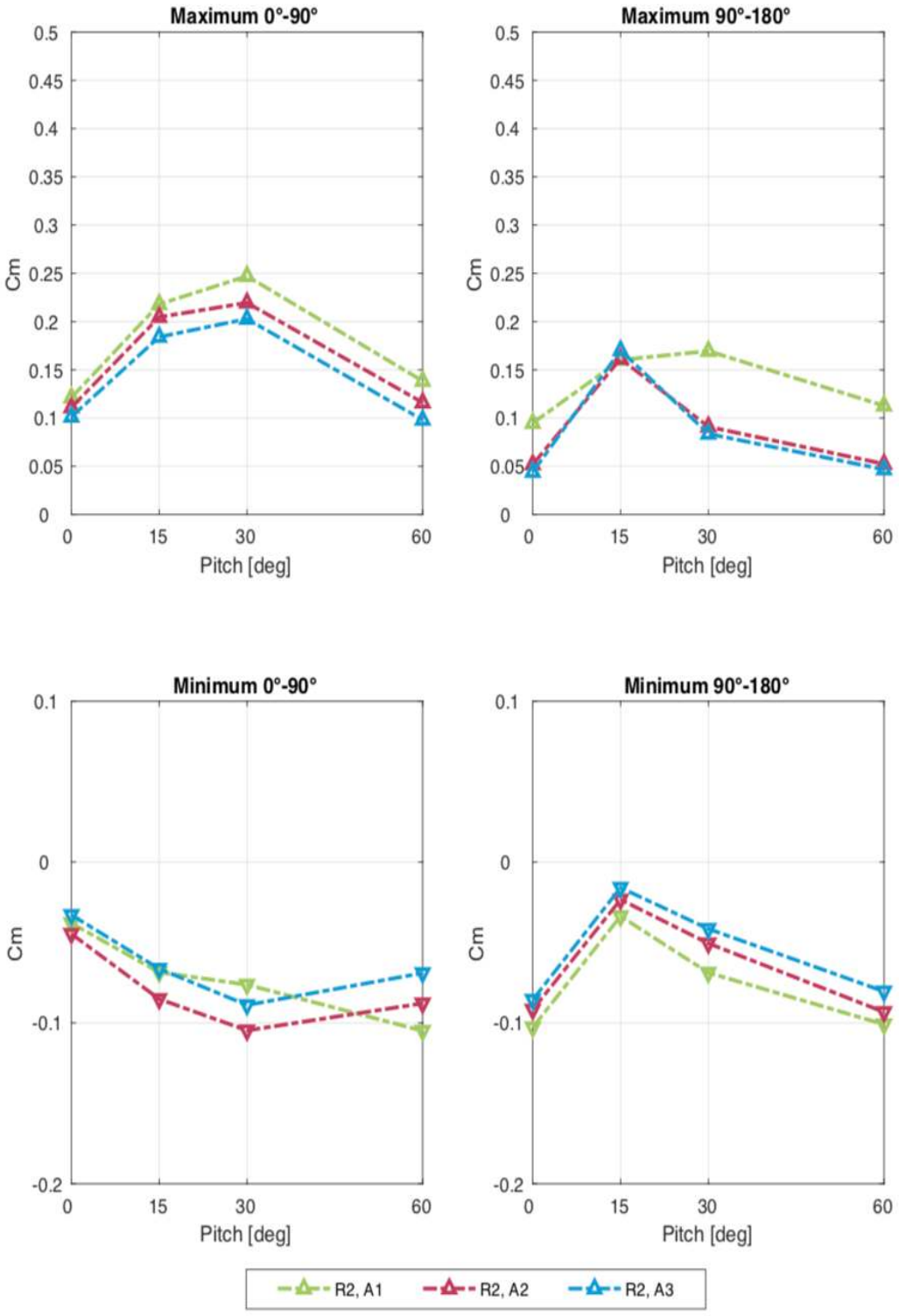

Figure 4.24 GCR 2.65 R2 peak torque coefficients for three load zones

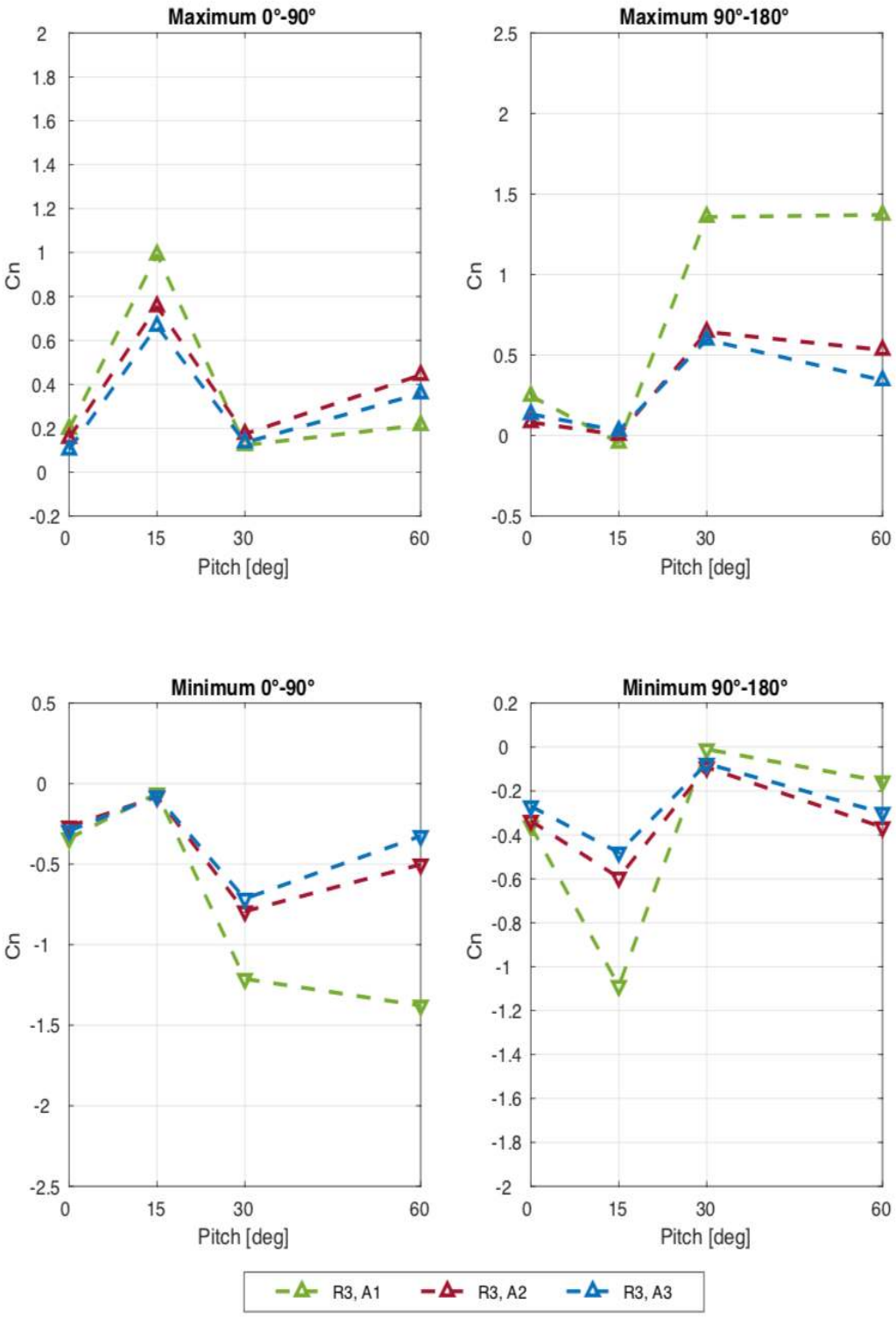

Figure 4.25 GCR 2.65 R3 peak normal force coefficients for three load zones

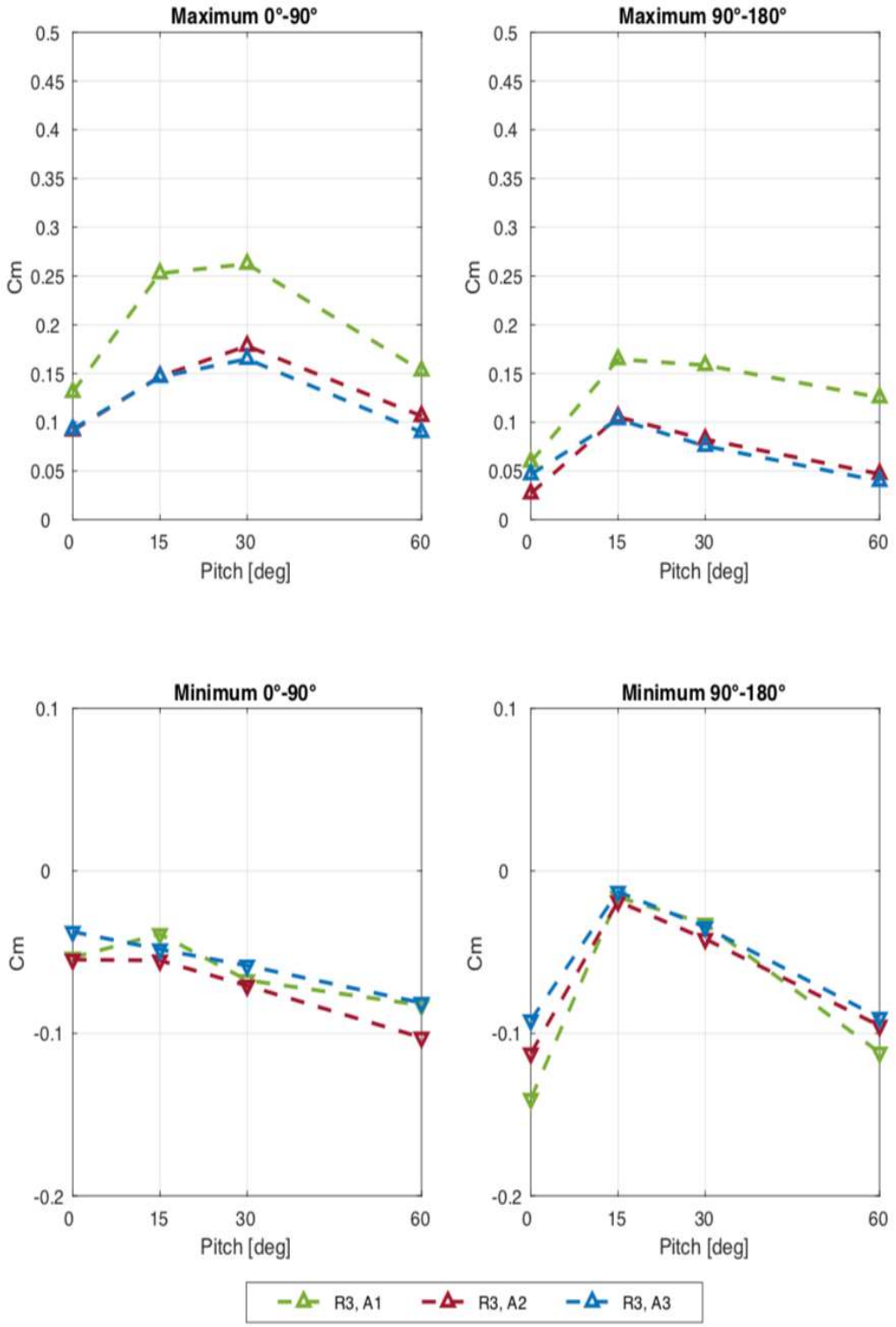

Figure 4.26 GCR 2.65 R3 peak torque coefficients for three load zones

4.2.2.2 GCR 4

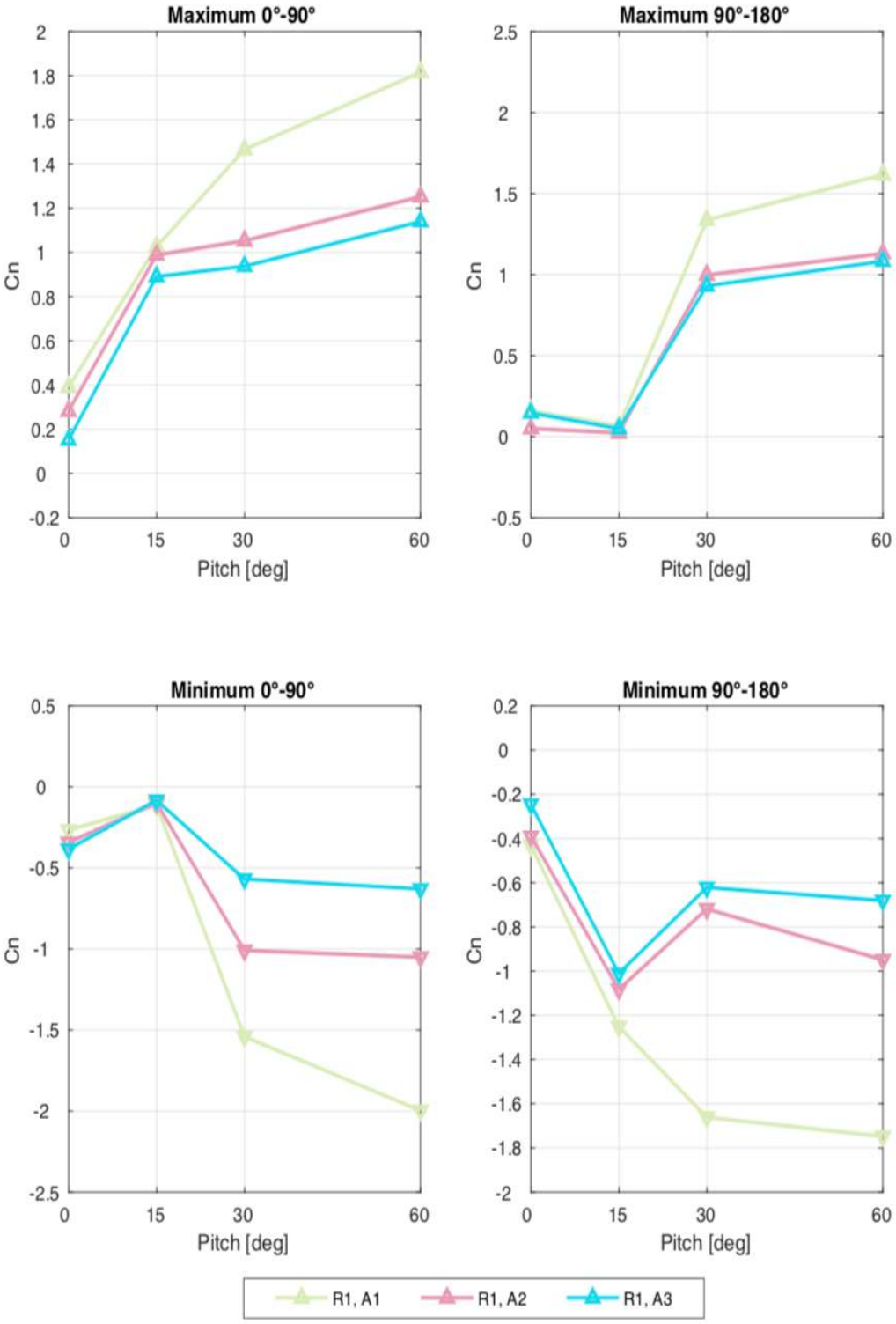

Figure 4.27 GCR 4 R1 peak normal force coefficients for three load zones

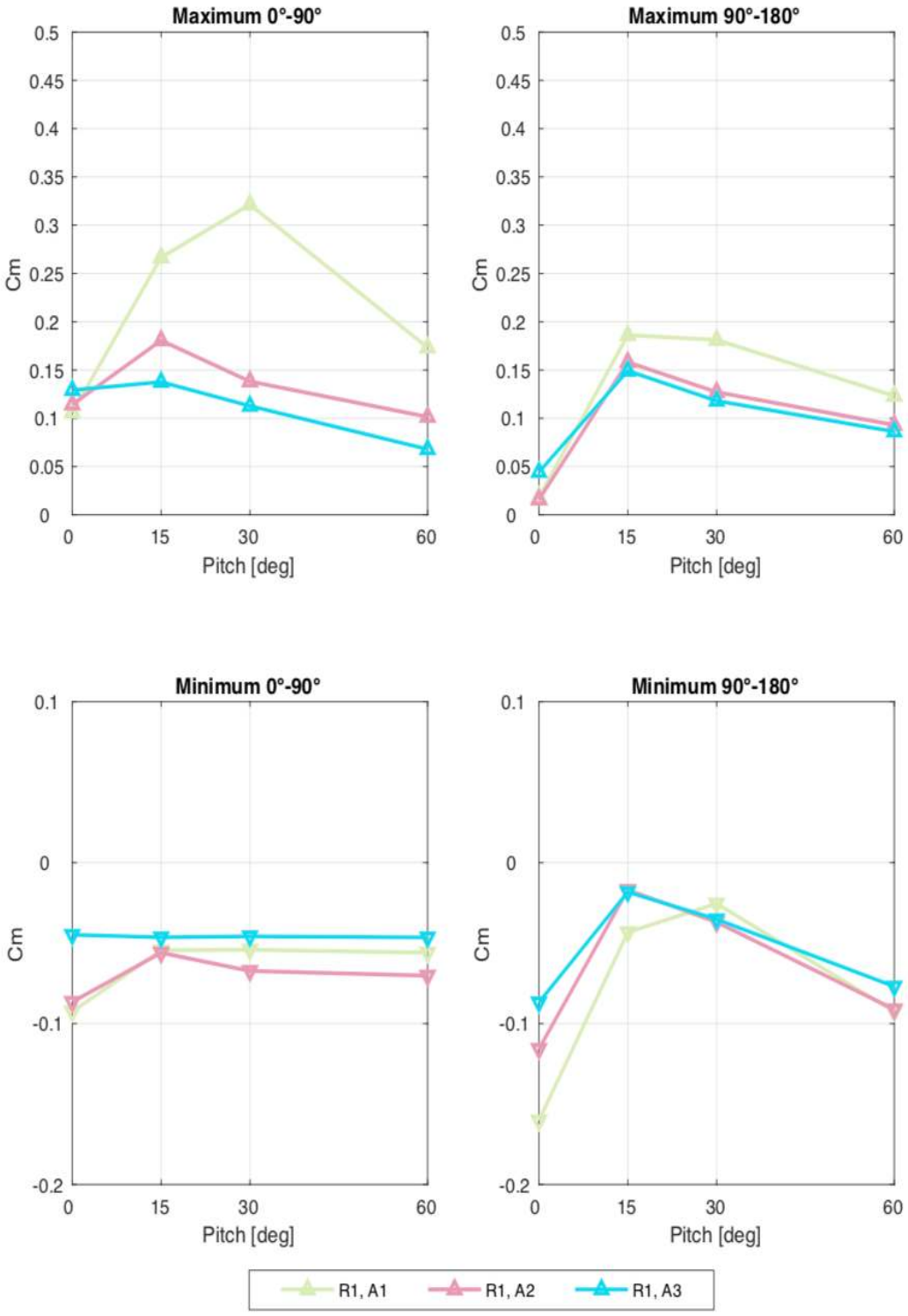

Figure 4.28 GCR 4 R1 peak torque coefficients for three load zones

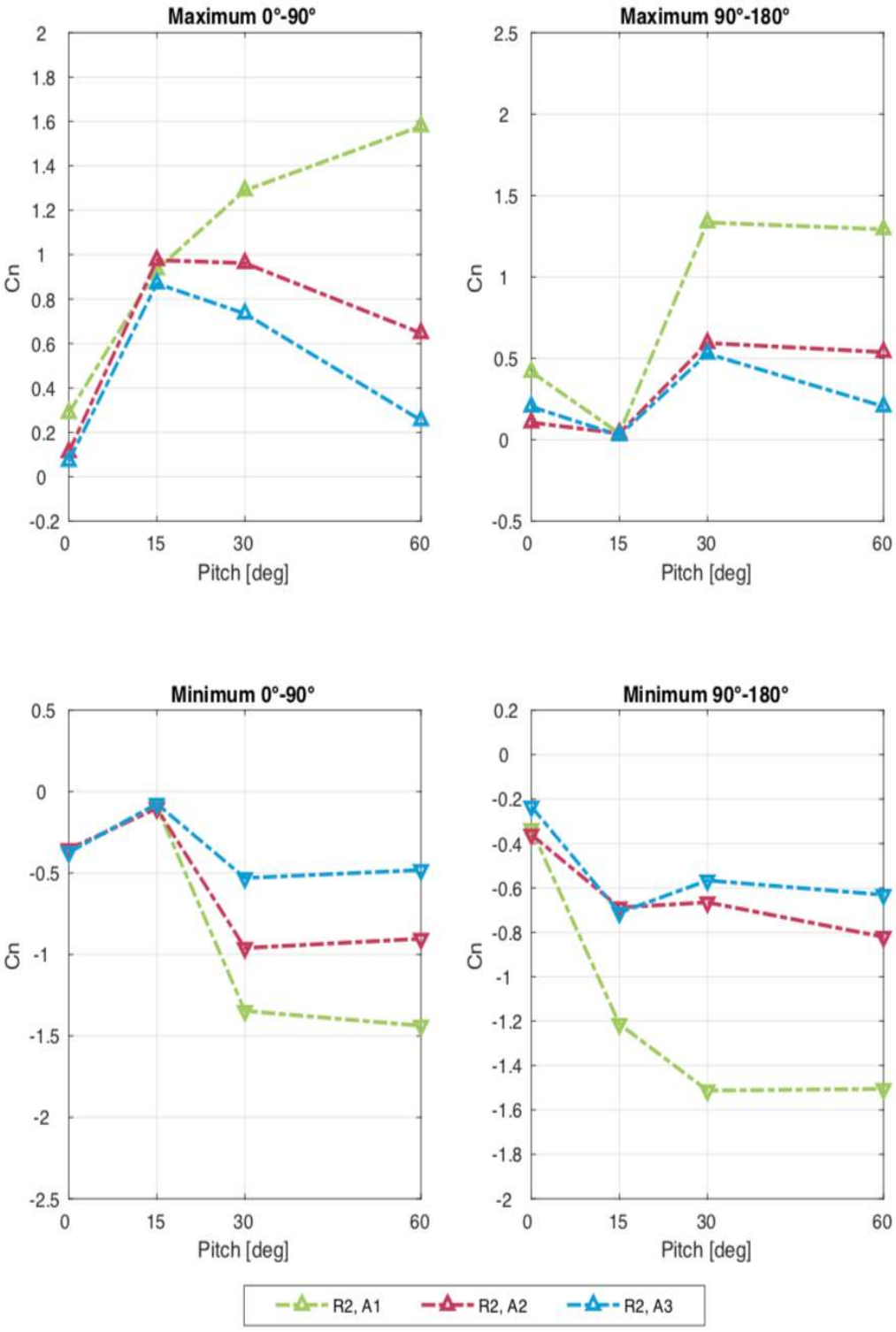

Figure 4.29 GCR 4 R2 peak normal force coefficients for three load zones

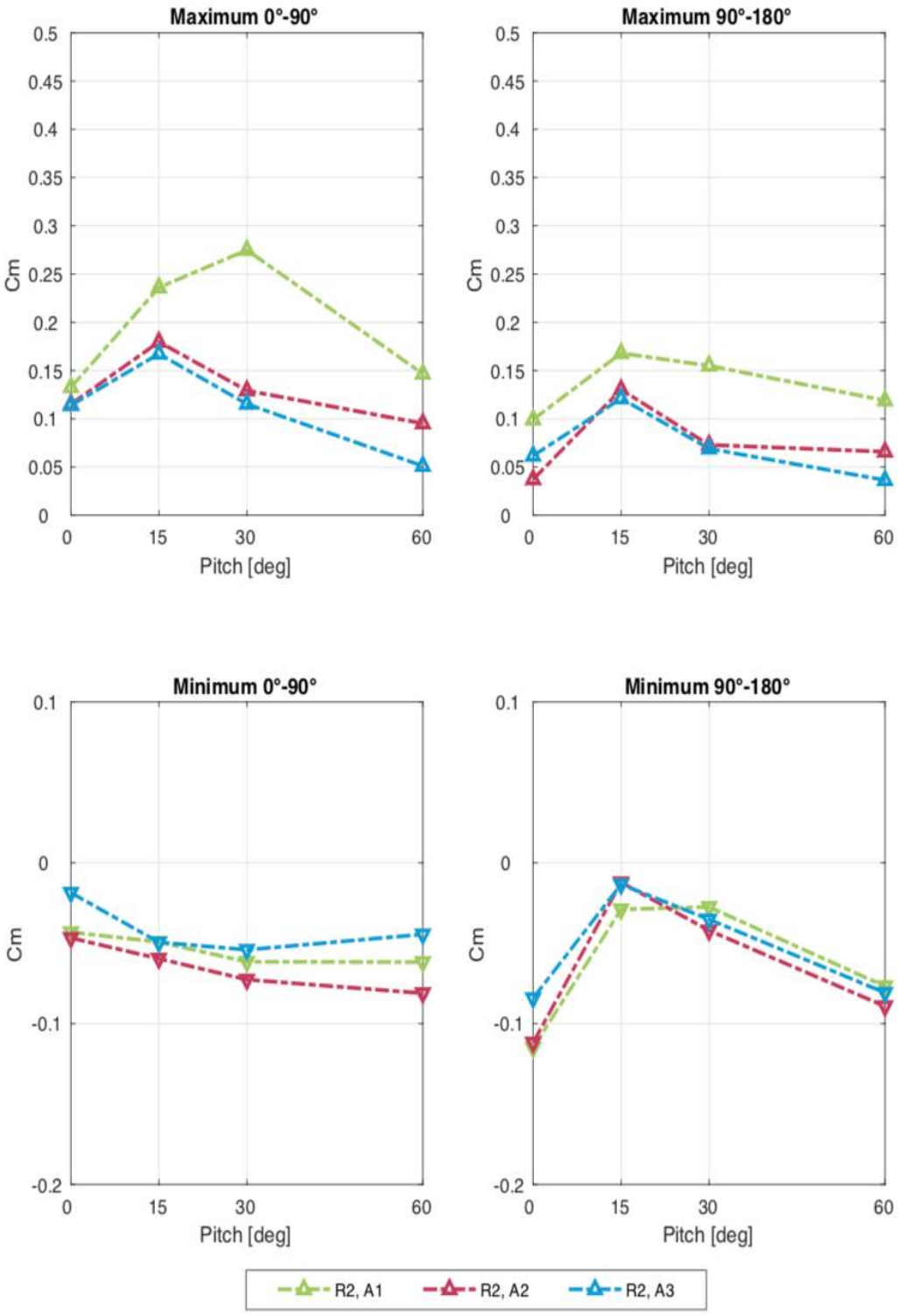

Figure 4.30 GCR 4 R2 peak torque coefficients for three load zones

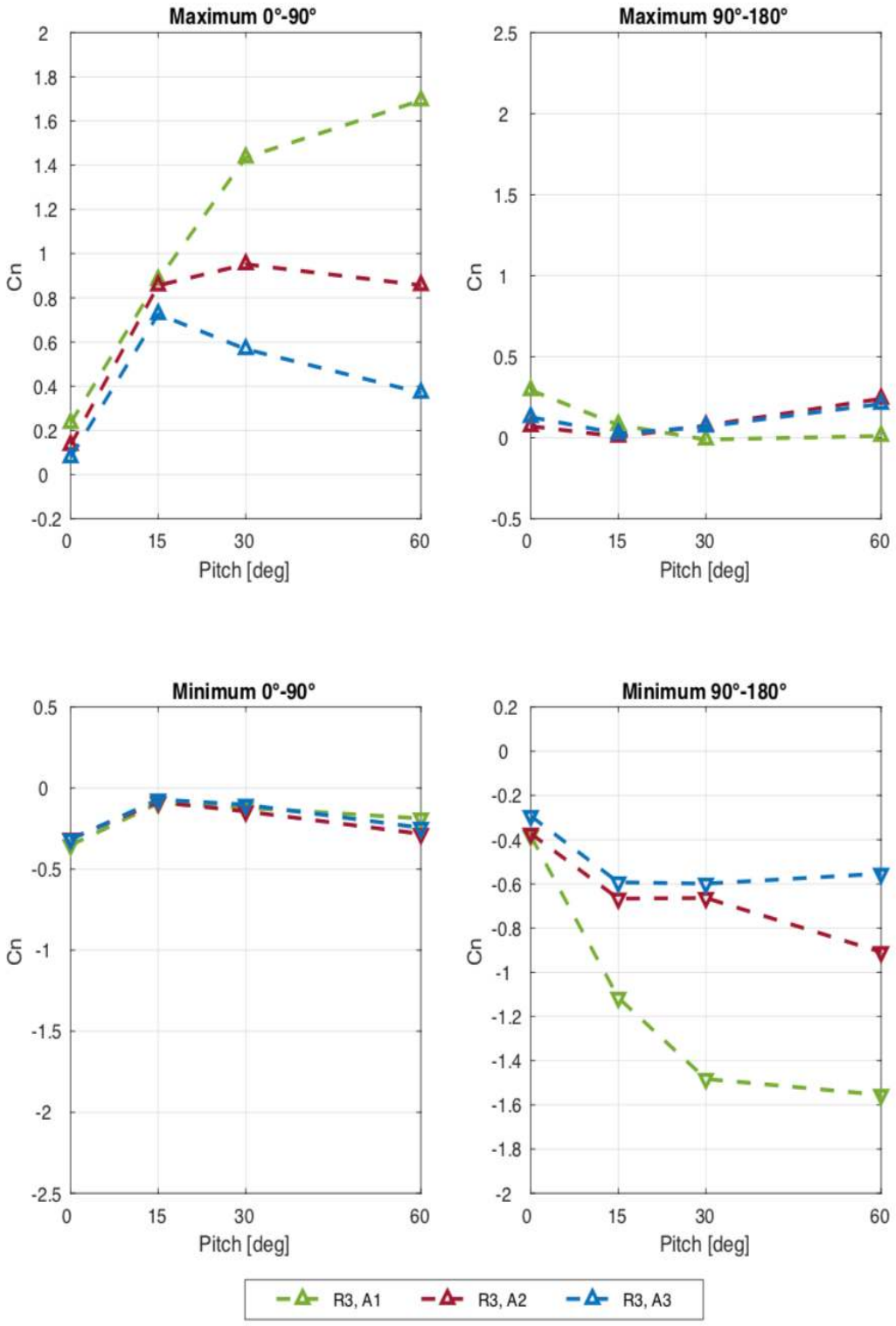

Figure 4.31 GCR 4 R3 peak normal force coefficients for three load zones

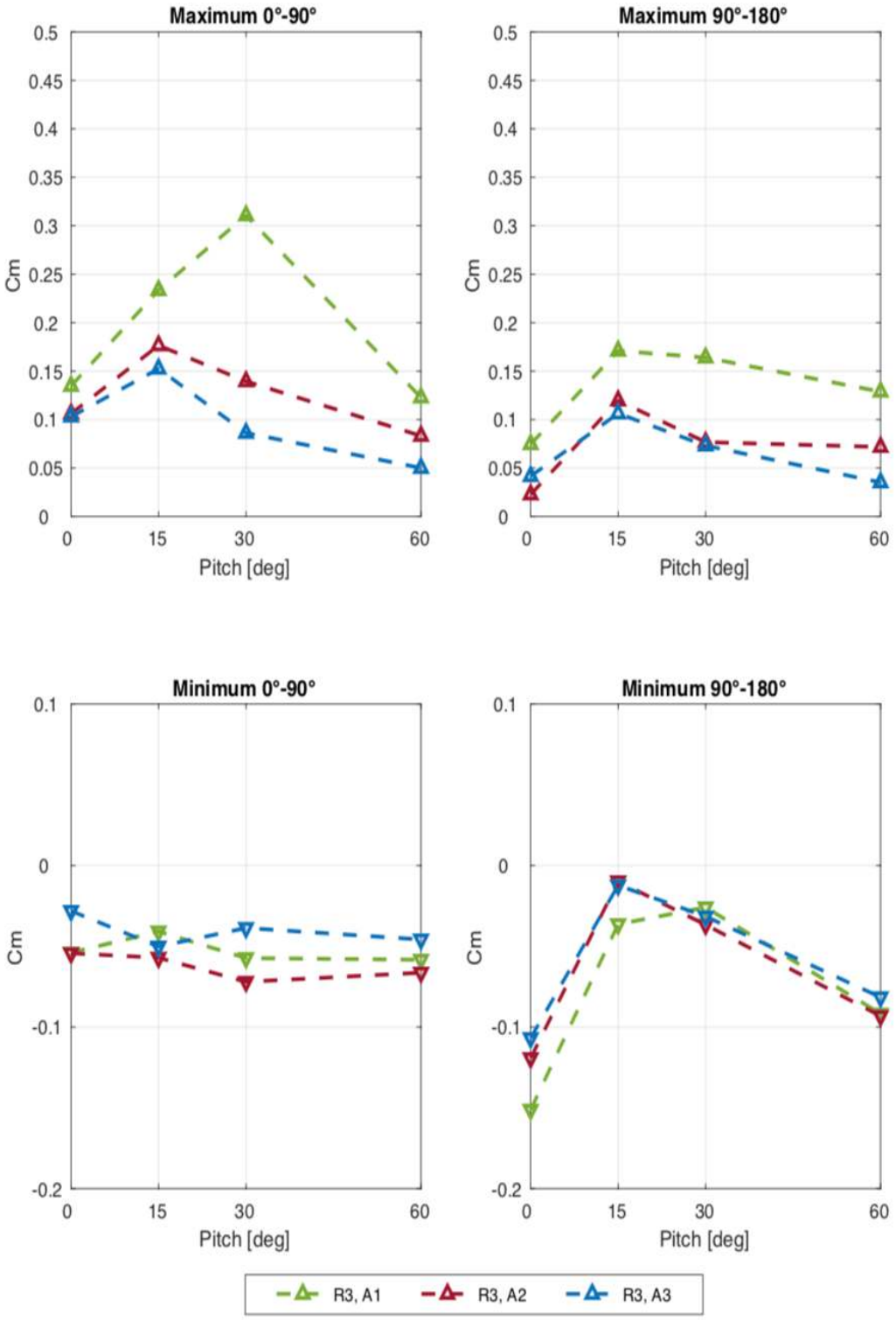

Figure 4.32 GCR 4 R3 peak torque coefficients for three load zones

4.2.3 Peak Load Coefficient Tables

Extremities for each pitch angle in above graphs are tabulated according to zone and row numbers. To clarify the most critically loaded sections, extreme points are chosen under the consideration of 1 full rotation of the turntable, full range of 0°-180° wind exposure. So, two ranges of wind exposure presented in graphs are merged into one full range peak coefficient envelope to point out the highest peak coefficient values. One more important alteration that should be mentioned is the reduction made in zone numbers. With considering the small peak values presented in zone A3 and its mostly similar behaviors with zones A2, zoning to investigate highest peak values done with using 2 zones. New load zones are described in figure 4.33, separation made between zones A2 and A3 is removed while row dividing is still the same. A1 represents the most outer columns and A2 is the new central position created with merging the data measured from previous load zones A2 and A3.

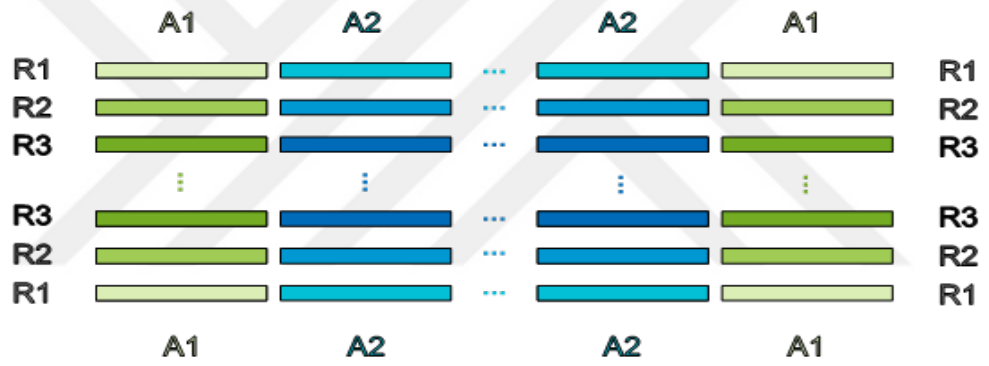

Figure 4.33 Zoning for peak coefficient tables

The absolute global peak value in each column is highlighted with red. These highlighted numbers are showing the maximum value of the load coefficient experienced by each dedicated section at specific pitch angle and GCR arrangement. Therefore, data in these tables are useful to understand which sections require special interest at particular operation conditions. The global values are chosen by comparing 10 significant figure measurements obtained from graphs but, due to ease in representation, these values are rounded to the closest 2-digit values inside the table. 0 inside the cells is representing the values smaller than 0.05.

There are couple of important comments needed to be made from the following tables. We already know from graphs that, normal force coefficient peaks at higher pitch angles while torque coefficient is peaking at middle pitch angles. It is easier to see this behavior with few exemptions. In GCR 4, it seems like global peak value of C_n is reached at 15° for central zones in second and third row but

these values are particularly small if we compare them with A1 values. It should also be noted, global peak C_n for GCR 2.65 is generally in negative direction while it is pointing positive direction for GCR 4. However, most of the time, the difference between global positive peak and negative peak is not more than 0,3 for each column. Global peaks of C_m is showing straighter pattern than C_n and it always peaks for positive torque values. For A1, torque coefficient always peaks at 30°. For A2, the global peak is at 15° in GCR 4 and at 30° in GCR 2.65. However, the differences between the global peaks measured at 15° and 30° is as small as 0,02 in GCR 2.65, so attention should also be paid to the operations at 15°.

These tables are the last set of results that will be presented. The tables are again categorized according to GCR and showing the most critical sections and operating conditions. In the next discussion section, further comments related to these results will be introduced.

4.2.3.1 GCR 2.65

	Cn GCR 2.65		ROW NUMBER					
			R1		R2		R3	
			A1	A2	A1	A2	A1	A2
Pitch Angle	0°	Max	0,3	0,2	0,4	0,1	0,2	0,1
		Min	-0,5	-0,4	-0,4	-0,3	-0,4	-0,3
	15°	Max	1,0	0,9	0,9	0,9	1,0	0,7
		Min	-1,3	-1,1	-1,0	-0,8	-1,1	-0,5
	30°	Max	1,5	1,0	1,3	0,5	1,4	0,6
		Min	-1,3	-1,0	-1,2	-0,9	-1,2	-0,7
	60°	Max	1,6	1,2	1,2	0,5	1,4	0,4
		Min	-1,8	-1,2	-1,1	-0,5	-1,4	-0,3

Table 4.1 Peak normal force coefficients during 0°-180° wind exposure

	Cm GCR 2.65		ROW NUMBER					
			R1		R2		R3	
			A1	A2	A1	A2	A1	A2
Pitch Angle	0°	Max	0,2	0,1	0,1	0,1	0,1	0,1
		Min	-0,1	-0,1	-0,1	-0,1	-0,1	-0,1
	15°	Max	0,2	0,2	0,2	0,2	0,3	0,1
		Min	-0,1	0,0	-0,1	-0,1	-0,1	-0,1
	30°	Max	0,3	0,1	0,2	0,2	0,3	0,2
		Min	-0,1	0,0	-0,1	-0,1	-0,1	-0,1
	60°	Max	0,2	0,1	0,1	0,1	0,2	0,1
		Min	-0,1	-0,1	-0,1	-0,1	-0,1	-0,1

Table 4.2 Peak torque coefficients during 0°-180° wind exposure

4.2.3.2 GCR 4

	Cn GCR 4		ROW NUMBER					
			R1		R2		R3	
			A1	A2	A1	A2	A1	A2
Pitch Angle	0°	Max	0,4	0,2	0,4	0,2	0,3	0,1
		Min	-0,4	-0,4	-0,4	-0,4	-0,4	-0,3
	15°	Max	1,0	0,9	1,0	0,9	0,9	0,7
		Min	-1,3	-1,0	-1,2	-0,7	-1,1	-0,6
	30°	Max	1,5	0,9	1,3	0,7	1,4	0,6
		Min	-1,7	-0,6	-1,5	-0,6	-1,5	-0,6
	60°	Max	1,8	1,1	1,6	0,3	1,7	0,4
		Min	-2,0	-0,7	-1,5	-0,6	-1,6	-0,6

Table 4.3 Peak normal force coefficients during 0°-180° wind exposure

	Cm GCR 4		ROW NUMBER					
			R1		R2		R3	
			A1	A2	A1	A2	A1	A2
Pitch Angle	0°	Max	0,1	0,1	0,1	0,1	0,1	0,1
		Min	-0,2	-0,1	-0,1	-0,1	-0,2	-0,1
	15°	Max	0,3	0,1	0,2	0,2	0,2	0,2
		Min	-0,1	0,0	-0,1	0,0	-0,1	-0,1
	30°	Max	0,3	0,1	0,3	0,1	0,3	0,1
		Min	-0,1	-0,1	-0,1	0,0	-0,1	-0,1
	60°	Max	0,2	0,1	0,1	0,1	0,1	0,1
		Min	-0,1	-0,1	-0,1	-0,1	-0,1	-0,1

Table 4.4 Peak torque coefficients during 0°-180° wind exposure

4.3 Discussion

In this section above results are evaluated according to panel inclination, row spacing and wind exposure angle. Inside the following subtitles, relevance of the test results to the concepts introduced in chapter 2 are investigated by considering the test variables. After this section, chapter 4 will be concluded, and the final conclusion chapter will start. Discussions inside the next pages are made with considering the comments from similar wind studies, for interested readers, these documents can be found inside references.

4.3.1 Effect of Panel Pitch Angle

It is clear to see the increase in aerodynamic loading on the trackers with the pitch angle. As already mentioned, this result is not a surprise if we consider the change in effective loading area with the pitch. On the other hand, increasing pitch angle has an opposite effect on the moment arm length, this is the reason of small C_m values inside above tables at 60° pitch. Another important aspect of the pitch angle is sheltering effect of the first row on the following rows in the array.

Sheltering effect is the blockage of the first row applied on to the inner rows and it can be seen in the graphs presented in section 4.2.1. If we investigate the behavior between 30° and 60°, we will see that C_n increases from 30° to 60° for R1 but it decreases for R2 and R3 despite the increase in their effective loading area. The reason of this behavior is that increase in the effective area of the first row, also means increase in the area causing the blockage and decreases the direct wind effect on the inner rows. Due to being related to direct wind effect, this behavior can be better investigated from envelopes of max 90°-180° and min 0°-90° where direct wind effects are dominant.

4.3.2 Effect of Wind Exposure Angle

As described in chapter 3, test was held on the turntable of the test section to measure load coefficients for different wind exposures. As expected, the load coefficients that are recorded at the exposure angles which makes panel orientation perpendicular to incoming wind direction have higher value than the load recorded at skewed winds. This is because the direct wind loading that is causing the normal force on the trackers also becomes skewed unlike 0° and 180° exposures. To see this behavior on the test data, figure 4.34 can be investigated.

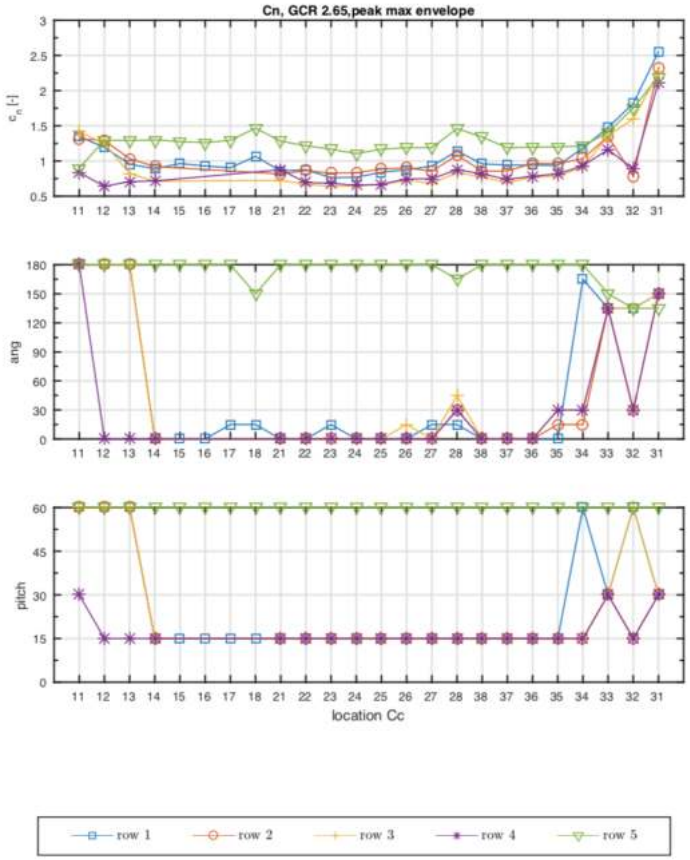

Figure 4.34 Local maximum peak normal force coefficients, GCR 2.65

The graph is showing the peak positive loading values for each chord inside the different rows with indicating the pitch and exposure angles at the point where the peak values are measured. As seen in above figure, data from 5 rows are presented rather than 3 rows presentation that is used inside the graphs of previous sections. This is accomplished by rotating the turntable with arranging the panel tilt to the negative or positive angles. For negative pitch and 0° exposure angle, the first instrumented row also is the first row of the full model array. On the other hand, positive pitch angle and 180° rotation of the turn table put the first instrumented row to the fifth row which is the last downstream row of the array. This is also true for the second instrumented row which is located in the second row for negative pitch angles and the fourth row for the positive pitch angles. With knowing this angular arrangement, it can be better understood why 5th row is experiencing positive peak at 180° and 1st row at 0°. Even if this statement is holds for most of the central chords, it cannot be said for the most outer chords in each column. Chords that have 7-8 or 1-2 as a second digit are representing the most outer sections and the chord alignment in each row is in same order with the placement in 'location Cc' axis. If we look at these outer sections, we will see that, slightly skewed winds create higher peak loads. It is because of the vibration induced by the slightly skewed winds on these outer sections. This vibration reduces for the central chords due to being closer to the panel supports. In addition to the effect of vibration, the reason of the odd behaviors that are seen for outer sections of the third column, can be related to the rotational direction of the turntable which leads more exposure of direct wind on the third column rather than the columns that are away from the wind source. Similar behaviors can also be experienced in GCR 4, measured data is presented in figure 4.35.

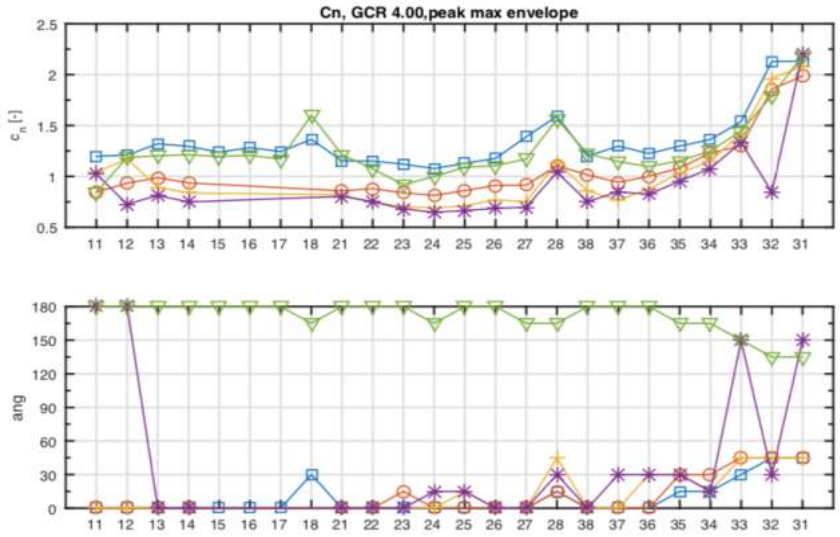

Figure 4.35 Local maximum peak normal force coefficients, GCR 4

4.3.3 Effect of Row Spacing

There are two different GCR values used during the test to investigate the effect of row spacing. GCR is the ratio of ground area occupied by the tracker array to the total area of PV panels. During the design stage of a solar energy field, GCR value set according to prevent shading which reduces energy production of the field. Therefore, these two GCR arrangements were proposed by the client which are representing 12 m and 16 m row spacings in the actual PV tracker field. Main aerodynamical effect of row spacing is related to blockage applied by upwind rows to the downwind ones. A similar study to investigate the effect of row spacing was held by CPP [16] and result showed that increasing row spacing slightly amplifies the loading on the downwind rows due to reduction in sheltering effect. In addition to that, there is another report [17] which uses CFD simulation to see aerodynamic behavior of PV panels, it states that minimum load coefficient for the downstream body happens when effective dimension of the body approximately equals to the gap between two bodies, which is not the case in our experiment even if for the GCR 2.65 arrangement. Therefore, expected increase in load coefficient for inner rows is not as clear as the reference tests. However, if we compare the peak coefficient tables for GCR 2.65 and GCR 4, we will see an increase around 0.2-0.4 in normal force coefficients measured from A1 of the inner rows, when we change the row arrangement to GCR 4. This increase is relevant to the results presented in both references. It can also be seen that this increase is highest at 60° pitch angle which induces the maximum blockage to the inner rows. To maximize and ease visual inspection of the results, [17] tests the models at 90° pitch, the difference between load coefficients measured from two different row spacing arrangements reaches as high as 0.6. When the pitch is reduced to 60° difference downs to 0.3 and the difference is almost 0 at 30° pitch angle. These results coincide with our data if we compare the peak load tables for two ground arrangements. It should be also noted that the smaller load coefficient values measured form A2 make hard to do the same comparison, but it can be still seen that absolute maximum values measured at 60° for GCR 4 are higher than the ones for GCR 2.65. If we extend our discussion to torque coefficient tables, we can say that row spacing does not have as much as effect on peak C_m values because it reaches to the maximum at mid-values of the pitch angle where sheltering effect is very little.

This is the end of chapter 4, all test results and related discussions were carried out. All of the referred documents in this section can be found in references. Major key points presented in this section will be summarized alongside with the future work and limitations of this study in conclusion chapter.

Chapter 5. Conclusion

The scope of this study was providing better understanding for aerodynamic forcing on 5 x 3 PVT array. The load coefficient data presented in the thesis are necessary for the client to secure its investment from any structural damage. This kind of a damage cuts down the production of the field and leads to a sizeable amount of reparation cost. Therefore, provided measurements and the discussions should be carefully investigated during the design stage of the field. In conclusion chapter, the thesis will be finalized with summarizing the test procedure, listing some of the major outcomes of the experiment and discussing the possible future studies alongside with the limitations of this work.

In order to measure pressure data, 1/15 plywood models were constructed according to information provided by the client. To experience relevant aerodynamic behavior, boundary layer and turbulence conditions of the real PVT field were carefully simulated in the tunnel. With using appropriate instrumentation, models were tested for different exposure angles, pitch angles and ground cover ratios. After recording pressure data that are measured from 522 pressure taps, normal force and torque coefficients were calculated for each section which were integrated to create the data presented in load zones. Data presented were normalized according to gust wind kinetic pressure. The results were presented with peak load graphs and tables to ease comparison of different load zones in different row locations. The summary of the major outcomes from these graphs and tables are listed below;

- The highest value of the normal force coefficients is reached at the highest pitch angle tested.
- The highest value of the torque coefficients is reached at the mid-values of the pitch angles tested.
- The load values experienced by the first and the last rows are higher than the values recorded from the inner rows of the PVT array.
- The load values experienced by the outer sections of each row are higher than the values recorded from the central sections due to the vortices created by the cornering winds.
- In every row and load zone, the highest value of the peak torque coefficient is in positive direction.
- The highest aerodynamic loading values are typically measured at 0° and 180°, which are direct wind exposure angles.
- Typically loading values are higher when the direction of the force coefficient matches with the direction of wind exposure.

- Increasing the pitch angle increases the blockage on the inner rows of the array. This effect reduces for GCR 4 arrangement due to higher spacing between rows that allows to more direct wind penetration on to the inner rows. The difference between the normal force coefficient values for inner rows of GCR 2.65 and GCR 4 is higher at the outer sections.
- Row spacing does not have a clear effect on torque coefficient values because highest values of C_m are reached at intermediate pitch angles that have almost insignificant blockage.

The results of this study found under consideration of Eurocode category I terrain profile. Different terrain profiles and surrounding structures yields to the different result, so before referring these result, ground profile of the solar field and the surroundings should be investigated. Also, array arrangement on the test section should be considered because this study only covers simple 5 x 3 rectangular arrangement of PVT array. Found critical locations may be different for other type of solar field configurations. Model dimensions should also be taken into account, because constructed models are reproduction of aerodynamically relevant geometries of a specific PVT system provided by the client and different systems may have different shapes that should be reproduced.

In this study the effect of three different parameters tested for different row and column locations in the array. However, effect of panel height can be investigated in future studies. Also test result may be extended for different type of terrain profiles with different turbulent and boundary layer conditions. For different meteorological conditions, this test can also be carried out for changing wind speeds. To support the test results, CFD simulation can be created to test the same array arrangement. In addition to that, FEM analysis of the models can be prepared to visualize mechanical stress and deflection on the support mechanism. Another possible extension to this study can be addition of oil or smoke flow over smaller models to visualize flow pattern on the tracker systems. This method can be helpful to locate boundary layer separation or any irregular flow pattern.

To conclude, this study was prepared by combining the result of two wind tunnel tests which were supervised by Prof. Marco Belloli, operated by Ing. Alessandro Fontanella and Ing. Stefano Giappino. All of the findings of these tests were presented, and all necessary comments were made with considering the theoretical background of the problem. Photos taken during the test were presented in Appendix section to provide better visual description to reader.

References

[1] *https://yearbook.enerdata.net/electricity/electricity-domestic-consumption-data.html*, Enerdata (2018)

[2] *Power Generation Costs in 2017*, International Renewable Energy Agency (2018)

[3] Lafond, F. , Bailey, A.G. , Bakker, J.D. , Rebois, D. , Zadourian, R. , McSharry, P. & Farmer, J.D. , *How well do experience curves predict technological progress? ,* Navigant Research (2017)

[4] *https://www.allearthrenewables.com/blog/dealers/pv-tracker-vs-pv-fixed-mount-system*, AllEarth Renewables (2012)

[5] Garratt, J.R. *Review: The Atmospheric Boundary layer,* Earth Science Reviews 37, p.89-134, (1994)

[6] Dyrbye, C. & Hansen, S.O. , *Wind loads on structures*, J. Wiley (1999)

[7] Stull, R.B. , *An introduction to boundary layer meteorology*, Kluwer Academic Publ. (1997)

[8] Munson, B.R. , Young, D.F. & Okiishi, T.H. , *Fundamentals of fluid mechanics*, J. Wiley, rev. 5, p. 485 (2006)

[9] Munson, B.R. , Young, D.F. & Okiishi, T.H. , *Fundamentals of fluid mechanics*, J. Wiley, rev. 5, p. 519 (2006)

[10] Munson, B.R. , Young, D.F. & T.H. Okiishi, T.H. , *Fundamentals of fluid mechanics*, J. Wiley, rev. 5, p. 513 (2016).

[11] Blevins, R.D. , *Flow Induced Vibrations*, Van Nostrand Reinhold Co. (1990).

[12] Gerhart, P.M. , Gerhart, A.L. & Hochstein, J.I. , *Munson, Young and Okiishi's Fundamentals of fluid mechanics*, J. Wiley, rev. 8 (2016).

[13] Longhi, S.F. , Montecino, D.G. & Garcia, E.T. , *Wind tunnel tests in a model of flat-shaped solar collectors plant,* (2016)

[14] *https://www.windtunnel.polimi.it/facility/*, Politecnico di Milano (2019)

[15] Belloli, M. , Rocchi, D. , Giappino, S. , Muggiasca, S. , Rosa, L. & Ronchi, L. , *GVPM Wind tunnel test procedures,* rev. 3, Politecnico di Milano (2017)

[16] Guha, T.K. , Fewless, Y. & Banks, D. , *Effect of panel tilt, row spacing, ground clearance and post-offset distance on the vortex induced dynamic loads on fixed tilt ground mount photovoltaic arrays,* CPP, ICWE 14 (2015)

[17] Shademan, M. & Hangan, H. , *Wind loading on solar panels at different inclination angles,* ACWE 11 (2009)

[18] Banks, D. , *Measuring peak wind loads on solar power assemblies*, CPP Wind Engineering (2011)

[19] Xypnitou, E. , *Wind loads on solar panel systems attached to building roofs*, Concordia University (2012)

[20] *Lecture notes in Wind Engineering*, Politecnico di Milano (2012)

[21] Geurts, C.P.W. , *Wind-induced pressure fluctuations on building facades*, Eindhoven University of Technology (1997)

[22] Banks, D. & Waye, S. , *Wind tunnel tests and wind load analysis for solaria ground mounted tracker*, CPP Wind Engineering (2012)

[23] Mohapatra, S. , *Wind tunnel investigation of wind load on a ground mounted photovoltaic tracker*, Colorado State University (2011)

[24] Cain, J.H. & Banks, D. , *Wind loads on utility scale solar PV power plants*, SEAOC (2015)

Appendix

7.1 Appendix A- Standards

ASCE 7-10 Section 27.4.3 Open building with Monoslope, Pitched or Troughed Free roofs;

27.4.3 Open Buildings with Monoslope, Pitched, or Troughed Free Roofs

The net design pressure for the MWFRS of open buildings with monoslope, pitched, or troughed roofs shall be determined by the following equation:

$$p = q_h G C_N \quad (27.4\text{-}3)$$

where

q_h = velocity pressure evaluated at mean roof height h using the exposure as defined in Section 26.7.3 that results in the highest wind loads for any wind direction at the site

G = gust-effect factor from Section 26.9

C_N = net pressure coefficient determined from Figs. 27.4-4 through 27.4-7

Net pressure coefficients, C_N, include contributions from top and bottom surfaces. All load cases shown for each roof angle shall be investigated. Plus and minus signs signify pressure acting toward and away from the top surface of the roof, respectively.

For free roofs with an angle of plane of roof from horizontal θ less than or equal to 5° and containing fascia panels, the fascia panel shall be considered an inverted parapet. The contribution of loads on the fascia to the MWFRS loads shall be determined using Section 27.4.5 with q_p equal to q_h.

Main Wind Force Resisting System – Part 1		0.25 ≤ h/L ≤ 1.0
Figure 27.4-4	Net Pressure Coefficient, C_N	**Monoslope Free Roofs** θ ≤ 45°, γ = 0°, 180°
Open Buildings		

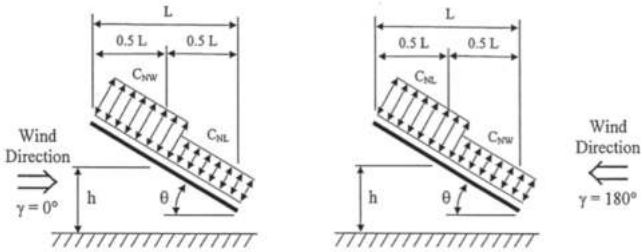

Roof Angle θ	Load Case	Wind Direction, γ = 0°				Wind Direction, γ = 180°			
		Clear Wind Flow		Obstructed Wind Flow		Clear Wind Flow		Obstructed Wind Flow	
		C_{NW}	C_{NL}	C_{NW}	C_{NL}	C_{NW}	C_{NL}	C_{NW}	C_{NL}
0°	A	1.2	0.3	-0.5	-1.2	1.2	0.3	-0.5	-1.2
	B	-1.1	-0.1	-1.1	-0.6	-1.1	-0.1	-1.1	-0.6
7.5°	A	-0.6	-1	-1	-1.5	0.9	1.5	-0.2	-1.2
	B	-1.4	0	-1.7	-0.8	1.6	0.3	0.8	-0.3
15°	A	-0.9	-1.3	-1.1	-1.5	1.3	1.6	0.4	-1.1
	B	-1.9	0	-2.1	-0.6	1.8	0.6	1.2	-0.3
22.5°	A	-1.5	-1.6	-1.5	-1.7	1.7	1.8	0.5	-1
	B	-2.4	-0.3	-2.3	-0.9	2.2	0.7	1.3	0
30°	A	-1.8	-1.8	-1.5	-1.8	2.1	2.1	0.6	-1
	B	-2.5	-0.5	-2.3	-1.1	2.6	1	1.6	0.1
37.5°	A	-1.8	-1.8	-1.5	-1.8	2.1	2.2	0.7	-0.9
	B	-2.4	-0.6	-2.2	-1.1	2.7	1.1	1.9	0.3
45°	A	-1.6	-1.8	-1.3	-1.8	2.2	2.5	0.8	-0.9
	B	-2.3	-0.7	-1.9	-1.2	2.6	1.4	2.1	0.4

Notes:
1. C_{NW} and C_{NL} denote net pressures (contributions from top and bottom surfaces) for windward and leeward half of roof surfaces, respectively.
2. Clear wind flow denotes relatively unobstructed wind flow with blockage less than or equal to 50%. Obstructed wind flow denotes objects below roof inhibiting wind flow (>50% blockage).
3. For values of θ between 7.5° and 45°, linear interpolation is permitted. For values of θ less than 7.5°, use load coefficients for 0°.
4. Plus and minus signs signify pressures acting towards and away from the top roof surface, respectively.
5. All load cases shown for each roof angle shall be investigated.
6. Notation:
   L : horizontal dimension of roof, measured in the along wind direction, ft. (m)
   h : mean roof height, ft. (m)
   γ : direction of wind, degrees
   θ : angle of plane of roof from horizontal, degrees

Eurocode UNI EN 1991-1-4 Section 7.3 Canopy Roofs;

(1) A canopy roof is defined as the roof of a structure that does not have permanent walls, such as petrol stations, dutch barns, etc.

(2) The degree of blockage under a canopy roof is shown in Figure 7.15. It depends on the blockage φ, which is the ratio of the area of feasible, actual obstructions under the canopy divided by the cross sectional area under the canopy, both areas being normal to the wind direction.

NOTE: $\varphi = 0$ represents an empty canopy, and $\varphi = 1$ represents the canopy fully blocked with contents to the down wind eaves only (this is not a closed building).

(3) The overall force coefficients, c_f, and net pressure coefficients $c_{p,net}$, given in Tables 7.6 to 7.8 for $\varphi = 0$ and $\varphi = 1$ take account of the combined effect of wind acting on both the upper and lower surfaces of the canopies for all wind directions. Intermediate values may be found by linear interpolation.

(4) Downwind of the position of maximum blockage, $c_{p,net}$ values for $\varphi = 0$ should be used.

(5) The overall force coefficient represents the resulting force. The net pressure coefficient represents the maximum local pressure for all wind directions. It should be used in the design of roofing elements and fixings.

(6) Each canopy must be able to support the load cases as defined below:

- for a monopitch canopy (Table 7.6) the center of pressure should be taken at $d/4$ from the windward edge (d = alongwind dimension, Figure 7.16)
- for a duopitch canopy (Table 7.7) the center of pressure should be taken at the center of each slope (Figure 7.17). In addition, a duopitch canopy should be able to support one pitch with the maximum or minimum load, the other pitch being unloaded.
- for a multibay duopitch canopy each load on a bay may be calculated by applying the reduction factors ψ_{mc} given in Table 7.8 to the $c_{p,net}$ values given in Table 7.7.

For canopies with double skins, the impermeable skin and its fixings should be calculated with $c_{p,net}$ and the permeable skin and its fixings with 1/3 $c_{p,net}$.

(7) Friction forces should be considered (see 7.5).

(8) The reference height z_e should be taken as h as shown in Figures 7.16 and 7.17.

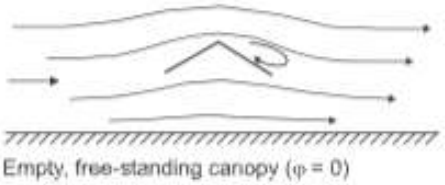

Empty, free-standing canopy ($\varphi = 0$)

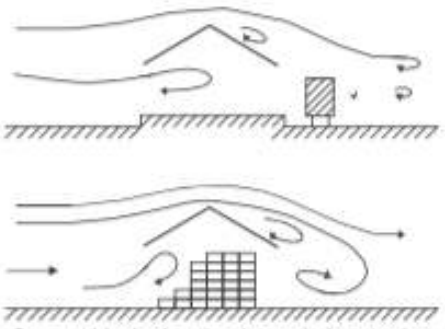

Canopy blocked to the downwind eaves by stored goods ($\varphi = 1$)

Table 7.6 — $c_{p,net}$ and c_f values for monopitch canopies

			Net Pressure coefficients $c_{p,net}$ Key plan 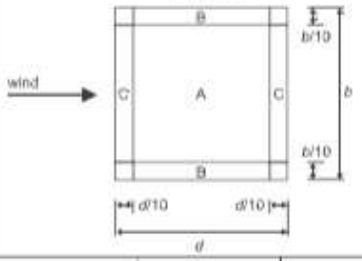		
Roof angle α	**Blockage φ**	**Overall Force Coefficients c_f**	**Zone A**	**Zone B**	**Zone C**
0°	Maximum all φ	+ 0,2	+ 0,5	+ 1,8	+ 1,1
	Minimum $\varphi = 0$	- 0,5	- 0,6	- 1,3	- 1,4
	Minimum $\varphi = 1$	- 1,3	- 1,5	- 1,8	- 2,2
5°	Maximum all φ	+ 0,4	+ 0,8	+ 2,1	+ 1,3
	Minimum $\varphi = 0$	- 0,7	- 1,1	- 1,7	- 1,8
	Minimum $\varphi = 1$	- 1,4	- 1,6	- 2,2	- 2,5
10°	Maximum all φ	+ 0,5	+ 1,2	+ 2,4	+ 1,6
	Minimum $\varphi = 0$	- 0,9	- 1,5	- 2,0	- 2,1
	Minimum $\varphi = 1$	- 1,4	- 2,1	- 2,6	- 2,7
15°	Maximum all φ	+ 0,7	+ 1,4	+ 2,7	+ 1,8
	Minimum $\varphi = 0$	- 1,1	- 1,8	- 2,4	- 2,5
	Minimum $\varphi = 1$	- 1,4	- 1,6	- 2,9	- 3,0
20°	Maximum all φ	+ 0,8	+ 1,7	+ 2,9	+ 2,1
	Minimum $\varphi = 0$	- 1,3	- 2,2	- 2,8	- 2,9
	Minimum $\varphi = 1$	- 1,4	- 1,6	- 2,9	- 3,0
25°	Maximum all φ	+ 1,0	+ 2,0	+ 3,1	+ 2,3
	Minimum $\varphi = 0$	- 1,6	- 2,6	- 3,2	- 3,2
	Minimum $\varphi = 1$	- 1,4	- 1,5	- 2,5	- 2,8
30°	Maximum all φ	+ 1,2	+ 2,2	+ 3,2	+ 2,4
	Minimum $\varphi = 0$	- 1,8	- 3,0	- 3,8	- 3,6
	Minimum $\varphi = 1$	- 1,4	- 1,5	- 2,2	- 2,7
NOTE	+ values indicate a net downward acting wind action - values represent a net upward acting wind action				

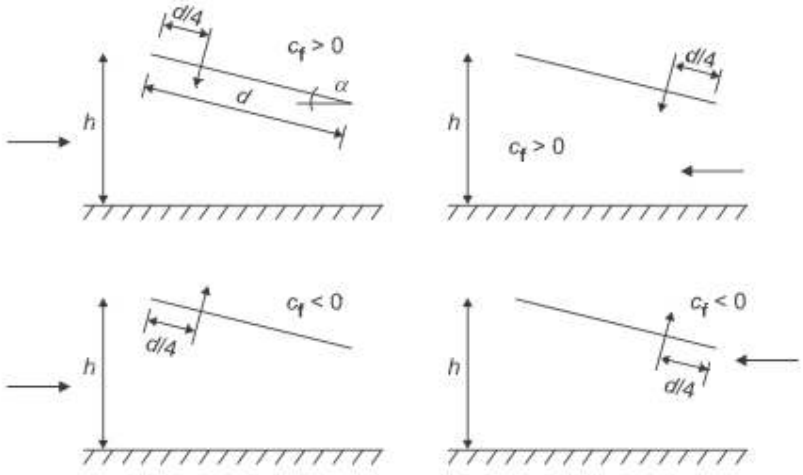

7.2 Appendix B- Technical Drawings of Test Models

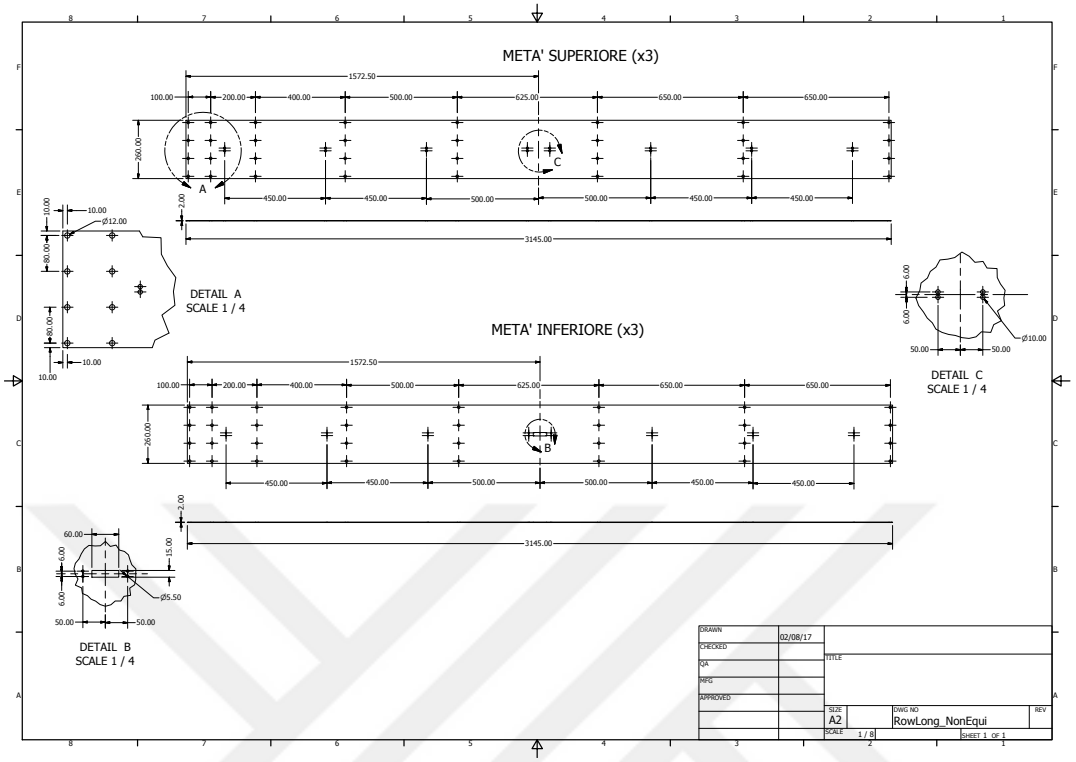

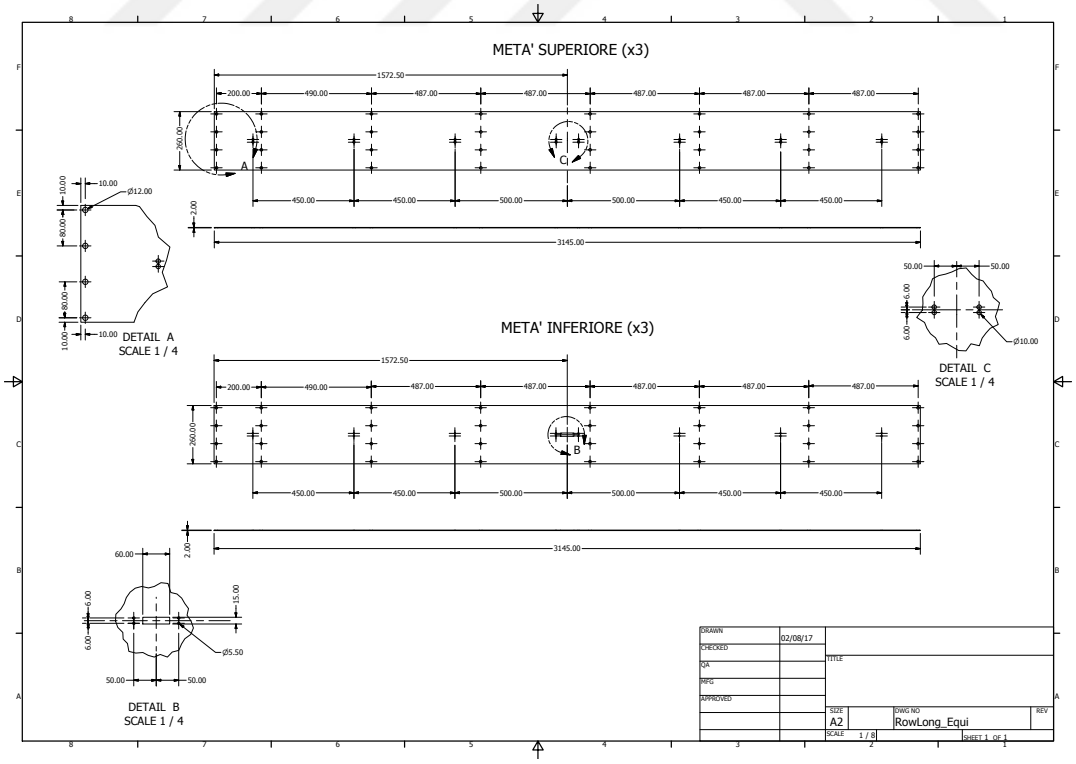

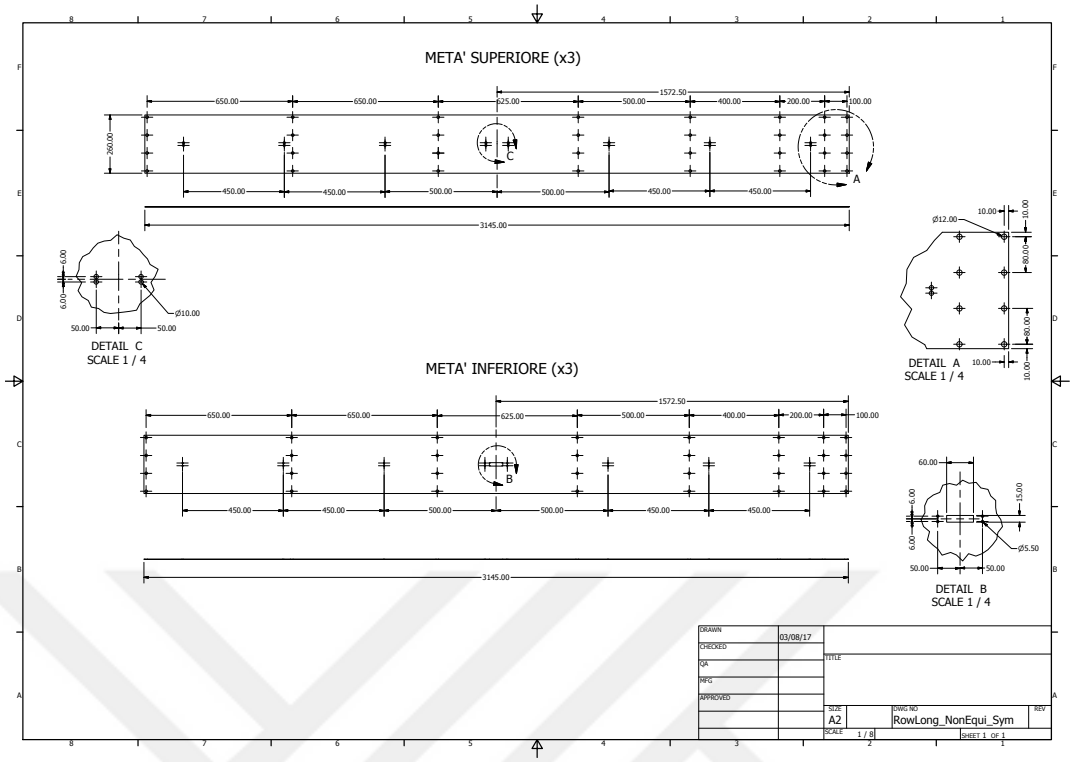
META' SUPERIORE (x3)
650.00
650.00
625.00
500.00
1572.50
400.00
200.00
100.00
260.00
450.00
450.00
500.00
500.00
450.00
450.00
3145.00
C
A
6.00
6.00
Ø10.00
50.00
50.00
DETAIL C
SCALE 1 / 4
Ø12.00
10.00
10.00
80.00
80.00
10.00
10.00
DETAIL A
SCALE 1 / 4
META' INFERIORE (x3)
650.00
650.00
625.00
500.00
1572.50
400.00
200.00
100.00
450.00
450.00
500.00
500.00
450.00
450.00
3145.00
B
60.00
6.00
6.00
15.00
Ø5.50
50.00
50.00
DETAIL B
SCALE 1 / 4
DRAWN
03/08/17
CHECKED
QA
MFG
APPROVED
TITLE
SIZE
A2
DWG NO
RowLong_NonEqui_Sym
REV
SCALE
1 / 8
SHEET 1 OF 1

7.3 Appendix C- Test Photos

Instrumentation & Test Models;

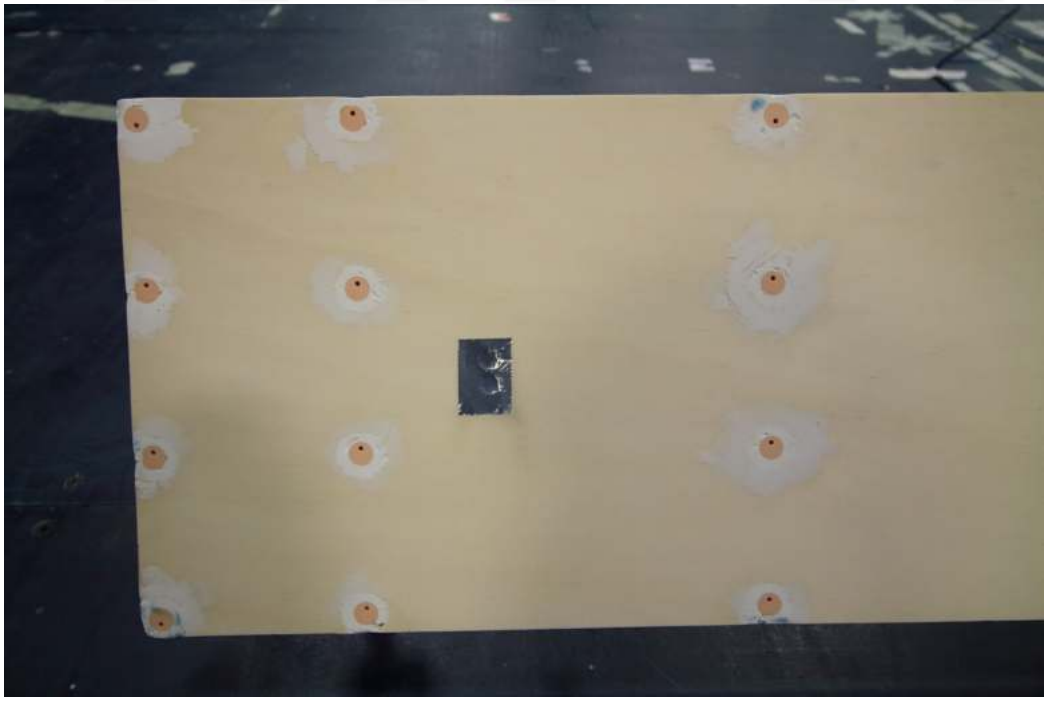

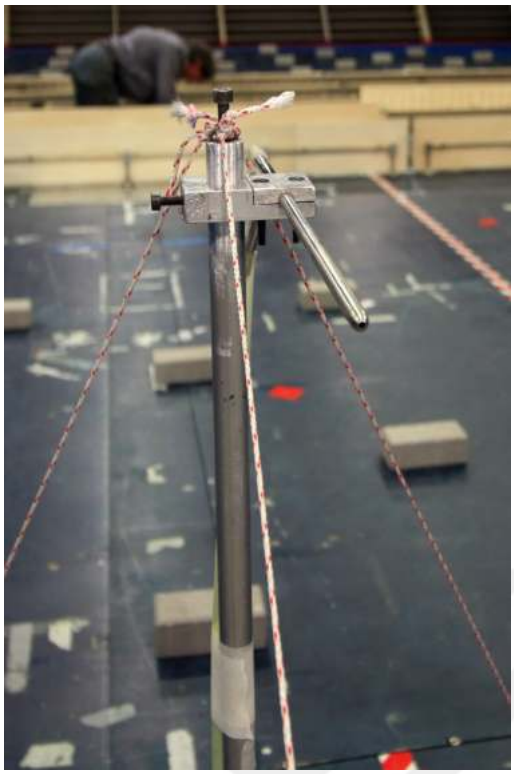


POLITECNICO


POLITE

Isolated First Row Test;

Full Array Tests;

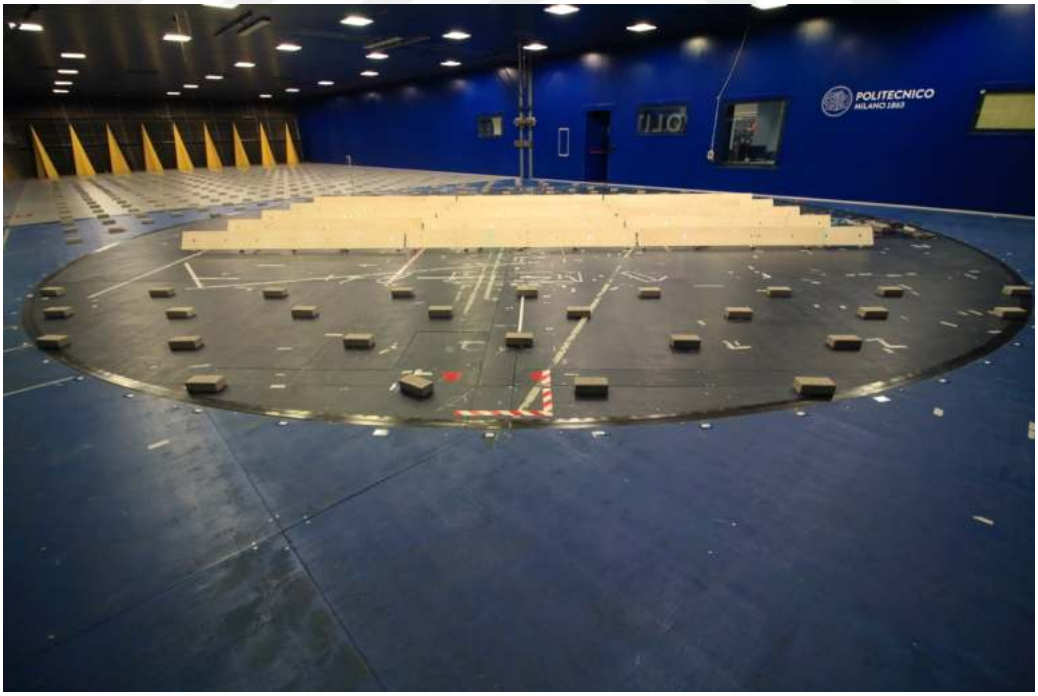
POLITECNICO
MILANO 1863